UNIVERSITY OF OSLO
Department of Physics

Thesis for the degree
Master of Science:

Fault dynamics of pseudotachylytes in the Lindås nappe, Bergen Arcs

Hedda Svarverud Aasen

June 14, 2013

Acknowledgements

Two years as a master student at PGP is soon over, the thesis is written, and now there are some people I would like to thank.

First of all, my supervisors, prof. Torgeir B. Andersen and prof. Håkon Austrheim, for introducing me to the Bergen area and Holsnøy. Such a nice place!

Also, Torgeir, for always being available, and for constructive critisism of my drafts. Håkon, for always making time for the numerous questions, and for commenting my drafts.

Muriel Erambert for patiently guiding me through the work-flow at the microprobe.

Håkon and Audhild for their generosity, letting me stay at Austrheim during my fieldwork.

Kerstin, who got all the nice weather, and Geir, who got all the bad, for assistance and company in the field.

PhD students Kjetil Thøgersen and Jørgen Trømborg for teaching me so many useful things my first year at PGP.

To Biojentene for making my first experience with the University so nice. Actually, all my years here.

My fellow students at ZEB and PGP for lots of good times. Kristin and Kerstin, we made it!

My great flatmates; Mariann, for buying me the things I need when forgetting to do it myself, and Kristina, for always having chocolate available for emergencies.

Last, thanks to my family and friends back home for encouraging me and always believing in me!

Abstract

Intermediate deep earthquakes are released below the seismogenic zone in subduction and collision, like under Himalaya, where they occur all the way down to the crust-mantle boundary. At great depths faulting by brittle failure is normally inhibited by the high confining pressure, and deformation by ductile flow is expected. Several solutions have been proposed to explain earthquakes below the brittle-ductile transition, but a definite explanation is yet to be found. At Holsnøy, Bergen Arcs, pseudotachylytes, interpreted to represent melt formed during seismic slip, are observed in close spatial relationship with high grade rocks including Proterozoic granulites, and Caledonian eclogites and amphibolites facies rock. The eclogites formed at pressures corresponding to depth of 60-70 km, and the pseudotachylytes may represent intermediate depth paleo-earthquakes formed in the root zone of the Caledonian orogen.

This thesis focuses on the dynamics of pseudotachylyte generation during faulting. Detailed mapping and sampling of faults has been carried out at three outcrops to constrain the field relations and mineralogy. Microscopy has been used to study the microtextures of the pseudotachylytes and their wall-rock damage zones. The average dynamic shear stress during faulting τ_f has been estimated using the energy budget of faulting. The equation used was $\tau_f = \rho[(1-\phi)H + C_p(T_i - T_{hr})]t/d$, where density ρ, latent heat of fusion H, heat capacity C_p, and initial melt temperature T_i is found in the literature. Based on observations of thin sections the amount of clasts ϕ has been estimated. Micro probe analyses have been performed to find the mineral assemblage of pseudotachylytes, and this has been used to find the ambient host rock temperature T_{hr} from previous work. The displacement d was measured in the field, and the average thickness of melt t was determined from either thin sections or field measurements.

The wall-rock damage zones were found to consist mainly of angular to subrounded fragments, suggesting a cataclastic origin. Pseudotachylyte injection veins truncating the wall-rock damage zone have been observed, and this indicates that the wall-rock damage zone was present at the time of melt generation. Spherulites and presumably newly grown anhedral garnet crystals have been observed in psedotachylytes. Both amphibolite and eclogite facies pseudotachylytes were observed, suggesting that faulting occurred on a wider range of depths than previously described for the pseudotachylytes at Holsnøy. Estimated values of the dynamic shear stress during faulting range from 21,88 to 146,61 MPa. The estimated values were found not to correlate with depth since eclogite facies and amphibolite facies pst show the same variation. Both low and high shear stresses were obtained for faults with small displacements, while a low shear stress was obtained for the fault with the largest displacement.

f

Contents

This page intentionally left blank

Chapter 1

Introduction

1.1 Objective of Thesis

This thesis concentrate on the dynamics of pseudotachylyte generation during faulting. The primary objective is to use the energy budget of faulting, based on the amount of preserved melt generated during what is suggested to be paleo-earthquakes, to estimate the average dynamic shear stress during faulting. This value corresponds to the dynamic stress drop associated with rupture, and yield information on the shear stress resistance of the crust. In order to obtain representative values for the parameters used in the estimate detailed field work, microscopy, and micro probe analyses is necessary.

Microtextural observations of the pseudotachylyte and microstructural observations of the wall-rock damage zones will be described. The change in composition of the main constituting minerals from the adjacent wall-rocks and to the pst will also be presented.

1.2 Fault Dynamics, Earthquakes and Pseudotachylytes

1.2.1 Fault Dynamics

Twiss and Moores (2007) define **a fault** as '...a surface or narrow zone in the Earth's crust along which one side has moved relative to the other in a direction parallel to the surface or zone'. Faults have a self-similar nature, and are observed at all scales ranging from μm to km.

When considering the thermomechanical effects of faulting, if work against gravity is neglected, almost all mechanical work done during deformation must be converted into heat (Scholz, 1990). Following Scholz (1990), a general energy balance for faulting can be written:

$$W_f = Q + E_s + U_s, \tag{1.1}$$

where W_f is mechanical work done in faulting (including both friction and ductile deformation), Q is heat, U_s is surface energy (found to be negligible for faulting), and E_s is the energy radiated in earthquakes. We can use this to determine the energy of the faulting provided that the temperature change can be determined. This approach will be used in Chapter 6.

1.2.2 Earthquakes

As Rice (2006) states: *Earthquakes occur because fault strength weakens with increasing slip or slip rate.* Field observations from high-level fault show that the slip in individual earthquake events are localized to a zone commonly narrower than ≤1-5 mm in width. This suggests that the weakening mechanisms must be thermal, otherwise, vast amounts of the rock would have undergone melting, and this have not been reported. Rice (2006) suggests that two important thermal weakening mechanisms operate during faulting;

1. thermal pressurization of pore fluid in and adjacent to the fault core. This reduces the effective stress, σ_{eff}, which in turn reduces the shear strength τ for any given friction coefficient μ.
2. flash heating at highly stresses frictional micro contacts during fast slip. This reduces the friction coefficient.

In addition, macroscopic melting is also suggested, and probably most significant in earthquakes with sufficiently large combinations of slip and initial effective normal stresses. Hot melt have low viscosity, which reduces the dynamic friction (Sibson, 1975). However, the onset of melting is also suggested to increase the effective fault strength due to an increase in the effective fault contact area and the high viscosity of silicate fluids near solidus. This may temporary increase in dynamic friction (viscous bracing) and may lead to rupture arrest (Fialko, 2004).

Present-Day Seismicity

Ground motions have been studied by seismologists for more than a decade, and the detailed knowledge increases as technology improves. Broadband seismographs record ground motions over a broad period range (from 0.02 s to hours), and have revealed a high diversity of slip characteristics and energy budgets of earthquakes. Also, a high variation in momentum, change of stress and duration of earthquakes are observed (Kanamori, 2008).

The spatial distribution of earthquakes is limited in the lateral direction by the fact that most seismic events are interplate earthquakes, occurring at plate boundaries, the most active beeing subduction and collision zones. Even though earthquakes *do* occur also as intraplate events, $\sim 95\%$ of the global seismic moment released are result of interplate earthquakes (Scholz, 1990).

The seismic moment is a measurement of earthquake size givens as,

$$M_{0ij} = \mu(\overline{\Delta u_i} n_j + \overline{\Delta u_j} n_j) A,$$

where $\overline{\Delta u_i}$ denotes the mean slip vector averaged over the fault area A, with unit normal n_j, and μ denotes the shear modulus (Scholz, 1990).

Earthquakes occure at depths ranging from the upper crust and down to about 680 km (Jung et al., 2004). Most earthquakes are initiated in the seismogenic zone, which thickness is defined as the limiting depth of seismic faulting as defined by the distribution of aftershocks and microseismicity (White, 2012). For simplicity, the lower boundary of the seismogenic zone is where the rheological transition from pressure-dependent to temperature-activated processes occurs, marking the change from brittle to elasto-plastic and/or viscous deformation of rocks (Scholz, 1990). The seismogenic zone typically comprise the upper 2-15 km of the continental crust (Sibson and Toy, 2006). These earthquakes are produced by brittle shear failure and/or frictional sliding on preexisting fault structures (Scholz, 1990).

Subduction zones are the most seismically active regimes on earth (Scholz, 1990). Subduction zones, and collision zones with a thickened crust, are also the places on earth where earthquakes extends to the greatest depths. When discussing earthquakes in such settings, the term shallow

earthquakes often include all earthquakes down to about 70 km depth. Between 70 and 300 km they are often considered intermediate deep, and everything beyond 300 km is deep (Green and Huston, 1995; Hacker et al., 2003). In subduction zones earthquakes are observed to occur to depths of approximately 680 km (Jung et al., 2004), in Benioff-Wadati zones related to the slab sinking into the mantle. The dip of these zones are on average about 45° (Kearey et al., 2009).

Subduction zone earthquakes often have down-dip widths of more than 200 km, and similar dimensions along-strike. This makes such earthquakes the largest occurring, both considering rupture area and moment (Scholz, 1990). Seismicity occur both in upper and lower plate, but the majority of moment is released on the interface between the downgoing and the overriding plate (Green and Huston, 1995; Kanamori, 2008). This interface is actually a deformation zone including parts of both the overriding and subducting plates, and not a narrow plane like for most high level faults (Kanamori, 2008).

Intermediate depth earthquakes in subduction zones tend to occur within the uppermost few km of the subducting slab. In many subduction zones, e.g. , Tohoku (Fig. 1.6), intermediate deep earthquakes are found to occur in two distinct layers; an upper and a lower seismic zone. These zones are separated vertically by an aseismic or weakly seismic zone, up to 40 km in thickness (Hacker et al., 2003)

Intermediate deep earthquakes are observed to occur by shear failure and exhibit double couple focal mechanisms. They have many fewer aftershocks than shallow earthquakes (here; shallower than 40 km), and slightly fewer aftershocks than deep (here; beyond 400 km) (Hacker et al., 2003). Despite these observed common properties of intermediate deep earthquakes, Kanamori (2008) addresses the heterogeneities of seismic slip characteristics of subduction zone earthquakes. The slip motion can be correlated with the location of the earthquake in the subduction zone. Earthquakes initiated within the subducting slab tend to have fast slip and may cause strong shaking. Earthquakes of the same magnitude occurring at the subduction boundary, the frictional interface between the downgoing and overriding plate, have slower slip and cause less shaking.

As a transition from shallow brittle failure to deeper creeping motions, Obara (in (Kanamori, 2008)) reports silent earthquakes in the downward extention of the seismogenic megathrust boundary at subduction zones, see Fig. 1.1. Such silent earthquakes have slip motions lasting from several minutes and up to 1 hour, and are associated with small tremors.

This thesis include faults with pst formed during earthquakes at shallow to intermediate depths, the deepest at ∼70 km.

Paleoseismicity

The best, and perhaps only certain, indication of paleoseismicity is the occurrence of pseudotachylytes (Sibson, 1975; White, 2012). Evidence for high-level paleoseismicity from identified fault-generated pst are quite common (Swanson, 1992). Pseudotachylyte is reported from exhumed fossil subduction zones from i.a. , the Alpine Corsica by Austrheim and Andersen (2004) and Andersen and Austrheim (2006), from Central Zambia by John and Schenk (2006), and from the Norwegian Caledonides by Austrheim and Boundy (1994) and Lund and Austrheim.

1.2.3 Pseudotachylyte

The term *pseudotachtylyte* was introduced by Shand (1916) to described a dark, aphanitic rock found as veins and networks in granite in Parijs, South Africa. This area is part of one of the worlds largest meteorite impact structures, the Vredefort Dome (Dietz, 1960). Goldschmidt (1943)

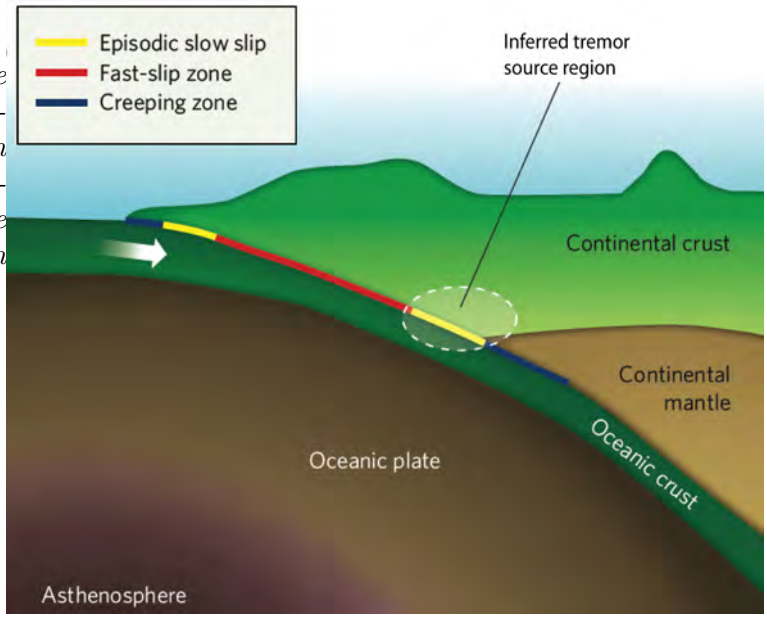

Figure 1.1: *Location of brittle fast-slip (seismogenic) and slow-slip zones along the subduction zone boundary (the interface between the subducting slab and the overriding plate in a subduction zone). From Kanamori (2008).*

described vesicular glass along faults in the Norwegian Caledonides, and interpreted it as product of frictional fusion. The name pseudotachylyte refers to a rock having a similar appearance as, but an origin distinct from, the glassy, basaltic rock *tachylyte*. An alternative way of spelling is *pseudotachylite*. The abbreviation *pst* will be used throughout the rest of this thesis.

What is required of a rock to be named *pseudotachylyte* has long been, and still is, some matter of debate. As the classification of fault rocks includes gradual transitions, pst can be hard to distinguish from (ultra)cataclasite, and even from ultramylonite, the latter a result of ductile deformation only (Sibson and Toy, 2006; Twiss and Moores, 2007). Several authors, e.g. , Philpotts (1964) and Lin (1996), argue that there is a gradation between melt-origin pst and pst-like cataclastic veins formed with no or little frictional melting, and include both in the term pst. Although, most authors find it a necessity that the pst shows evidence of having been through a melt phase. Glass may or may not still be present in the pst. Magloughlin and Spray (1992) argue that presence or absence of glass is not a test on whether the rock had a melt origin or not, because pst is usually formed under conditions not favouring preservation of glass (Shand, 1916), se also (Maddock, 1986). Magloughlin and Spray (1992) instead lists several features that, alone or in combination, are indicative of the rock having a melt origin, rather than a cataclastic origin;

- quenched vein margins
- a variation in microlite textures and size with respect to position in a vein
- vesicles or amygdules
- newley crystallized minerals stable only at high temperatures
- dendritic microlite habit
- sulfide droplets
- spherulites
- melting effects in clasts within pst
- certain recrystallization features
- certain systematic chemical relations between pst and host rock (pst slightly more mafic than host rock, and often has an andesitic to basaltic composition)

Flow structures are also often observed in pst, caused by flow during displacement of the wall rock along fault veins, and injection flow between walls of extension fractures into dilatational injection vein reservoirs (Swanson, 1992).

Pst is described from three main settings in the nature; impact structures (Dietz, 1960; Shand, 1916), the basal slip surface in some landslides (Masch et al., 1985), and exhumed faults (Andersen and Austrheim, 2006; Austrheim and Boundy, 1994). In addition, pst has been generated in laboratory experiments e.g. , (Lin and Shimamoto, 1998; Weiss and Wenk, 1983) and as a result of diamond drilling in rocks (Killick, 1990). This thesis will concentrate only on fault-related pst.

Fault-Related Pseudotachylyte

Fault-related pst is largely restricted to crystalline metamorphic or plutonic rocks (Sibson and Toy, 2006), but has also been reported from metasediments (Bjørnerud, 2010) and limestones (Vigano et al., 2011). A plausible reason for the major part of the pst found to occur in crystalline rocks, is that such rocks tend to have low porosity and high competence, and therefor have the ability to store large amounts of elastic strain energy prior to brittle failure (Sibson and Toy, 2006). Planar fabrics in the wall-rock imposes an anisotropy, and influence the direction of faulting. Where the wall-rock is foliated, $\sim 61\%$ of the fault-veins are parallel to the foliation, while $\sim 39\%$ cross-cut the foliation. As a consequence, there is in general a lack of offset markers for estimating of slip along the fault.

Pst has been reported from thrust and strike-slip systems, including transpressional and transtentional settings, in approximately equal numbers. Significantly fewer occurrences is reported on pst from normal fault systems (Sibson and Toy, 2006).

Estimates of likely depths of pst formation at different localities cover a large range of depths, as seen in Fig. 1.2. The formation depths range from upper continental crustal levels and down to the upper mantle lithosphere. Most of the pseudotachylytes observed are however generated in the upper continental crust seismogenic zone, from depths of 1-2 km and down to more than 20 km (Sibson and Toy, 2006), see Fig. 1.2. Note that the scale in the left- and right-hand groups differs, and the location of the Bergen Arcs to the right.

Fault Vein Geometry

Pst veins can be classified on basis of their geometry, like done by e.g. , Sibson (1975) and Swanson (1992). Sibson (1975) distinguish between *fault veins*, *i.e.*, pst found along the slip-surfaces which are mostly planar, and *injection veins*, which ramify of the slip surface in a highly irregular way, see Fig. 1.3a. The fault veins are commonly a few millimeters to a few centimeters thick, but may vary along the fault plane (Swanson, 1992). The fault veins commonly show lenticular distribution of pst on centimeter-scale (Sibson and Toy, 2006). Swanson (1992) describe fault veins as the typical *generation surface* of pseudotachylyte, and injection veins as common *reservoir-structures*. The host rock intruded by injection veins can be referred to as a reservoir zone.

Injection veins lead the melt away from the generation surface and into the cooler wall rocks, and often have a high angle to the fault veins (Swanson, 1992). The thickness of injection veins may reach several centimeters, and they can extend several meters into the wall rock. Injection veins are not a truly unique character for pst, it's intrusive appearance may also be mimicked by cataclasites and gouges(Sibson and Toy, 2006).

A different geometry also commonly observed with pst is paired slip surfaces, isolating host rock in-between. Swanson (1992) call this parallel fault structure *pst generation zones*, see Fig. 1.3b.

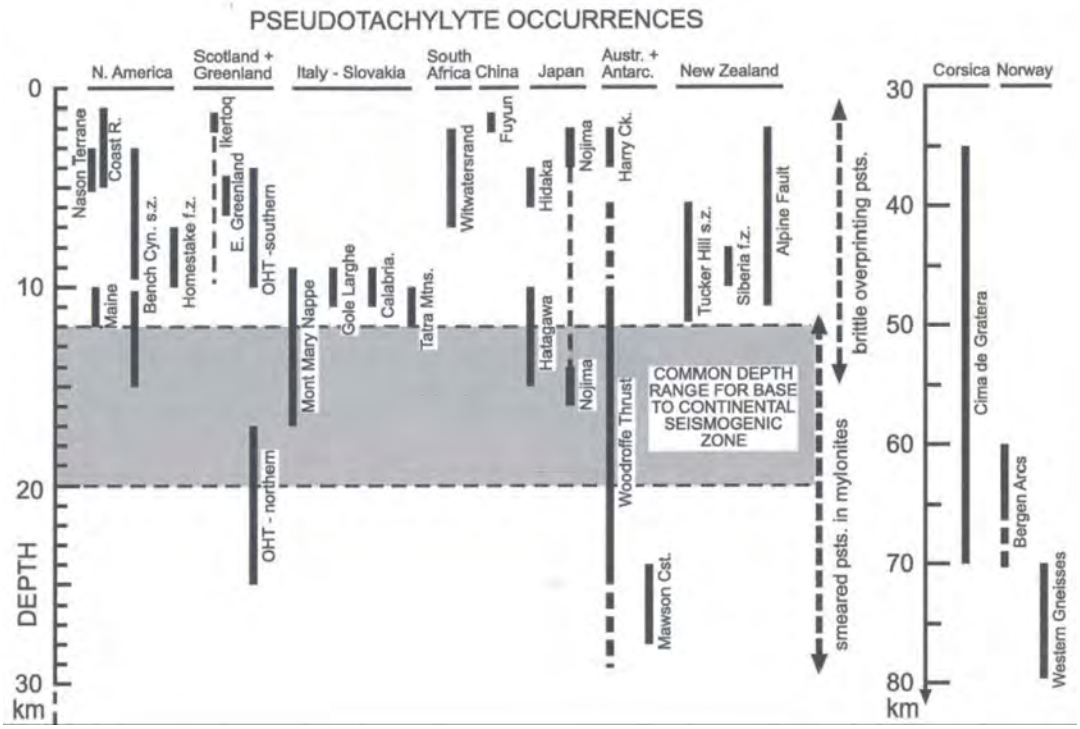

Figure 1.2: *Estimated depths of formation for fault-generated pst. Note the change in depth scales between left-and right-handed groups, and the location of the pst of the Bergen Arcs, Norway. From Sibson and Toy (2006).*

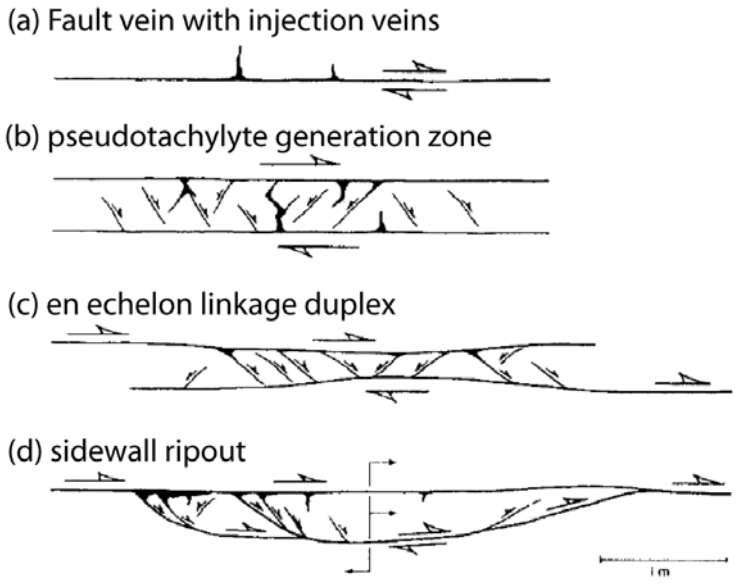

Figure 1.3: *Fault structures associated with pst generation: (a) Fault vein - injection vein system. (b) paired shear systems of pst generation zones. (c) en echelon linkage duplex in typical extentional geometry. (d) Sidewall ripouts with leading and trailing structural assemblages. After Swanson (1992).*

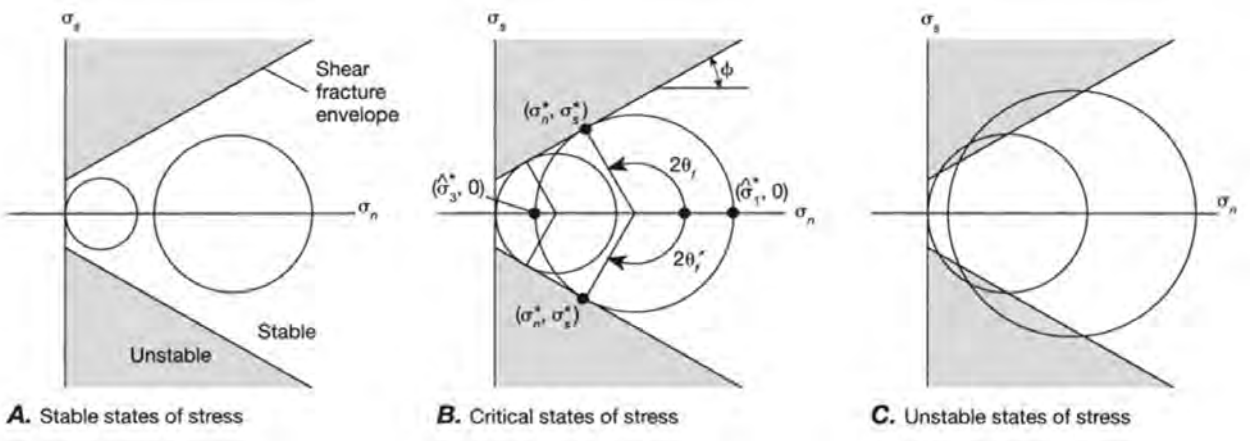

Figure 1.4: *Coulomb fracture criterion for axial compression. The fracture criterion divides the Mohr diagram into areas of unstable stress(shaded) and stable stress(unshaded). Mohr circle representing stable states of stress (A), critical states of stress (B) and unstable states of stress(C). Modified from Twiss and Moores (2007).*

Internal fracture assemblages in the pst-embedded host rock include orthogonal dilatant veins and conjugate shear fractures, both indicative of fault-parallel extention associated with the injection of pst (Swanson, 1992).

A somehow similar fault-geometry, described from strike-slip fault-settings, is *en echelon linkage duplexes*. Elongated areas of extensive overlapping, parallel slip surfaces develop at the ends of en echelon strike-slip fault segments. The internal deformation by conjugate faulting and fault-linkage results in pst-bearing, slab-shaped, duplexes, see Fig. 1.3c.

Sidewall ripouts are coupled extentional and contractional ramps that define tabular to curvi-planar fault lenses adjacent to the main slip surface(Swanson, 1992), see see Fig. 1.3d. These structures are interpreted to be mesoscale examples of adhesive wear generated as tabular ripouts during slip along the main fault.

When multiple fault vein arrays are observed, these are interpret as evidence for repeated rupturing with identical fault styles and deformation mechanisms of subsequent earthquake events (Swanson, 1992).

1.2.4 The Mohr-Coulomb Criterion for Shear Fracture

This section presents a summary of Mohr-Coulomb, and the textbook by Twiss and Moores (2007) is used as the main reference for text and figures. Fracture experiments on rocks in confined compression have shown that initiation of fractures depends on the differential stress,
$\sigma^{(Dif)} = \hat{\sigma}^1 - \hat{\sigma}^3$, and that with increased confining pressure, a higher magnitude of differential stress is necessary to cause shear fracture, see Fig. 1.4.

A shear fracture envelope, separating stable states of stress from unstable states of stress, can be constructed on the Mohr diagram. The shear fracture envelope, based on experimental data, approximates two lines symmetric across the σ_n axis, see Fig. 1.4. Any Mohr circle contained between the two lines represents a stable stress state, like in Fig. 1.4a. A Mohr circle tangent to the lines, like in Fig. 1.4b, have reached a critical state of stress causing shear failure. A Mohr circle that crosses the failure envelope, like in Fig. 1.4c, experience stresses that are to high for the material to support, and fracturing would already have occurred.

The straight line approximation of the slightly concave failure envelope is the Coulomb fracture criterion. It states that the critical shear stress $|\sigma_s^*|$ equals a constant c plus the tangent of the slope angle ϕ of the line times the normal stress σ_n, or

$$|\sigma_s^*| = c + \mu\sigma_n, \tag{1.2}$$

where

$$\mu = tan\ \phi, \tag{1.3}$$

and where μ is the slope of the lines and ϕ is the slope angle of the line (see Fig 1.4b), taken to be positive.

The constants in Eq. (1.2), c and μ characterize the failure properties of the material, and varies from one type of rock to another. c is the cohesion; the resistance to shear fracture on a plane across which the normal stress is zero. μ is referred to as the coefficient of internal friction, and ϕ the angle of internal friction because of the similarity, when c is zero, between Eq. (1.2) and Amontos' 2nd. law of friction,

$$|\sigma_s^*| = \overline{\mu}\sigma_n, \tag{1.4}$$

where $\overline{\mu}$ is the coefficient of sliding friction. Amontos' 2nd. law of friction states that the friction is proportional to the normal load across the sliding surface.

1.2.5 Seismicity at High Confining Pressure

In addition to the general question of the weakening mechanisms of faults, an other problems arise regarding seismicity at high confining pressure. At great depths faulting by brittle failure is normally inhibited by the high confining pressure and the following extreme values of the differential stresses, $\sigma^{(Dif)}$, needed to overcome the sliding friction, see Fig. 1.4.

Several solutions, some of the ideas overlapping, have been proposed to explain earthquakes below the brittle-ductile transition, including the following;

1. Transformational faulting. This hypothesis is based on rocks being subducted to depth outside the field of stability of the mineral assemblage; their phase boundaries are overstepped. Large volumes of such metastable rock will suddenly undergo prograde metamorphic reactions, phase transformations, accompanied by densification, if the PT-path of the subducting lithosphere reaches the kinetic boundary at pressures below a critical value. This instant densification can cause earthquakes to be initiated, if phase transformations propagates along fault-like features (Hacker et al., 2003; Kirby et al., 1991).

2. Densification-induced anticrack failure. This mechanism is based on experiments on metastable olivine that during the phase transition from olivine to spinel show Crack-shaped lenses of the denser spinel oriented perpendicular to the compression direction. This is opposite of tensile cracks, and they were referred to as anticracks. A positive feedback between reaction rate and temperature leads to anticracks linking up, and at a critical density of anticracks the material fails (Green et al., 1990; Tingle et al., 1993).

3. Dehydration embrittlement. When hydrated rocks undergo dehydration reactions and a free fluid phase is released, the result is an increased pore fluid pressure. This has the effect that it lowers the effective stress on the fault plane, thus allows shear fracturing to happen, and a sudden stress drop occurs (Hacker et al., 2003).

4. Ductile shear heating causing thermal runaway. Localized shear instabilities generates heat faster than dissipation by conduction. This initiates melting along the shear plane and enables slip at relatively low shear stresses. (Braeck and Podladchikov, 2007; Braeck et al., 2009)

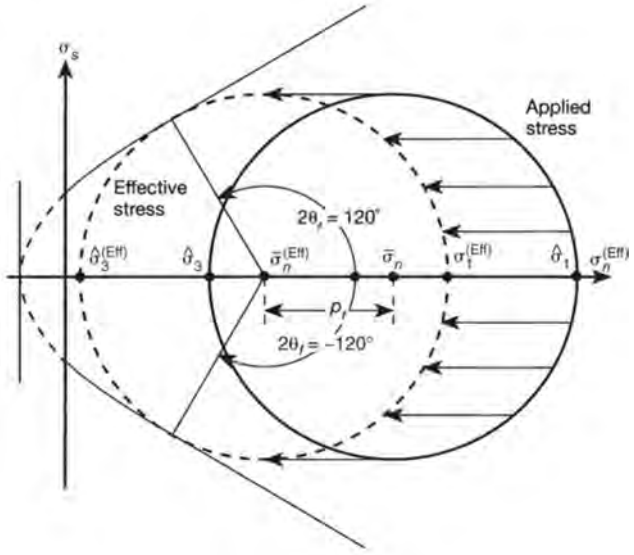

Figure 1.5: *Mohr diagram with the effective stress plotted on the horizontal axis, showing the effect of pore fluid pressure on the fracture stability of rock. At (relatively) large differential stresses, an increase in pore pressure leads to shear fracture by lowering the effective stress, shifting the Mohr circle to the left in the diagram. From Twiss and Moores (2007).*

Dehydration embrittlement and shear heating by viscous dissipation will be further explained in the following Paragraphs.

Dehydration Embrittlement

One alternative way to bring the Mohr circle in contact with the failure envelope, is to increase the pore fluid pressure in the rock. The presence of pore fluid makes rocks behave as the confining pressure were lower by an amount equal to the pore fluid pressure. When reducing the applied normal stress components by an amount equal to the pore fluid pressure p_f, the result is the effective stress $\sigma_n^{(Eff)}$. The applied shear stress is unchanged, hence the Mohr circle does not change in diameter, but is shifted to the left along the σ_n axis, see Fig. 1.5. The Coulomb fracture criterion is then:

$$|\sigma_s^*| = c + \mu(\sigma_n^{(Eff)}) = c + \mu(\sigma_n - p_f), \tag{1.5}$$

where

$$\sigma_n^{(Eff)} \equiv \sigma_n - p_f. \tag{1.6}$$

The pore pressure also affects the frictional sliding. An elevated pore fluid pressure decreases the effective normal stress across the sliding surface. As Eq. (1.4) show, the frictional stress is proportional to the effective normal stress across the sliding surface, and the critical shear stress necessary for sliding also decreases (Twiss and Moores, 2007).

At mid-ocean ridges oceanic crust undergo hydrothermal alteration involving hydration of pyroxene and olivine to serpentine. This alteration is enhanced by the temperature gradient and the fracturing at the mid-oceanic ridges. The water is released in subduction zones during dehydrating reaction (Bach and Früh-Green, 2010).

In many subducting slabs a double seismic zones is observed. Based on the observed spatial correlation between seismicity and hydration state in crust and mantle, Hacker et al. (2003) suggests that the upper seismic zone represents dehydration of the upper crust, with some contribution from the lower crust, and that the lower seismic zone represents dehydration of the upper mantle.

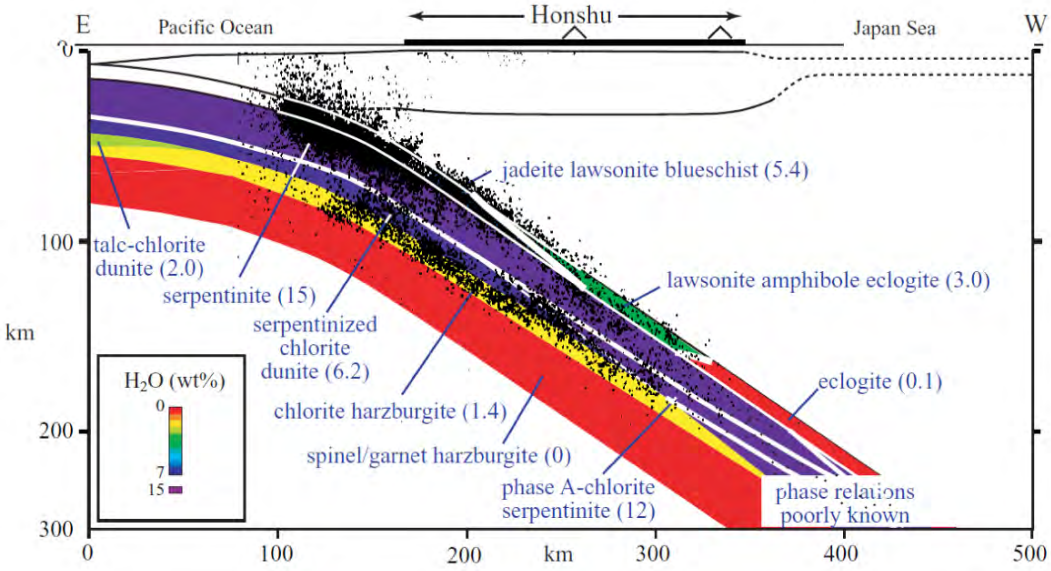

Figure 1.6: *Correlation between seismicity and phase transitions in the Tohoku subduction zone, with the location of Honshu on the top of figure. Phase transitions at $P > 5$ GPa and $T > 600^{\circ}C$ is poorly known. Colors represent the hydration state of the rocks. Modified from Hacker et al. (2003).*

Shear Heating

In dry rocks, where the pore fluid pressure is zero or too low to be significant, the shear heating mechanism may be an alternative way of generating catastrophic failure of rocks (Braeck and Podladchikov, 2007; Braeck et al., 2009).

Even below the conventional elastic limit, most materials respond by creep under constant load and stress relaxation under constant extention induced by defects and imperfections; they behave non-elastic. Most material, including rocks, may therefor be characterized as viscoelastic; the rheology contain both a viscous and a elastic component. The viscosity is strongly dependent on temperature (Braeck and Podladchikov, 2007).

The temperature increase over time arising from shear heating is given by the equation,

$$\frac{dT}{dt} = \frac{\tau\dot{\varepsilon}}{\rho C_p},$$

where T is temperature, t is time, τ is shear stress, $\dot{\varepsilon}$ is strain rate, ρ is density and C_p is heat capacity (Stuwe, 2007). This equation also show that the shear heating is strain-rate dependent, and strain rate is temperature-dependent. An increased strain rate in a weaker zone cause a temperature rise and weakens the zone even further (Braeck and Podladchikov, 2007).

Initial ductile deformation in shear zones may lead to heating, thermal softening and weakening of the rock (Braeck and Podladchikov, 2007; Braeck et al., 2009)

Self-Localizing Thermal Runaway Self-localizing thermal runaway (SLTR) involves no brittle deformation, but rather deformation in ductile shear zones as a precursor to the seismic slip. An increase in strain rate in an already weaker zone leads to temperature rise due to viscous dissipation and further weakening.

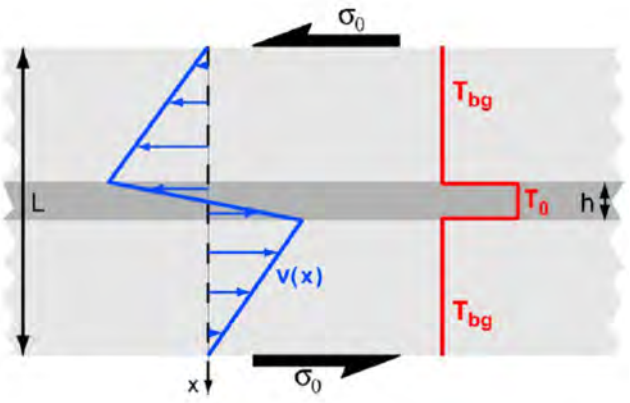

Figure 1.7: *The setup of the 1D viscoelastic slab model of Braeck and Podladchikov (2007). The stress state is simple shear with zero velocity boundary conditions. The shear stress σ is constant throughout the slab, and at $t = 0$ it equals the maximum value σ_0. σ decrease with time due to relaxation and viscous deformation in the interior. The shaded region illustrate a small perturbation in temperature T_0 of width h. The background temperature is T_{bg}. The strain profile has the same geometry as the temperature profile.*

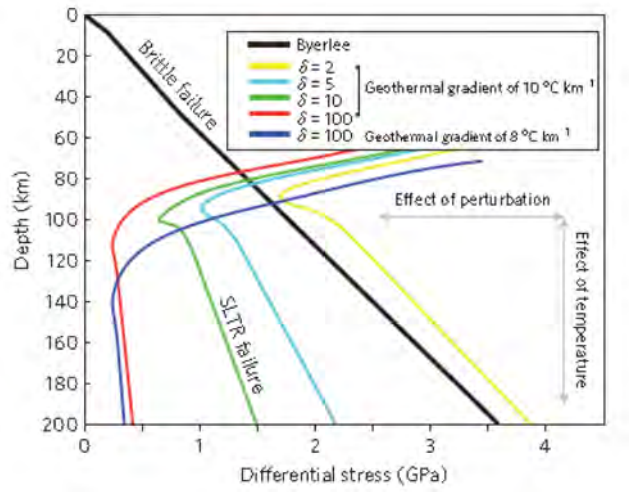

Figure 1.8: *Comparison of failure envelopes of SLTR (colored lines) and Byerlee brittle failure (black line). Different color indicate different SLTR parameters. SLTR occurs at lower differential stresses than brittle failure for a wide range of parameters at depths below 70km. Byerlee brittle failure was calculated assuming fluid pressure = 0. Lower geothermal gradients result in deeper cross-over point whereas bigger perturbations result in lower yield stresses. From John et al. (2009).*

At high stresses viscous dissipation becomes substantial. If heat is generated faster than it is conducted away, the local increase in temperature and strain rate is strongly amplified. This will cause a positive feedback between temperature rise and viscous dissipation to be established, and may result in a thermal runaway (Kelemen and Hirth, 2007). Braeck and Podladchikov (2007) tested the hypothesis of SLTR using a 1D model of a viscoelastic slab, see Fig. 1.7, with an initial positive temperature perturbation in the center, that were subjected to simple shear, see Fig. 1.7.

Kelemen and Hirth (2007) used olivine flow laws for their numerical models of a fine-grained, viscous shear zone in a coarse grained, elastic material. As shear heating became important, a rapid increase in temperature and strain rate were observed. A sudden, dramatic stress drop occurred, followed by low strain rates and cooling.

The SLTR hypothesis is applicable also to field observations by John et al. (2009), and numerical simulations by the same authors supports SLTR being a viable mechanism of intermediate-depth earthquakes. Failure envelopes for numerical simulations, using an initial perturbation in viscosity of less than 1%, show that failure by SLTR occur at lower diffential stresses than brittle failure, see Fig. 1.8. The critical stress required to initiate SLTR is found to depend on the average geothermal gradient and the initial viscosity pertubation (John et al., 2009).

1.3 Geological Setting

The field area in this thesis is located on the northern part of the Holsnøy island, 30 km NW of Bergen, Hordaland, see Fig. 1.9. Holsnøy is part of the Lindås nappe, one of the allochtonous nappes

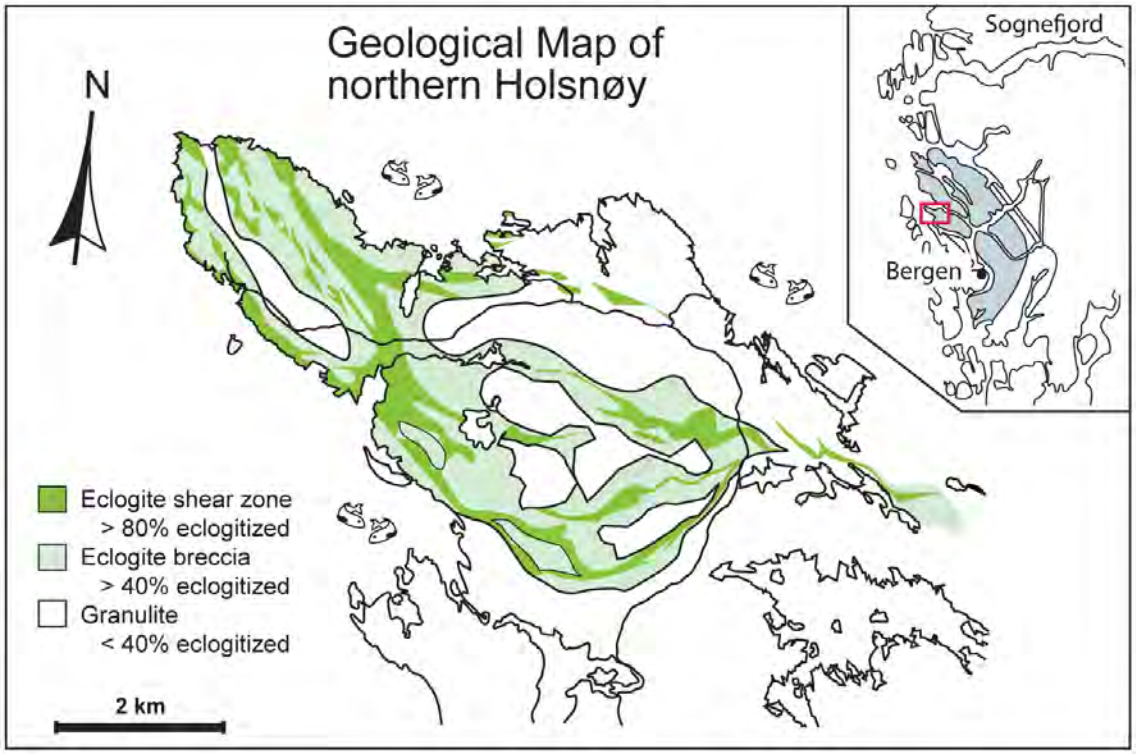

Figure 1.9: *Geological Map of Northern Holsnøy. The map is compliled from work mainly of Austrheim et al. (1996) and Boundy et al. (1997). Inset show the location of the Lindås nappe and northern Holsnøy with respect to Bergen, in western Norway.*

comprising the Bergen Arcs system, see Fig. 1.10. The name Bergen Arcs refers to the arcuate shape of the nappes bent around the city of Bergen.

1.3.1 Tectonostratigraphy of the Caledonides in Western Norway

The present day mountains of Norway is not a result of the Caledonian Orogeny, although this orogenic phase is crucial to understand the tectonostratigraphy observed today. The dominating structure of the Caledonian orogen is thrust-nappe tectonics. The thrust sheets are composed of metasedimentary and igneous rocks, and pre-Caledonian crystalline basement. In the middle 1980´s, Roberts and Gee (1985) grouped the Precambrian basement and Caledonian nappes complexes into the following tectonic units; the Authocthon/Parautochthon, Lower, Middle, Upper, and Uppermost Allochthons. The division was based on general stratigraphical and structural characteristics.

The **Autochthonon/Parautochthon** consist largely of Precambrian crystalline basement (Bryhni and Strurt, 1985; Roberts and Gee, 1985). In the study area i western Norway, the basement rocks are parautochthonous, and its foliation is interpreted as result of lateral displacement. In the literature the Parautochthon east and north of the Bergen Arcs is referred to as the Western Gneiss Region (WGR), and the parautochthon west of it as Øygarden Gneiss Complex (ØGC) (Roberts and Gee, 1985; Roffeis et al., 2012).

The Autochthon/Parautochton are in many antiformal windows overlien by thin sandstones and black shales, representing an important decollement surface at the base of the Lower Allochthon (Roberts and Gee, 1985). Above this westward-dipping **Main Caledonian Thrust** is the **Lower Allochthon**. The sediments of this unit are traditionally interpreted as platform and shelf successions from the Baltican margin Roberts (2003).

The complex is internally imbricated, and psammitic and pelitic metasediments are thrusted together with locally detached basement (Bryhni and Strurt, 1985). Basement rocks are in general only involved in the interior parts of the orogen, and the amounts of Precambrian crystalline rocks increase westwards in the Lower Allochthon. The crystalline rocks are foliated, mylonitized, and have been recrystallized under greenschist and amphibolite facies conditions. Due to the high grade of metamorphism and deformation, the Parautochthon is not easily distinguished from the allochthonous basement in this area. The basement/cover rocks have been referred to as *Caledonized basal gneisses* (Bryhni and Strurt, 1985; Roberts and Gee, 1985).

A **mélange unit** situated structurally above the MCT, and between the Lower and Middle Allochthon, can be traced for more than 400 km. The mélange consists of mantle peridotites, detrital serpentinites, metabasalts, gabbroes and deep basin sediments interlayered with allochthonous, silisiclastic sediments and Proterozoic basement rocks (Andersen et al., 2012). Andersen et al. (2012) interpret this as evidence of a hyperextended Baltican margin with exposed subcontinental mantle lithosphere.

The rocks of the **Middle Allochthon** are mostly Precambrian crystalline rocks, and thick, unfossiliferous metasandstones of late Neoproterozoic age, traditionally considered to be derived from the ancient passive margin of Baltica (Roberts and Gee, 1985; Roberts, 2003).

The thick nappes of crystalline rocks preserve a Precambrian history of development of intense foliation, and mylonitization along the margins, the Jotun nappe beeing an example of this (Roberts and Gee, 1985). The metasediments have been exposed to high ductile strains, resulting in a penetrative foliation, isoclinal recumbent folding, and fold axis rotation (Roberts and Sturt, 1980). The upper parts of the Middle Allochthon are intruded by mafic dykes of doleritic composition (Roberts and Gee, 1985; Roberts, 2003). The Middle Allochthon is structurally a highly heterogeneous complex.

A hyperextended continental margin involving the large crystalline nappes of southern Norway, including the Lindås and Jotun nappes, implies that these nappes may have been separated from Baltica by large rift basins including zones of exhumed mantle. In that case, the Lindås, Upper Bergsdalen and Jotun Nappe complexes can be considered ancient continental ribbons or outboard micro continents(Andersen et al., 2012), instead of originating from the Baltican margin, like suggested by Lundmark et al. (2007) and Roffeis et al. (2012).

Above the nappes of the Middle Allochthon lie the volcanosedimentary rocks of the **Upper Allochthon**. This unit consist of transported island-arc and associated basinal sequences, and in addition fragmented ophiolite, generally accepted to have originated from the outermost margin of Baltica and the Iapetus ocean floor (Roberts and Gee, 1985).

Caledonian thrust nappes positioned above the Köli nappes are only found in north-central parts of Norway. They constitute the **Uppermost Allochthon**, which has been interpreted by Roberts (2003) as exotic carbonate-shelf successions, slope/rise sediments and evolved magmatic arc assemblages of Laurentian or perilaurentian affinity.

1.3.2 The Bergen Arcs System and the Lindås Nappe

The Bergen Arcs System rests in a depression in the Baltic basement, with the Western Gneiss Region (WGR) to the east and Øygarden Gneiss Complex (ØGC) to the west (Roffeis et al., 2012), see Fig. 1.10. Structurally overlying the ØGC are series of arcuate allochthonous units, and sedimentary rocks of Devonian age. The nappes are separated from the ØGC by the Main Caledonian Thrust (MCT). From west to east the units are the Minor Bergen Arc (Minor BA), the Ulrikken Gneiss, the Lindås nappe and the Major Bergen Arc (Major BA)(Kuhn, 2002).

The Major BA is the structurally lowest unit, separated from the WGR by the Bergen Arc Shear

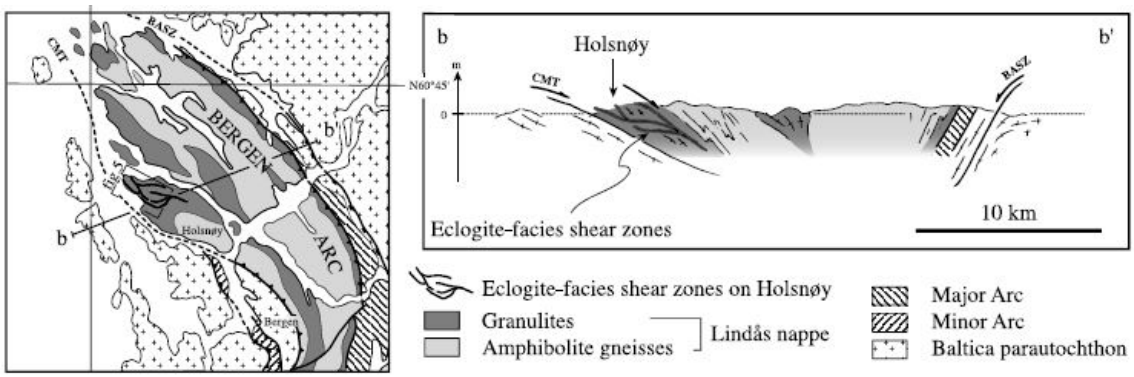

Figure 1.10: *A: Structural sketch of the Bergen Arc (after Ragnhildsveit and Helliksen, 1997). B: Cross section through the Bergen Arc along b-b'. Figure and text from Labrousse et al. (2010).*

Zone (BASZ). The Major BA comprise the Gullfjellet ophiolite and associated magmatic rocks, and overlain marine metasediments. This part of the Bergen Arcs are interpreted to belong to the Upper Allochthon. Structurally above is the Ulrikken Gneiss, a Precambrian granite-migmatite complex with a cover of greenschist facies rocks. It has been correlated with both Middle (Bryhni and Strurt, 1985) and Upper Allochthon (Kuhn, 2002). Between the Major BA and the Ulrikken Gneiss, and structurally overlying the Major BA, is the Lindås nappe (Kolderup and Kolderup, 1940). This nappe is the volumetrically largest nappe in the Bergen Arcs system. Nappes of the Middle Allochthon lying on top of rocks of the Upper Allochthon indicate an inverted tectonostraigraphy in this area, or that the commonly used tectonostratigraphy, outlined by Roberts and Gee (1985) needs a revision.

The Lindås nappe consist mainly of rocks belonging to an anorthosite-mangerite-charnokite-granite (AMCG) suite and banded gneisses (Austrheim and Griffin, 1987; Kuhn, 2002). It is often referred to as the *Anorthosite Complex* in the literature. It mainly consist of granulite facies metamorphic rocks with mulitishelled corona structures. The rocks have undergone extensive amphibolite metamorphism, and parts of it also eclogite metamorphism (Kuhn, 2002).

1.3.3 The Magmatic and Metamorphic History of Lindås Nappe

There are three events which are of great importance in the history of the rocks in the Lindås nappe. First of all, the emplacement of the magmatic complex. The time of emplacement is dated to $1237 + 43 - 35$ Ma for charnockite (U-Pb zircon). For the granulite, ages of 951 ± 2 Ma are obtained, and for amphibolite 957 ± 11 Ma are obtained by Bingen et al. (May, 2001), both using U-Pb zircon. Roffeis et al. (2012) define an age of 969±6 Ma (U-Pb zircon) for emplacement of the jotunite-anorthosite parts of the complex.

During the Sveconorvegian(Grenvillian) orogeny the magmatic rocks were metamorphosed under granulite facies conditions, estimated to 800-900 °C and 10 kbar or more (Austrheim and Griffin, 1985). The age of the granulite metamorphism is $\sim$ 930 Ma (945 ± 5 Ma (Boundy et al., 1997), 929 ± 1 Ma (U-Pb zircon) (Bingen et al., May, 2001), 936 ± 12 Ma (Roffeis et al., 2012)). Corona formation due to a reaction between the primary olivine and plagioclase is characteristic for these rocks. The rocks also developed a generally penetrative foliation during the Sveconorwegian orogeny.

The later metamorphic history of Lindås nappe is enigmatic and highly debated. The Lindås nappe was deformed and metamorphosed during the Caledonian orgeny, which resulted from the continent-continent collision between Laurentia and Baltica starting at 430 ± 3 Ma (Roffeis et al., 2012). The Scandian event led to subduction of the Baltican margin, overlying volcanosediments and earlier

nappes beneath the Laurentian plate, followed by a rapid exhumation and emplacement of thrust sheets onto Baltica (Glodny et al., 2008). The nappe wedge was transported mainly towards the SE (Boundy et al., 1997). This event commonly erased most of the earlier structures (Roberts and Gee, 1985), but the Lindås nappe preserve structures of both Proterozoic and Caledonian age. Parts of the nappe underwent eclogite and amphibolite metamorphism during the Caledonian orogeny (Kuhn, 2002).

Eclogites are only reported from the central/western part of the nappe, in the area from northern Holsnøy, western Radøy, Gaupås, Haukeland to Flesland (Kuhn, 2002). The metamorphic conditions during eclogitization is estimated to $650 - 750°$ C and $15 - 21$ kbar (Glodny et al., 2008; Jamtveit et al., 1990). Austrheim and Griffin (1987) argue that the formation of eclogite was restricted to places where deformation had occurred and fluids were available. Boundy et al. (1997) explain the partly presence of eclogites by a rapid cycling of continental crust through the deepest portions of the orogen and back to upper crustal levels. Both of these explanations leads to preservation of arrested stages of eclogite formation, and survival of metastable granulites through eclogite facies conditions.

Although agreeing that the metamorphic reactions have been arrested due to availability of fluids, some authors, *e.g.*, Kuhn (2002) and Roffeis et al. (2012), regard the Lindås nappe as a crustal section where different parts experienced a different tectono-metamorphic evolution. The southwestern part of Lindås nappe were brought to depths of more than 50 km, and metamorphosed under eclogite facies conditions. At the same time, the northeastern part experienced amphibolite facies conditions and metamorphism at shallower levels. The Lindås nappe is therefore interpreted to represent a natural pressure gradient increasing from ENE to WSW (Roffeis et al., 2012).

Amphibolite facies assemblages are also present in eclogite-bearing domains, the overprint actually is especially evident in these areas. The amphibolite facies retrogression took place at $600 - 690°$C and $8 - 12$ kbar (Bingen et al., 2004; Glodny et al., 2008; Kuhn, 2002).

The tectonic affinity of the Lindås nappe is not fully understood. Lindås nappe has generally been considered part of the Middle Allochton, because of the simailar lithology, and tectonostratigraphic position, as the Jotun nappe (Roberts and Gee, 1985). Wennberg et al. (1998), however, point out differences between the two nappes, and interpret the Lindås nappe as part of the Upper Allochthon, representing fragments of micro-continents from Iapetus. Also, Andersen et al. (2012) suggest that the Lindås nappe is remnants of continental ribbons or micro continents, and therefor not necessarily of Baltic affinity.

A recent paper by Roffeis et al. (2012) supports the general consensus of a correlation between the Lindås nappe and the Jotun nappe, based on ages of formation of the anorthositic-jotunitic member of the complex at 969 ± 6 Ma for Lindås nappe, and work by Lundmark and Corfu (2008) giving 965 ± 4 Ma for anorthosites in the Jotun nappe. The authors concludes that the two nappes had a common origin prior to the Caledonian orogeny, and that they are part of the same tectonic system.

Chapter 2

Methods

2.1 Field Work

The goal of the field work was to collect information on the structural and metamorphic relationships of the fault zones where pst is present at the fault plane, and where the apparent displacement on the fault can be quantified by the presence of a marker. This was done by detailed mapping of faults on meter–scale, and by collecting samples for further analytical studies.

I was introduced to the area and the rocks in the Lindås nappe during the summer and autumn of 2011. The field course in FYS-GEO4200-Case study in Physics of Geological Processes was held at Northern Holsnøy, with focuse on Ådnefjell North, in September 2011. The field area, with the three new localities, was visited two times during the summer 2012; 25th-29th of June and 1st-9th of September.

The field work in June focused on general field observations and collection of samples from Hundkjeften (HK), Ådnefjell south (ÅFS) and Husebøvatnet (HV). The field work in September focused on detailed mapping of the selected outcrops.

2.1.1 Detailed Mapping

Detailed mapping of the faults at selected parts of the outcrops at localities Hundkjeften (Fig 3.5), Husebøvatnet (Fig 3.10) and Ådnefjell South(Fig 3.15) was done on graph paper. A 1 x 1 m grid made of rope and a folding ruler was used to facilitate the mapping. Stike and dip of fault planes, fractures and foliation was measured using a Silva Compass. The right-hand rule was applied.

2.1.2 Drill Core Sampeling

Drill cores were sampeled using a water-cooled, diamond bit Pomeroy EZ Stihl core drill. A paleomagnetic orientation device and a Brunton compass was used for measuring the orientation of the drilled samples (field arrow; trend and plunge of drill core).

- 18 samples were drilled at the Hundkjeften locality, 16 from the fault plane of fault HK, and two from the wall-rock.
- 13 samples were drilled at the Husebøvatnet locality, all from the fault planes of HVa, HVb and HVc.

- 9 samples were drilled at the Ådnefjell South locality, from the fault planes of ÅFSa, ÅFSb, and ÅFSd.

Samples from fault planes were drilled both where the amount of pst on the surface was high, and where it was low. The aim was to get a representative selection regarding the thickness of the pst veins.

2.1.3 Sample Preparation

The drill cores and two hand specimens were cut using a diamond saw at the Natural History Museum, UiO. Thin sections were prepared at the Department of Geoscience, UiO.

2.2 Analytical Techniques

2.2.1 Optical Microscopy

An OlympusBX microscope mounted with a Leica DF320 camera was used for the petrographic observations and obtaining micrographs of the thin sections.

2.2.2 Electron Micro Probe (EMP)

Electron Micro Probe (EMP) analyses were carried out at the Department of Geoscience, UiO. The instrument used is a Cameca SX100 electron microprobe with five wavelength–dispersive spectrometra (WDS) used for quantitative analyses. The EMP has an energy–dispersive system(EDS) used for qualitative analyses, and *i.a.* Back Scatter Electron (BSE) detectors used for imaging. Standard calibration was applied prior to analyses. An accelerating voltage of $15kV$ and a beam current of $15nA$ was applied.

Eight thin sections were analyzed in order to identify the various minerals (qualitative analyses), and to investigate the chemistry of the minerals (quantitave analyses). Microtextures in wall–rock, wall-rock damage zone, and in pst was also examined.

2.3 Estimating the Amount of Melt

2.3.1 Area Method

To estimate the amount of melt preserved on the fault planes the area of pst was measured from detailed map drawn in field for fault HK. The length and width of sections covering the whole fault were measured. The area of injection veins, sidewall ripouts and fragments of pst in the adjacent wall-rock were also measured. The total area of pst was divided by the length of the fault to find the average thickness of melt along the fault plane:

$$t_{pst}[m] = \frac{A\ [m^2]}{L\ [m]},$$

where t_{pst} is the average thickness of the pst, A is the total area of pst measured, and L is the length of the fault.

2.3.2 From thin section

When estimating the amount of melt from thin sections, the thickness of the vein and clasts were measured directly from the most representative section across the pst vein.

2.4 Image Processing and Analysis

To get a more reliable estimate of the amount of material having been through a melt phase image analysis techniques were applied to the fault at HK. In addition to constrain the relative area of clasts vs. matrix in the pst, it also allowed to extract quantitative information on shape and orientation of the particles. Photoshop CS and the signed applet version of ImageJ1.43u were the programmes used.

Chapter 3

Field Observations

3.1 General Field Observations

All studied outcrops at northern Holsnøy are dominated by granulite, eclogite and amphibolite facies rocks (see Chapter 1). The detailed petrography is given in Chapter 4.

The Proterozoic granulite foliation is defined by the elongated pyroxene-garnet coronas and/or layers of pyroxene and garnet ranging in thickness from a few millimeters to several centimeters. The intensity of the foliation varies from one locality to another. Even on meter scale the difference is notable at several outcrops. The orientation of the foliation varies sightly between the granulite domains.

The main Caledonian structures in the area are shear zones and faults. Folds are locally present, but have not been studied in this work. The shear zones tend to be restricted to eclogites, whereas the faults are mostly observed in the granulite. The granulite domains are often seen as blocks and lenses surrounded by shear zones of eclogite, see Fig. 3.1. This is what Austrheim (1990) referred to as eclogite breccia, covering large parts of northern Holsnøy. Eclogitization along fractures in the granulite is also common, like in Fig. 3.1a.

The faults are most commonly parallel to the foliation of the rock, striking approximately N-S, see i.e. , Fig. 3.1c. As there are no other markers than the pyroxene-garnet layers, it is not possible to estimate the displacement on these faults. It is rather rare to find faults striking oblique to the foliation. Those are the ones we mainly are interested in, as the apparent displacement can be measured. Faults like this is found on the three studied localities; Hundkjeften (HK), Husebøvatnet(HV) and Ådnefjell(ÅF).

3.2 Hundkjeften

Hundkjeften is located west of the lake Husebøvatnet, see Fig 3.2. Fig 3.3 gives an overview of parts of the area, with the studied outcrop HK in the center of the image. A dextral fault, referred to as fault HK, that crosses the outcrop in a NNE-SSW direction, was mapped in detail. The rectangle in the field photograph in Fig 3.3 corresponds to the area that was mapped.

The wall rock granulite in the hanging-wall appears more pristine, with a slightly darker gray/lilac color compared to what is observed in the foot-wall. The granulite foliation strikes N-S, see the Stereonet in Fig. 3.6a.

(a) *Eclogitization front along a fracture. The granulite foliation (horizontal) is lost in the part of the rocks that have been altered to eclogite. Folding ruler for scale is 20 cm long.*

(b) *Lenses of granulite surrounded by eclogite shear zones. Notice the difference in orientation of the foliation between the two lenses. Key for scale is ca 8 cm long.*

(c) *Fault with pst oriented (sub)parallel to the granulite foliation and layering in the rock, which is vertical in this picture. Pen and folding ruler for scale.*

(d) *Parts of a former prx-grt-layer floating in eclogite. Notice how the granulite foliation are slightly bent when approaching the eclogite. Pen for scale is 14 cm long, and also indicate the orientation of the foliation.*

Figure 3.1: *Structures and reaction fronts that are typically observed on northern Holsnøy. Photographs (a) and (d) taken at Husebøvatnet, (b) near Hundkjeften, and (c) at Ådnefjell.*

Figure 3.2: *Aerial photograph of Northern Holsnøy. The three localities Hundkjeften, Husebøvatnet and Ådnefjell studied in detail in this thesis,are marked by white circles. Source: Skog og landskap.*

Thick, continous layers of pyroxene and garnet have not been observed at this outcrop, but patches and layers with a higher density of pyroxene-garnet coronas compared to the surrounding rocks are found and define the granulite foliation. This layer enables the apparent displacement on the fault to be measured. A 12 cm thick layer with high density of pyroxene-garnet coronas has been dragged into the fault zone. It is continuous on both sides of the fault plane, see detailed map in Fig. 3.5. Apparent displacement, measured in the horizontal plane, is 62 cm.

A vein of scapolite strikes NE-SW, marked in pale brown in the detailed map, see Fig. 3.5. It can be seen in the photograph in Fig. 3.3, and is off-set by a crossing fault zone with a network of pst.

Fault HK with pst is oriented 028/73, see Fig. 3.6. The total length of the fault, measured on the surface of the outcrop, is 9,4 meters. It terminates at both ends adjacent to eclogite facies shear zones, hence the total original length of the fault is unknown. The shear zone on the NNE end of the fault (on top of the map in Fig. 3.5) is oriented 300/58, while the shear zone on the SSW end (bottom of the map) is oriented 308/63. In NNE the fault splits into two. In SSW the fault plane develops into a horse tail-structure, see Fig. 3.4c, suggesting that this may have been the original termination of the fault. Flow structures have been observed in both shear zones, see Fig. 3.4a for an example.

The geometry of the pst varies along strike, but is mainly a single fault vein with injection veins. The amount of pseudotachylyte present on the fault plane varies along strike, from almost not being visible to the naked eye, and up to 1 cm in thickness. Most commonly the thickness of the pst vein is in the order of 2-4 mm. Several places the pst is branching off the main fault plane. It makes up an anastomozing network of pst, enclosing lenses of wall-rock in between, see detailed map of Hundkjeften. The two SSE-most meters of the fault show a sidewall ripout-geometry.

Injection veins of pst from the fault plane and into the wall-rock is observed. 13 out of 16 injection

veins goes into the footwall, like the ones in Fig. 3.4b. The injection veins either have a crack-like or a void-like geometry, see Fig. 3.4b for an example of both types. The length of the injection veins visible in the field ranges from 1 to 11,5 cm. However, single fragments of pst are observed in the wall-rock. They are disconnected from the fault plane in the section displayed on this outcrop, but are most likely also part of the NNE-SSW striking fault zone. These pst-veins extend about half a meter into the wall-rock. The angle between fault plane and injection vein varies between 12° and 85°. As seen in Fig. 3.6, most of the injection veins have an angle of 90-120° from the strike of the fault plane, inicated by the gray line.

A network of pst striking NW-SE is also observed, see center of Fig. 3.5. It has a 60° angle to the fault HK, described above.

A **network of fractures** crosses the pst, and are observed all along strike of the fault. Some fractures are on the order of one meter in length, and extends up to 1 m into the wall-rock. Most of the fractures are, however, less than five centimeters in length, and restricted to the fault plane and the wall-rock damage zone. There is a much higher number of these shorter fractures compared to the longer ones. In Fig. 3.6 the strike of all 47 measured fractures are presented in a rose diagram. As observed on the detailed map from Hundkjeften, the majority of the fractures are oriented WNW-ESE, with a mean vector of 310°. A small percentage of the fractures have a different orientation (NNE-SSW). Most of those fractures are located near the SSW tip of the fault, associated with the horse tail-structure, see Fig. 3.5.

19 samples were collected from this outcrop at Hundkjeften; HS1 and HK2-HK19. 15 of the samples were drilled from the fault plane, and four from the wall-rock.

(a) *Field photograph of the locality at Hundkjeften. The lake Husebøvatnet can be seen in upper left corner. The black rectangle outline the area mapped in detail (b). The photo is taken looking NE. Persons for scale. Photo: K. Drivdal.*

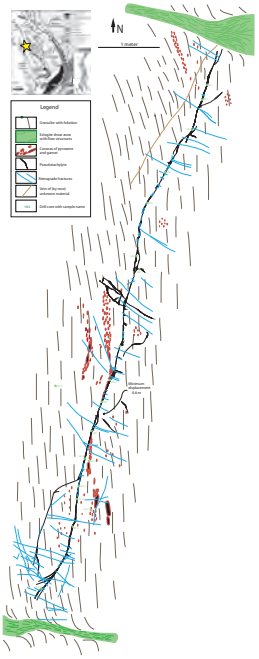

(b) *Small version of the detailed map of the fault at Hundkjeften.*

Figure 3.3: *Overview of the locality Hundkjeften.*

(a) Fault (black lines) terminating in NNE adjacent to an eclogite shear zone (highlighted in green). Notice the flow structures in central parts of the shear zone, and the patches with high density of coronas in lower left corner.

(b) Pst on fault plane oriented vertical in the picture. Injection veins with high angle into the eastern fault block. The uppermost is crack-like, while the lowermost has a void shape.

(c) Termination of the fault in SSW as a horse tail structure. Pst is highlighted in transparent gray. Drill for scale. Photo by T. B. Andersen.

(d) Branched fault plane with pst and injection vein into eastern fault block. Pst highlighted in transparent gray.

Figure 3.4: *Field photographs from fault HK at Hundkjeften. Note that the granulite foliation in general is poorly developed on this locality, and not easily noticed on the photographs. Fig. 3.5 show location of the photos.*

3.3 Husebøvatnet

The Husebøvatnet locality is situated 50 m north of the lake Husebøvatnet, see Fig. 3.2. Fig. 3.7 gives an overview of the locality. Several faults are found at this locality, three of them are HVa, HVb and HVc. HVb was mapped in detail, see Fig. 3.10. Photographs and measurements were taken of HVa and HVc. Samples were collected from all three faults.

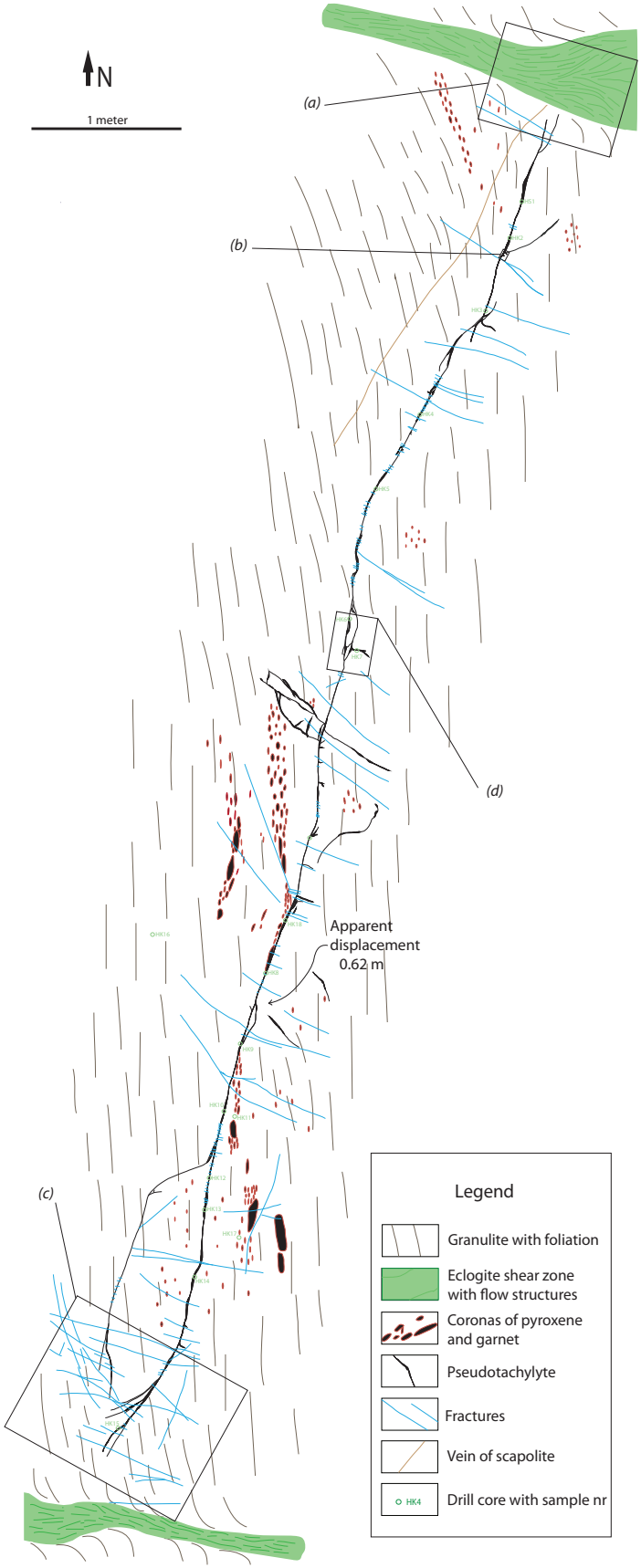

Figure 3.5: *Detailed map of the fault at Hundkjeften. Rectangles correspond to field photos in Fig. 3.4.*

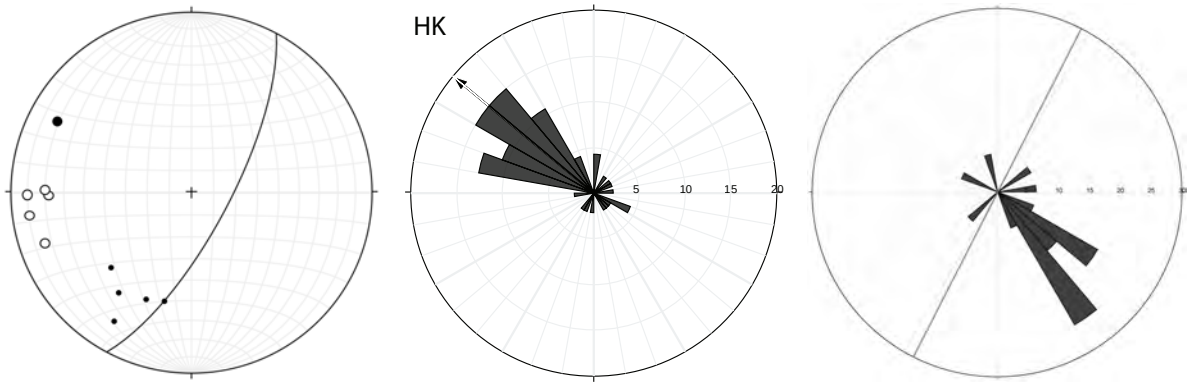

(a) *Stereonet of the fault plane (solid dot and great circle), and foliation (open dots) and fractures (dots) plotted as ploes to the planes. Equal area projection, lower hemisphere.*

(b) *Rose diagram of directions of all fractures measured at HK. The numbers (5-20) indicates % of all values within a certain range. Bin size = 10°.*

(c) *Rose diagram presenting the orientation of the injection veins at fault HK. The gray line indicates the strike of the fault. Most injection veins have an angle of 60-90° to the fault plane, and splays of into the footwall.*

Figure 3.6: *Orientation data from Hundkjeften. Fault plane, foliation and fractures in (a). The dip of the fractures crossing the fault was difficult to measure, so the strike of all measured fractures are presented in the rose diagram in (b). The angle of the injection veins are presented in the rose diagram in (c).*

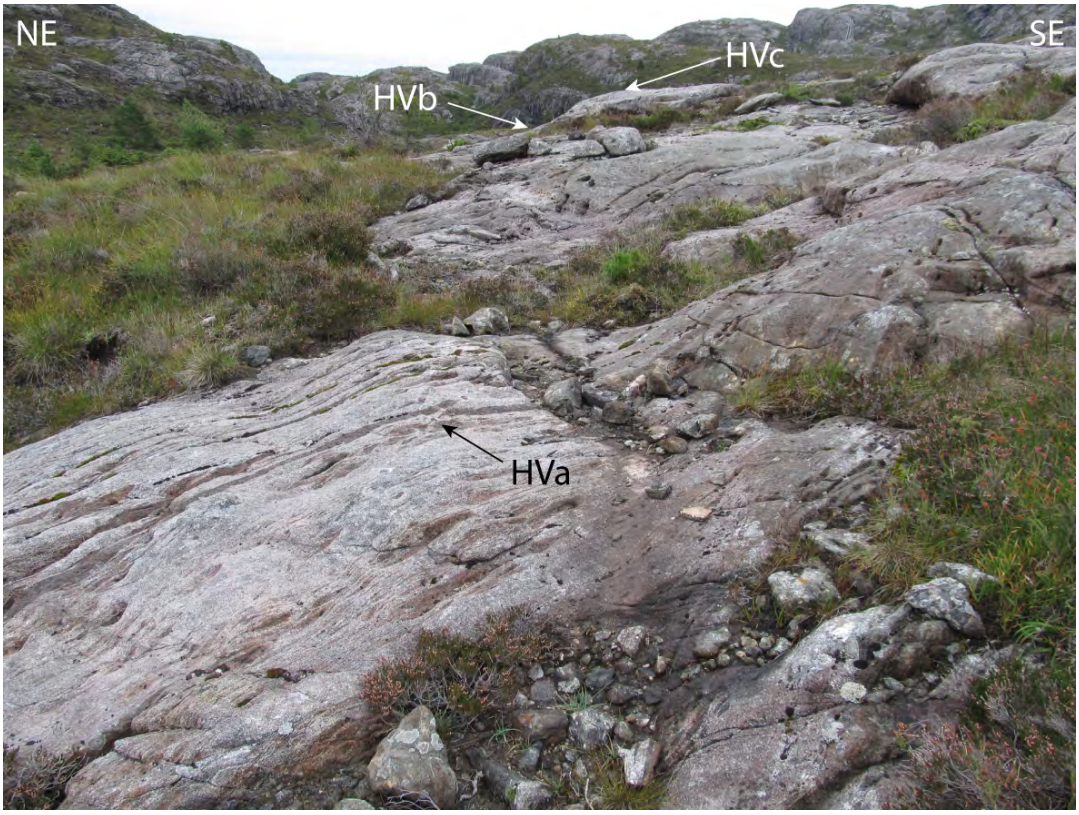

(a) *Field photographs of the locality at Husebøvatnet. Arrows pointing out the location of the three faults we focused on. Photo is taken looking E.*

Figure 3.7: *Overview of the locality Husebøvatnet.*

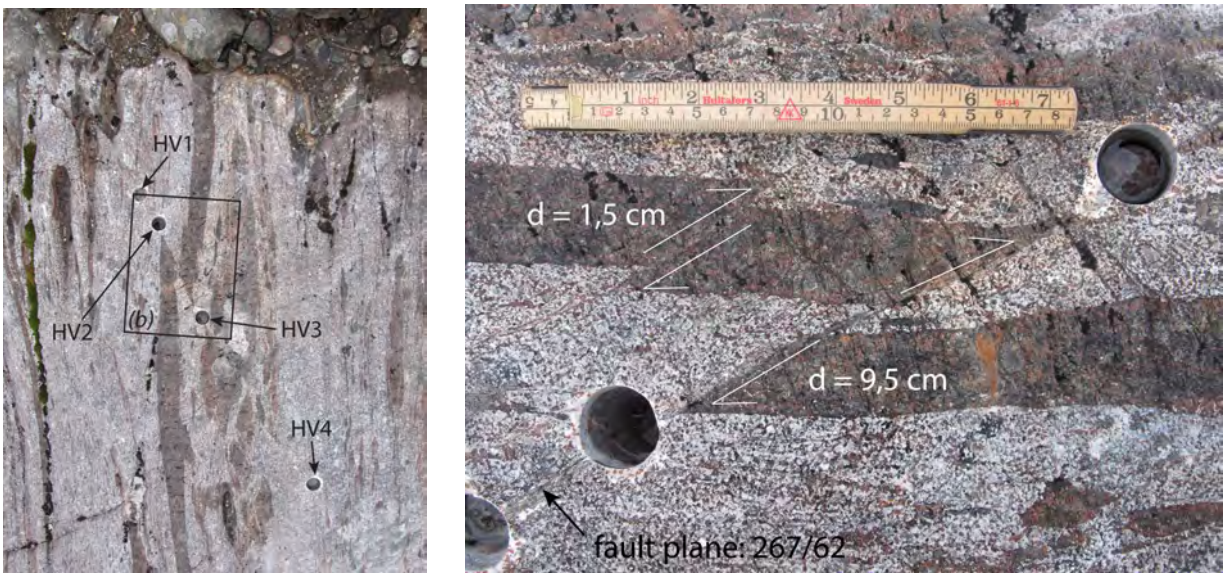

(a) *HVa oriented diagonally, upper left-lower right. Locations of samples drilled from the fault plane are pointed out. Top of photo is to SE.*

(b) *Close up on the fault plane and the offset px-grt layer. HVa has an apparent displacement of 9.5 cm. The arrows indicate the relative direction of movement on the faults.*

Figure 3.8: *Field photographs of the fault HVa. The black rectangle in (a) corresponds to (b) when rotated 90 degrees counterclockwise. Drill holes 2.5 cm in diameter as scale.*

At Husebøvatnet the granulite foliation is well developed and strikes NW-SE. The rose diagram in Fig. 3.11 gives a presentation of the measurements. Continuous centimeter thick layers of pyroxene-garnet are common. They make up the markers for fault-offsets. Coronas of pyroxene and garnet in all sizes, from 1 to ∼30 cm in the longest direction, are commonly present. This locality has a higher amount of mafic layers, and are more banded, compared to the locality at Hundkjeften.

3.3.1 Fault HVa

The dextral E-W striking fault HVa can be traced for a few meters across the outcrop. The fault plane of HVa is oriented 267/62, see Fig. 3.11. HVa offsets several coronas, but the displacement is most easily observed where the fault sharply cuts a five cm thick pyroxene-garnet layer, see Fig. 3.8. The foliation-parallel marker has not been dragged into the fault zone, hence the fault sharply cuts the foliation. Measured on the subhorizontal surface of the outcrop, the apparent displacement of HVa is 9,5 cm, see Fig. 3.8. Another fault in immediate vicinity has an apparent displacement of 1,5 cm. A mm-thick vein of pst is observed on parts of the fault plane of HVa, see Fig. 3.8. No injection veins of pst were observed in the field.

The directions of all fractures at HVa are located within a range of 30°. They are all oriented NNW-SSE, see the rose diagram in Fig. 3.11.

Four samples were drilled from HVa; HV1-HV4.

3.3.2 Fault HVb

The dextral N-S striking fault HVb can be traced for 1,4 m on a subhorizontal part of the outcrop. The fault plane is curve-planar; from it's southern tip HVb strikes NNW-SSE (341/55 measured in drill hole HV6), and further north it strikes NNE/SSW, see detailed map in Fig. 3.10. The fault

off-sets a 3 cm thick pyroxene-garnet layer, which is dragged into the fault zone and cut off. The photograph in Fig. 3.9b, taken prior to drilling, show the apparent displacement of 5,2 cm. On this particular part of the outcrop, the well-developed granulite foliation is found about 10 cm into the eclogite bodies, see Fig. 3.10. The foliation is slightly bent in parts of the eclogite. This is illustrated in the detailed map in Fig. 3.10.

Pst is found on the fault plane, and the amount varies along strike. The common thickness is 1-3 mm, but thicknesses up to 1 cm is observed. The fault is branched, and pst encloses lenses of granulite, see center of Fig. 3.10.

Several fractures truncate the outcrop, see detailed map of fault HVb in Fig. 3.10. The rose diagram in Fig. 3.11 indicate that there are two fracture populations, one oriented NNE-SSW, the other NNW-SSE. Fractures from both populations are found in both granulite and eclogite. Some fractures are restricted to eclogite, see middle right in Fig. 3.10, and others fractures are restricted to the granulite. Notice that no fractures are observed perpendicular to the fault plane, like at Hundkjeften, and that all are relatively long. The density of fractures are also much lower compared to at fault HK. Only one fracture is observed crossing fault HVb.

Five samples were drilled from HVb; HV5-HV9. See detailed map in Fig. 3.10 for locations of samples.

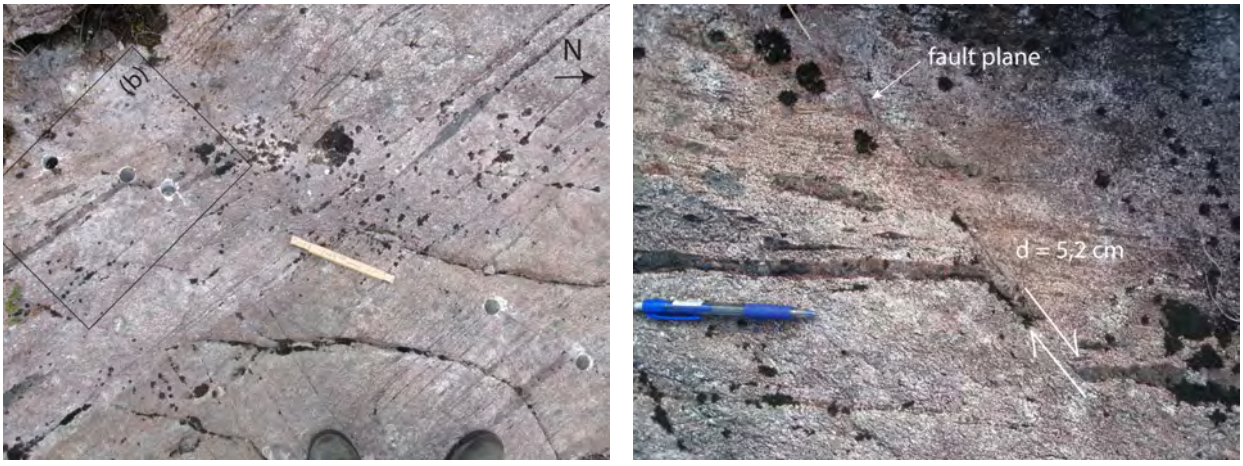

(a) *Fault HVb oriented subdiagonal, upper left-lower right. Detailed map of HVb can be found in Fig. 3.10. Notice the foliation also in parts of the eclogite.*

(b) *Close up of the marker (horizontal) visualizing the apparent displacement of the fault (upper left-lower right). Arrows indicate the relative movement of the fault. A 14 cm long pen for scale.*

Figure 3.9: *Field photos of fault HVb. The rectangle in (a) corresponds to (b) after drilling of samples.*

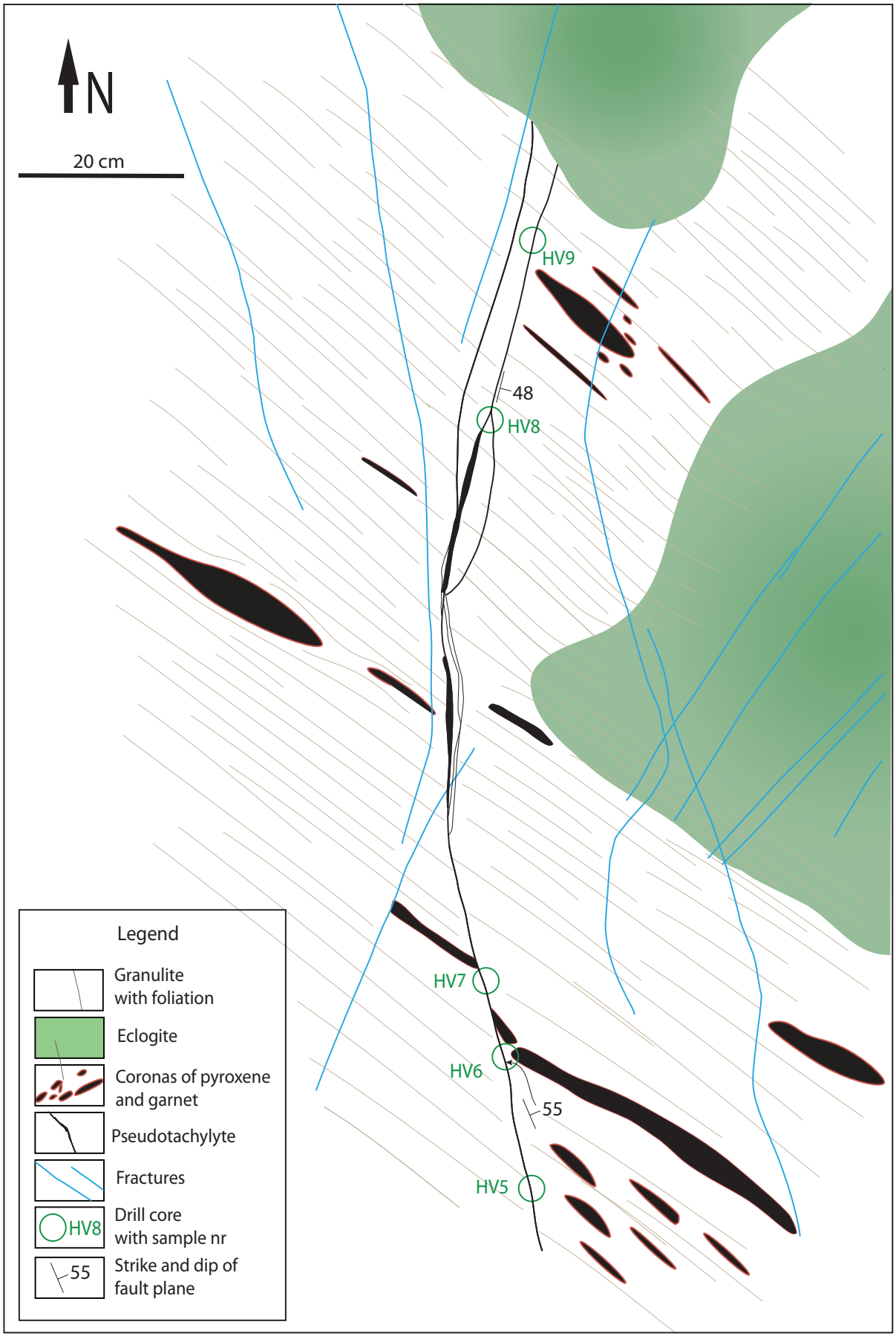

Figure 3.10: *Detailed map of the fault HVb at Husebøvatnet.*

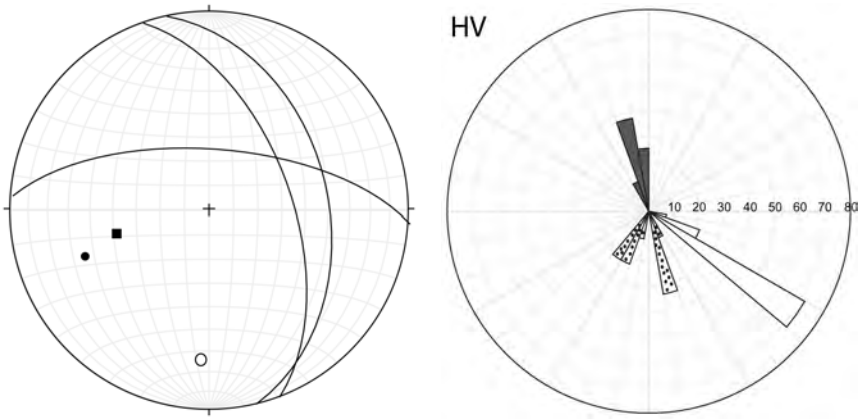

(a) *Stereonet of the fault plane of HVa (open dot), HVb (solid dot) and HVc (square) plotted as poles to the best sylindrical fit of the planes. Equal area projection, lower hemisphere.*

(b) *Rose diagram presenting the direction of the foliation (open sectors), and the directions of fractures associated with the faults HVa (gray sectors) and HVb (dotted sectors).*

Figure 3.11: *Orientation data from the locality Husebøvatnet. Fault planes in (a), and foliation and fractures in (b). Numbers in (b) (10-80) indicate % of all values within the certain range. Bin size = 10°.*

3.3.3 Fault HVc

The dextral fault HVc is located only decimeters from HVb, and the two faults have almost the same orientation, see stereonet in Fig. 3.11. A connection between the two faults were not found in the field, so they are treated as two individual faults.

HVc can be traced for more than five meters, the field photos in Fig.3.12 only covering the northernmost part of the fault. HVc is oriented 347/41, see stereonet in Fig. 3.11. The displacement is visualized by a pyroxene-garnet layer off-set by 16 cm. Displacement on the fault is measured from the field photograph in Fig. 3.12b.

Pst is observed all along the strike of the fault. On photos it may look like the thickness of the veins in some places are several centimeters. This is due to erosion of the wall rock in places where the dip of the fault and dip of the surface of the outcrop are approximately equal. Common thickness of pst observed in the field is 2-4 mm.

Four samples were drilled from this fault;, HV10-13. See Fig. 3.12 for location of the samples.

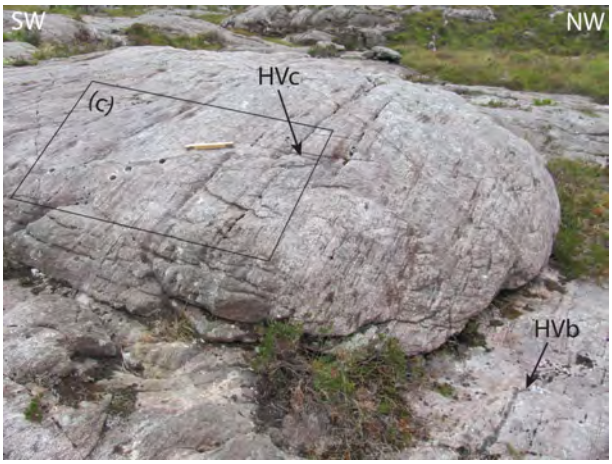

(a) *Overview of the outcrop where HVc are located. Parts of HVb is also visible in lower left corner.*

(b) *Close-up of the px-grt layer offset by the fault (horizontal) with 16 centimeters. Arrows indicating relative movement on the fault.*

(c) *Location of samples drilled from HVc (subdiagonal). Folding ruler for scale.*

Figure 3.12: *Field photographs of the fault HVc. The rectangle in (a) corresponds to (c), and the rectangle in (c) corresponds to (b).*

3.4 Ådnefjell

The locality of Ådnefjell is situated at Ådnefjell, east of Eldsfjellet and the road Fv249, see Fig. 3.2. The well-developed foliation is oriented ENE-WSW. The stereonet and rose diagram in Fig. 3.14 gives a presentation of the measurements. A high number of flattened pyroxene-garnet coronas with very high aspect ratios are present.

Three faults at this outcrop cross-cut the foliation; ÅFSa, ÅFSb and ÅFSd. Foliation-parallel layers of pyroxene (and garnet) act as markers. One foliation-parallel vein of pst was observed; ÅFSc. ÅFSa was mapped in detail, the map is showb in Fig. 3.15. Pictures and measurements were taken of ÅFSb, ÅFSc and ÅFSd, and they are only briefly described. Fig. 3.13 give an overview of the outcrop, and the location of the four faults are pointed out.

Pst is present on all four fault planes, and samples were collected from all four faults.

Figure 3.13: *Field photo of the locality at Ådnefjell. Photo is taken looking NE. Photo by K. Drivdal.*

3.4.1 Fault ÅFSa

The detailed map of the sinistral fault ÅFSa is shown in Fig.3.15. The fault is oriented 145/51, see stereonet in Fig.3.14. ÅFSa can be traced for approximately 2,5 m on the eastward dipping surface of this outcrop.

The apparent displacement on ÅFSa is 5,5 cm, visualized by an E-W striking pyroxene layer that is sharply off-set. This can be seen between drill hole ÅFS3 and ÅFS4 in the detailed map in Fig.3.15. A field photograph of the marker is shown in Fig.3.16b. A thin vein of pst is observed on the fault plane. The thickness varies slightly, but is commonly 1 mm. The fault branches off the main fault plane four places along strike, but no injection veins were observed in the field.

The rose diagram in Fig.3.14 gives a presentation of the strike of the fractures associated with ÅFSa and the surrounding wall-rock. Approximately 50 % of the measured fractures strikes NNE-SSW,

within a range of 20°. The fracture population is oriented with an high angle to the foliation, and approximately 30/60° to the fault plane. The length of the fractures varies from 30 cm to 1,5 m.

Fives samples were collected from ÅFSa; ÅFS1-ÅFS5. For location of the samples, see detailed map in Fig. 3.15.

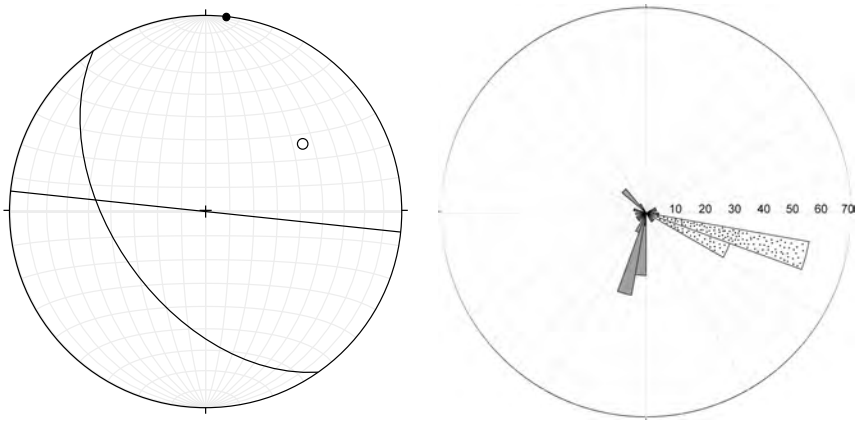

(a) *Stereonet of foliation (solid dot) and fault plane ÅFSa (open dot) at Ådnefjell, plotted as poles to planes of cylindrical best fit of greate cirles. Equal area projection, lower hemisphere.*

(b) *Rose diagram from Ådnefjell presenting the direction of the foliation (dotted sectors) and fractures associated with the fault ÅFSa (gray sectors). Numbers (10-70) indicate percentage of all values within a certain range. Bin size = 10 degrees.*

Figure 3.14: *Orientation data from the locality Ådnefjell. Fault plane of ÅFSa and foliation in (a), and direction of fractures associated with ÅFSa and all measurements of foliations in (b).*

3.4.2 Fault ÅFSb

The dextral fault ÅFSb is oriented 077/88. Three samples were collected from the fault plane of ÅFSb; ÅFS6-8. The discplacement turned out to be indeterminable, and no more work have been carried out on this fault.

3.4.3 Fault ÅFSc

The fault ÅFSc is oriented parallel to the foliation, see Fig. 3.16. An overview of the fault is also shown in Fig. 3.1c. Because of the foliation-parallel orientation of the fault a measure of the apparent displacement is not found. This pst vein is is much thicker compared to all other observed on the outcrops in this study. It varies slightly, but is up to ∼12 cm, see Fig. 3.16c. NOt easily observed on the field photographs, the vein geometry of fault ÅFSc is complex, involving

One sample was collected form this fault; ÅFS9, a hand specimen from the margin of the pst, to examine the microstructures.

3.4.4 Fault ÅFSd

The dextral fault ÅFSd is oriented 96/90. The displacement is 12,5 cm, see Fig. 3.16, visualized by a marker dragged into the fault zone. A pst vein of commonly 1-2 mm was observed on the fault plane.

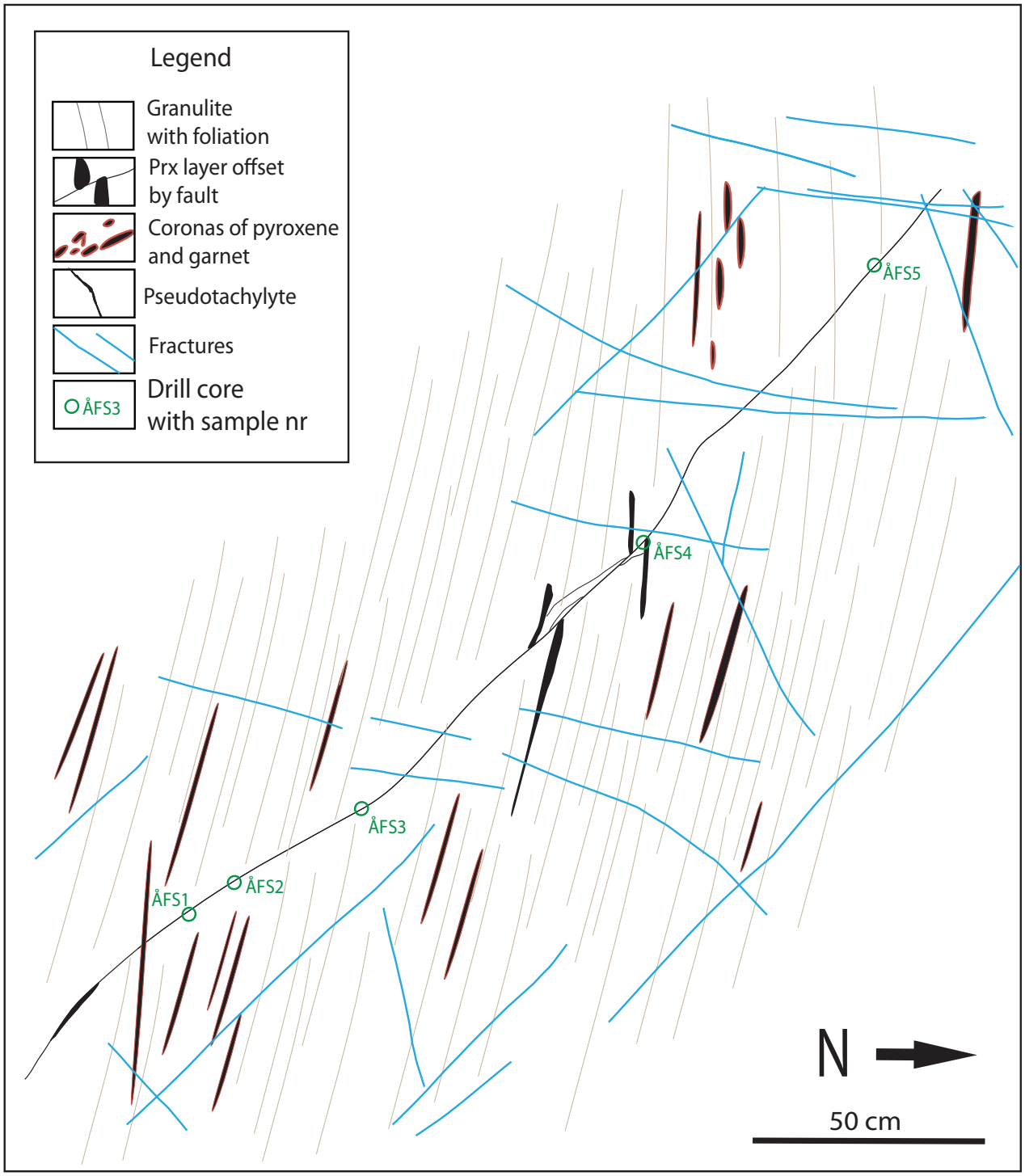

Figure 3.15: *Detailed map of the fault ÅFSa.*

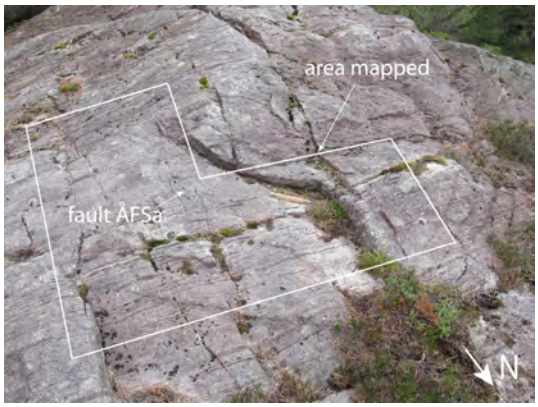

(a) ÅFSa. Area outlined in black corresponds to area mapped in detail.

(b) ÅFSa, upper left-lower right. Location of samples pointed out.

(c) ÅFSc, parallel to the foliation. The white box is parts of (e).

(d) ÅFSd running vertical. Relative movement of fault indicated by arrows. Marker bent in towards the fault plane.

(e) ÅFSc

(f) ÅFSd

Figure 3.16: *Field photos of the investigated fault at Ådnefjell; ÅFSa, ÅFSc and ÅFSd.*

This page intentionally left blank

Chapter 4

Petrography

This chapter is based on observation of thin sections by using optical microscopy and by using EDS and WDS system at the EMP. The presentation of the petrography is divided into the three field localities, and for each of them the wall-rock, the wall-rock damage zones and the pseudotachylytes are described.

Mineral abbreviations after Siivola and Schmid (2007).

In Appendix, images of scans of thin sections used for images are listed. Exception are the thin sections included in the main document, that will not be shown twice. The different sections of the thin section used in various figures in this chapter is marked by rectangles and figure number.

4.1 Hundkjeften

Thin section HK16, drilled in the wall-rock 70 cm off the fault plane of fault HK, is a granulite that show evidence of incipient amphibolite facies metamorphism. The mineralogy include both the pristine Precambrian granulite facies assemblage and the Caledonian amphibolite facies assemblage.

4.1.1 The Pristine Wall-Rock

The Precambrian granulite facies mineral assemblage in this area is plagioclase+garnet+clinopyroxene +orthopyroxene+scapolite±spinel±amphibole±Fe-Ti-oxides (Kuhn, 2002).

The texture of the wall-rock is largely polygonal, with most of the grains intersecting at 120° angles to each other.

Plagioclase is the main mineral in the wall-rock, and constitutes $\sim 70 - 80\%$ of the modal composition. The grain sizes range from 500 μm and up to 5 mm. The plagioclase show a variety of twinning structures, both growth and deformation twins; albite, periclase, carlsbad, see Fig. 4.1b and 4.1c. Away from the fault plane the plagioclase is pristine, with few inclusion and fractures. Crystals are mostly subhedral to euhedral, although some grains have a lobate shape, see Fig. 4.1. Also, in Fig. 4.4a the plagioclase in the upper left part of the image is relatively undisturbed. The garnet-pyroxene band seems to have taken much of the deformation, as it is heavily fractured. When approaching the fault plane, the number of fractures in general increase. Centimeters away from fault plane, the orientation of the fractures locally follow the same direction as the fault plane.

The plagioclase in the wall rock also show evidence of having undergone ductile deformation. Grains record pinning structures as a result of grain boundary migration (GBM), see Fig. 4.1c. Closer to the fault plane the growth twins are destroyed, see Fig. 4.4e. Larger grains on the margin to the wall-rock damage zone are partly bent towards this zone, and show undulose extinction, see Fig. 4.4e.

Pyroxene constitutes ∼10% of the wall-rock, not encountering the cm thick layers with high density of of garnet-pyroxene coronas distributed variably throughout the wall-rock at Hundkjeften. Both clinopyroxene and orthopyroxene are found, but the dominant phase observed is clinopyroxene. The crystal habit is euhedral to subhedral, see Fig. 4.4a. Cleavages in primary pyroxene are observed. Pyroxene is locally associated with amphibole, see Fig 4.1b. Secondary clinopyroxene (cpx2) is observed in reaction rims. The pyroxene is more intensely fractured closer to the fault plane, apparently in random directions, like observed in Fig. 4.4a.

Garnet constitutes ∼10% of the wall-rock, not encountering the cm thick layers with high density of of garnet-pyroxene in the wall-rock. Crystals are euhedral to subhedral, see Fig. 4.1b. Grain size range between 400 μm and 2 mm. The garnets are variably fractured. In some cases the distribution and orientation of the fractures are apparently random, while in other cases one or a few orientations are favoured.

Scapolite is euhedral to subhedral, with grain sizes of ∼200 μm. It often has a high number of inclusions compared to the surrounding plagioclase.

Spinel is found in small amounts. The crystal habit is subhedral to anhedral, and the grain size is ∼500 μm. These dimensions may not reflect the size of the original crystals, as spl is mainly observed as the core of coronas, surrounded by corundum+garnet+
amphibole+clinopyroxene2, see Fig. 4.1f.

Amphibole is found in reaction rims (Fig. 4.1f), in association with clinopyroxene (Fig. 4.1b), and as fill in fractures. The amphiboles have an anhedral crystal habit, and no cleavages are observed.

Fe-oxides are observed in reaction rims between scapolite and clinopyroxene, and also variably distributed in small amounts elsewhere in the wall-rock.

4.1.2 The Wall-Rock adjacant to the Fault Zone

In addition to the granulite facies assemblage, including the minerals described above, Caledonian eclogite and amphibolite facies assemblages have also been reported from this area, *e.g.*, by Austrheim and Griffin (1987) and Kuhn (2002). The Caledonian amphibolite facies assemblage is plagioclase+zoisite+K-feldspar+amphibole+garnet2+qartz+mica+kyanite+corundum+Fe-sulphides.

Zoisite and **K-feldspar** are observed in symplectites on plagioclase-plagioclase grain boundaries and in fractures. Zoisite is also found as needles growing on plagioclase.

Corundum is found in coronas in association with spinel and garnet, see Fig. 4.1f.

Symplectites of K-feldspar and zoisite (both detected by EDS) are observed on grain boundaries and in fractures in the wall rock, see Fig. 4.1b, 4.1d and 4.5b. In plane polarized light (ppl) they appear as dark feathery crystals, see Fig. 4.1b, and in BSE-images, Fig. 4.1e, as alternating gray (K-feldspar) and pale gray (zoisite). Their orientation of growth with respect to the grain boundaries and fractures is random. The size of the symplectites are up to 100μm in the longest direction. Kuhn (2002) observed the same intergrowth at plagioclase-plagioclase boundaries in the most pristine granulites from Holsnøy in clsoe spatial relation to eclogite, and interpret this as incipient eclogitization of the granulite.

Tiny needles of what is probably kyanite are found in contact with, or in vicinity of, the symplectites, where they are associated with Ab-rich plagioclase. The kyanite needles are also present in plagioclase.

Aggregates of spinel and garnet1 with rims of corundum+garnet2+clinopyroxene2±amphibole is shown in Fig. 4.1f. The surrounding mineral is plagioclase.

The transition from wall-rock to pst is either a sharp and intrusive-like contact, or it includes a zone of highly deformed and damaged wall-rock in between. Both types of transitions between wall-rock and pst is found along the fault plane of HK at the Hundkjeften locality. Where the contact between wall-rock and pst is sharp, mineral grains in the wall-rock are sharply truncated by the pst, e.g. , plagioclase without showing any bending of the twin lammelae towards the fault plane, see Fig. 4.2a. Garnets in direct contact with the pst are either cut sharply off, see Fig. 4.2b, or, the pst makes an embayment where the grain originally was situated, like in Fig. 4.5c. Parts of the garnet may still be left beyond the pst-embayment. This selective melting of garnet is previously described by Austrheim et al. (1996), who observed both garnets cut sharply off, that apparently contibuted to the melt, and embaymets of pst into garnet.

4.1.3 The Wall-Rock Damage Zone

The zone of highly fractured, damaged and deformed wall-rock associated with pst is here referred to as the wall-rock damage zone, abbreviated *wrdz*. Where the wrdz is present, the thickness varies along strike of the HK fault, ranging from a few mm to 1 cm, see *e.g.*, Fig. 4.4e for a section.

The wrdz is distinguished from the wall-rock itself, like in Fig. 4.4c and Fig. 4.4e, due to an abrupt and drastic reduction in grain size from the wall-rock to the wrdz. The fine grained material in the wrdz have grain sizes of 10-50μm, see Fig. 4.4d. In Fig. 4.5a the slight variation in grain sizes in the crushed material can be observed. White plagioclase clasts is a bit larger than the rest, and the dark phase, horizontally oriented in the middle of the image is garnets that are aligned or streched. BSE-images of the wrdz, in Fig. 4.4d and Fig 4.6e, show that the grains are angular to subrounded. The plagioclase is surrounded by a lighter gray phase which is a feldspar with a higher content of Ca (detected by EDS).

In addition to the crushed material described above, the wrdz also consists of larger grains that have experienced severe deformation resulting in a high density of fractures, see Fig. 4.5f, and/or an undulous extinction. Twinning lammelae in higly deformed plagioclase show that grains are bent. Plagioclase also go extinct, from left to right, at different angles as the microscope stage is turned. In the lower right corner of Fig. 4.4a and in Fig. 4.4b examples of such grains with undulose are shown.

The wrdz is not only observed outside the pst fault vein, like in Fig. 4.5a and Fig. 4.5f, but also in between double planes of pst, like in Fig 4.5e. Also here the material is highly fractured, although not as extensive as in the wrdz outside pst. Fig 4.3a is a scan of the thin section HK2, and show the location of Fig. 4.5c with respect to the fault zone.

The origin of the wrdz will be discussed in Chapter 7.

4.1.4 The Pseudotachylyte

The pst of fault HK has an amphibolite facies mineralogy. The mineral assemblage of the matrix is plagioclase+amphibole. Tiny needles found all over the pst are suggested to be zoisite, but they are to small to give clean EMP-analyses.

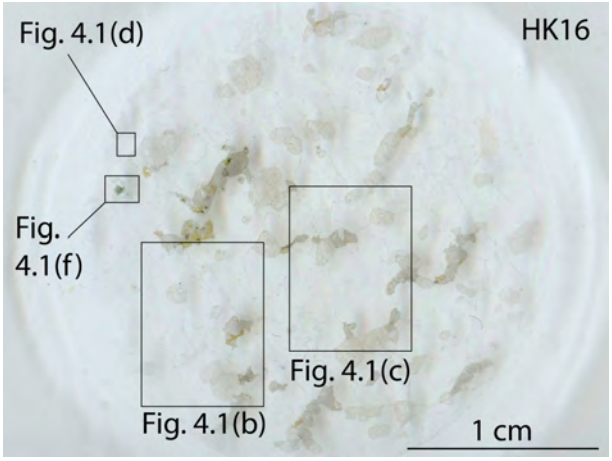

(a) Scan of thin section HK16 from wall-rock granulite.

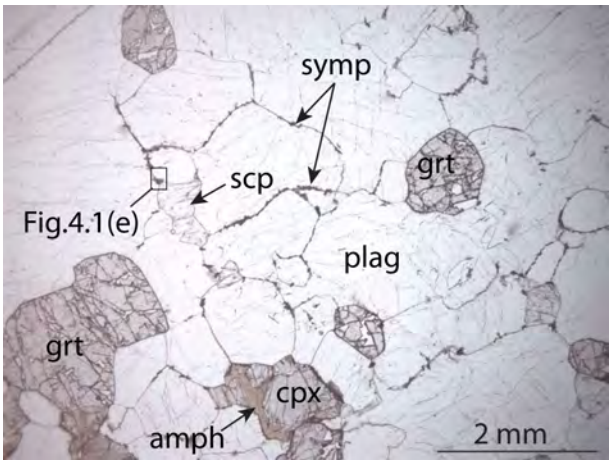

(b) The main minerals in the wall-rock is pointed out. Symplectite of K-feldspar and zo is observed on grain boundaries (HK16, ppl).

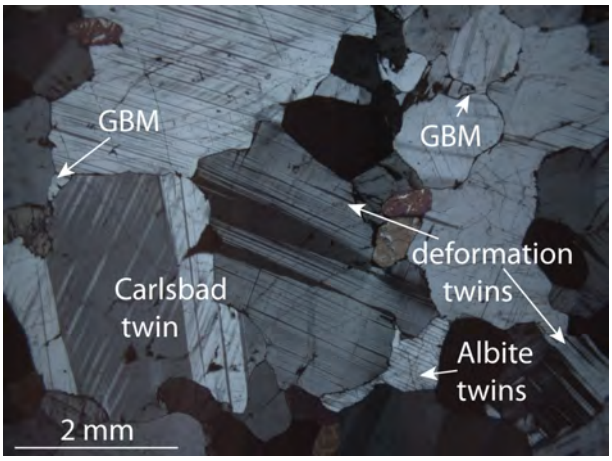

(c) Growth twins, deformation twins and grain boundary migration observed in plag (HK16, xpl).

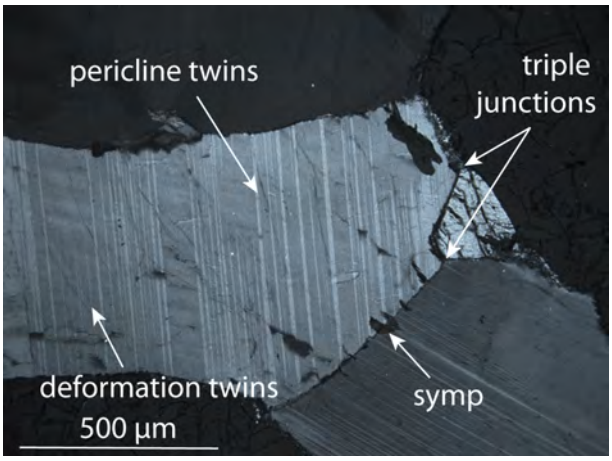

(d) Typical polygonal texture in plag, with grains intersecting at 120°. Note twins in plag and symplectites on grain boundary (HK16, xpl).

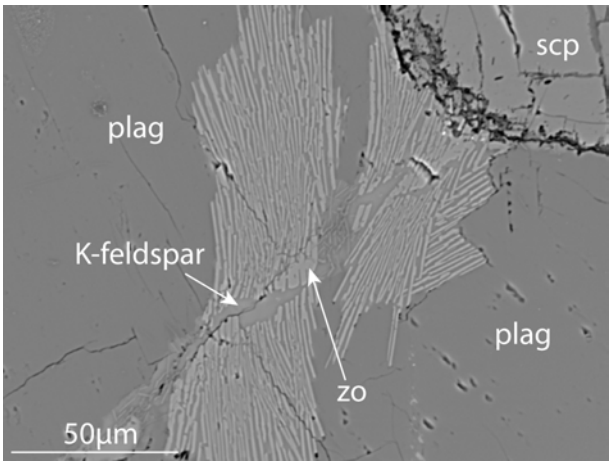

(e) Symplectite of K-feldspar and zo on plag-plag grain boundary (HK16, BSE)).

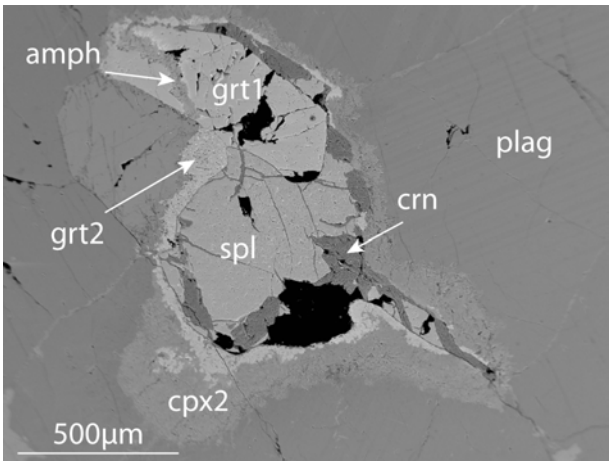

(f) Aggregate of spn+grt with reaction rims of crn+cpx2 (HK16, BSE).

Figure 4.1: *Scan(a), micrographs(b-d) and BSE-images(e-f) illustrating the mineralogy, microtextures, and reactions that indicate incipient amphibolite metamorphism of the wall-rock at Hundkjeften.*

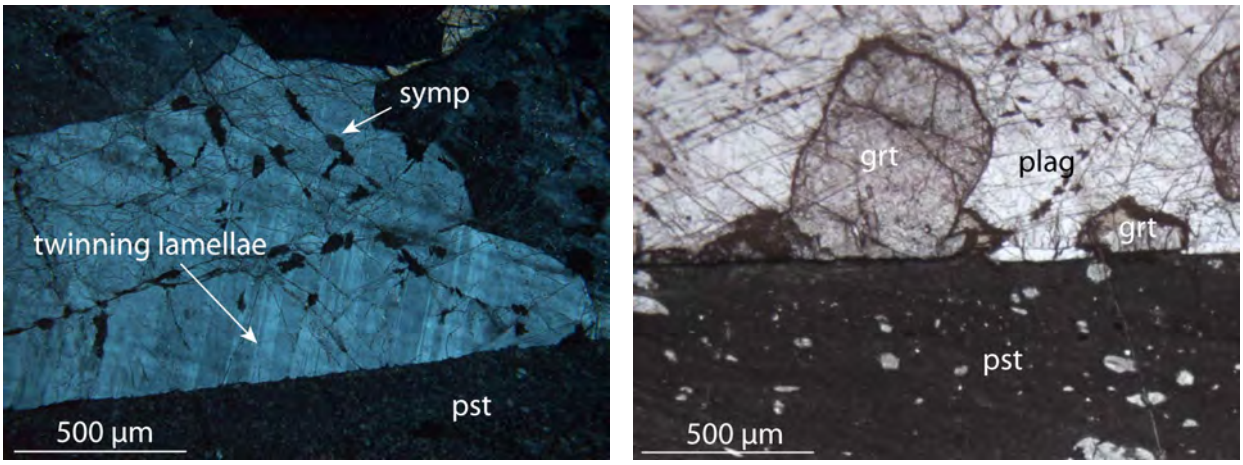

(a) Plag cut sharply off by pst. Symplectite on fractures in plag pointed out (HK4, xpl).

(b) Garnet cut sharply off by pst. Symplectites in fractures oriented sub-parallel to the fault plane (HK4, ppl).

Figure 4.2: *Micrographs of an intrusive-like contact between wall-rock and pst of fault HK.*

The vein geometry of fault HK varies along strike. In most of the thin sections investigated, fault HK has the geometry of a single fault vein, like observed in e.g. , thin section HK4 in Fig. 4.3b. Fig. 4.5a is a micrograph of parts of this fault vein, with one sharp contact to the wall-rock, and a wrdz on the opposite side. Nearly orthogonal injection veins are observed in both fault-blocks. The continuation of the injection vein pointing upward in the image in Fig. 4.5a is displayed in it's full length in Fig. 4.5d. This injection vein has a clean fracture-type geometry, although slightly undulating, and it penetrates both plagioclase, pyroxene and garnets. Flow structures are visible, as pointed out by the arrow. Fractures point in different directions from the tip of the injection vein and further into the wall-rock.

A close-up on the injection vein that splays off the opposite side of the pst is displayed in Fig. 4.5b. This injection vein penetrates the wrdz before entering the wall-rock. This vein does not show flow structure similar to the injection vein in Fig. 4.5d, and the border to the adjacent rock is not as sharp. A possible explanation for this could be that the fine grained intruded material of the wrdz behave different and less coherent than the massive wall-rock. The implications of the pst injection vein cross-cutting the wrdz will be discussed in Chapter 7.

In Fig. 4.5f a micrograph from HK4 (the same thin section as the previously described injection veins), show two pst injection veins in the wrdz. One is orthogonal to the fault vein, while the other is oriented sub-parallel to the fault vein. Remains of highly fractured plagioclase is observed in the wrdz outside the sub-parallel injection vein. The sub-parallel injection vein is longer and wider than the orthogonal vein, and also host clasts and aggregates of minerals. It has an irregular shape, with alternating thicker and thinner units.

Injection veins of both irregular and clean fracture-type geometries splaying off a fault vein are displayed in Fig. 4.5c. This image also show the embayment of pst where only parts of the garnet crystal is left. The wall-rock seems greatly affected by the irregular injection veins in the upper part of the image, and what resembles a wrdz have been developed around them.

Parts of fault HK also have the geometry of a paired slip zone with variable amounts of pst on the slip planes, like in thin section HK2 (Fig. 4.3a). The subparallel paired slip planes are connected by fractures and veins of pst of highly irregular geometries, see Fig. 4.5e. In this Fig the slip planes are oriented subhorizontal, the one named *pst fault vein*, significantly thicker than the other. The material between the slip surfaces is highly damaged in this particular area, but almost undisturbed lenses of wall-rock enclosed by pst is also observed along the fault plane of HK.

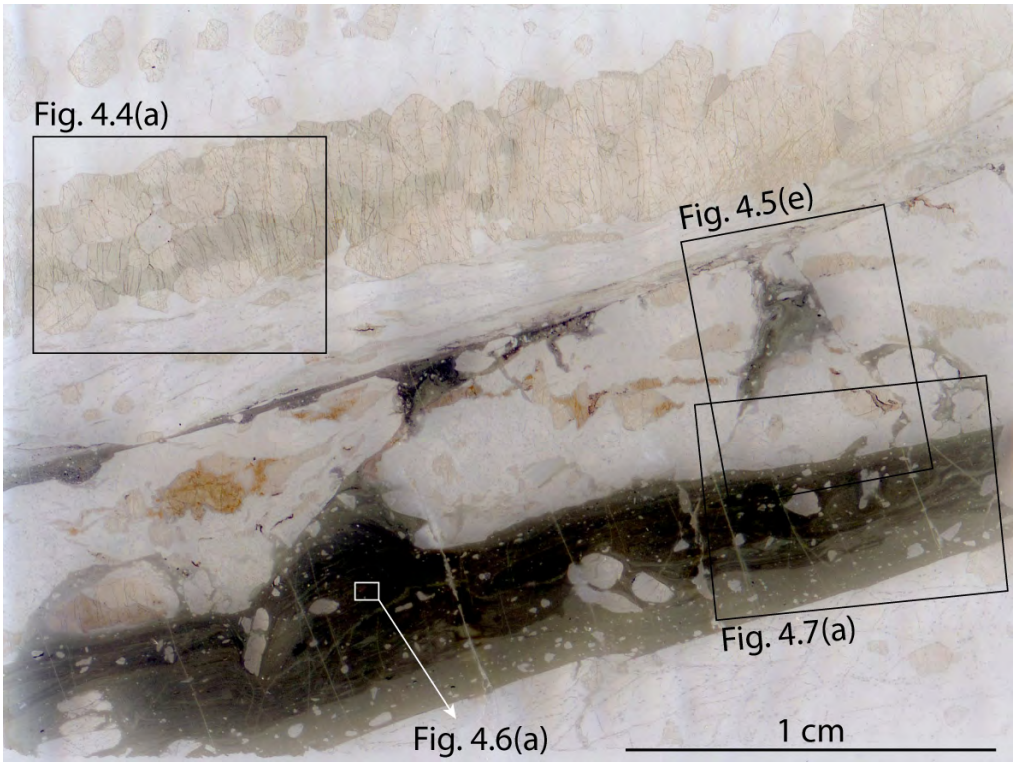

(a) HK2: Paired slip surfaces of pst (generation zone fault-geometry) connected by pst veins and fractures. Lenticular fragments of variably damaged wall-rock is encapsulated in between. A grt-px band is oriented subparallel to the fault plane.

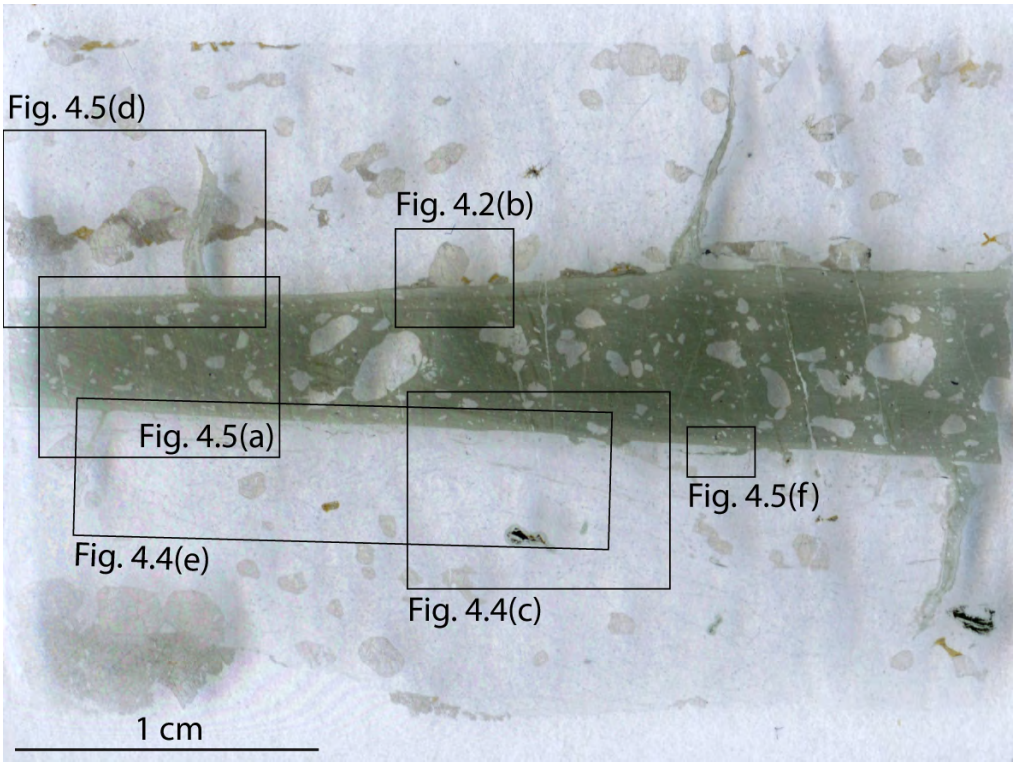

(b) HK4: A single fault vein with near-orthogonal injection veins.

Figure 4.3: *Scanned thin sections from fault HK at the Hundkjeften locality.*

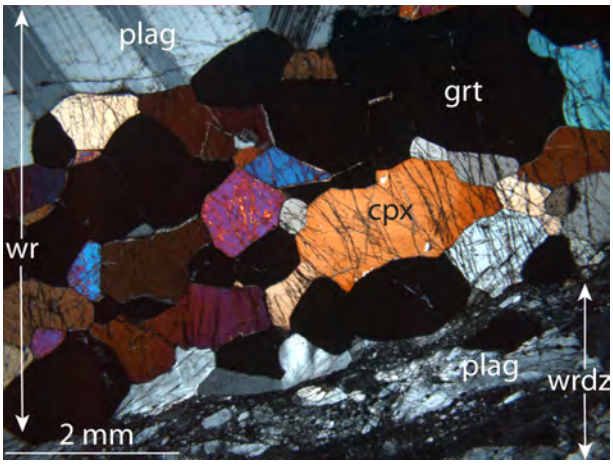

(a) Grt-px band in wall-rock. In upper left the plag is well-preserved, while in lower right it is fractured and crushed in the wall-rock damage zone. See Fig.4.3 for relation to fault plane (HK2, xpl).

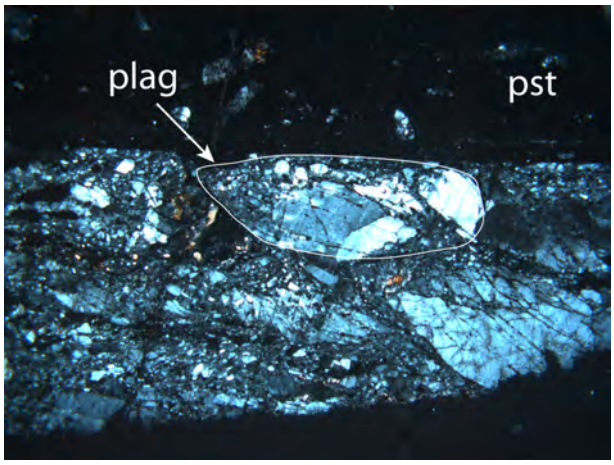

(b) The former outline of a fractured plag grain is sketched. The grain is bent, and goes extinct, from left to right, as the stage is turned (HK6, xpl).

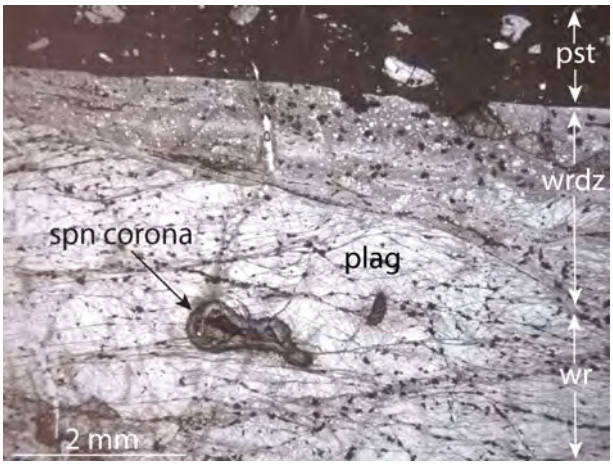

(c) Wall-rock and wall-rock outside pst. Spl corona seen in wall-rock, and fractured plag observed in wall-rock damage zone in middle right. Note symplectites on fractures (HK4, ppl).

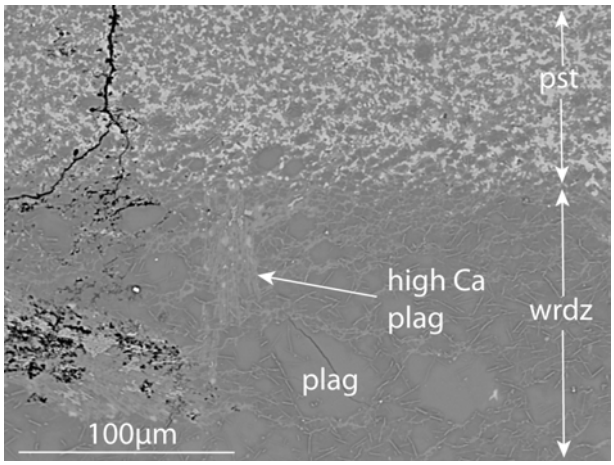

(d) Angular to subrounded fragments of plagioclase in wall-rock damage zone. Note the change in grain size from wall-rock damage zone to pst (HK4, BSE).

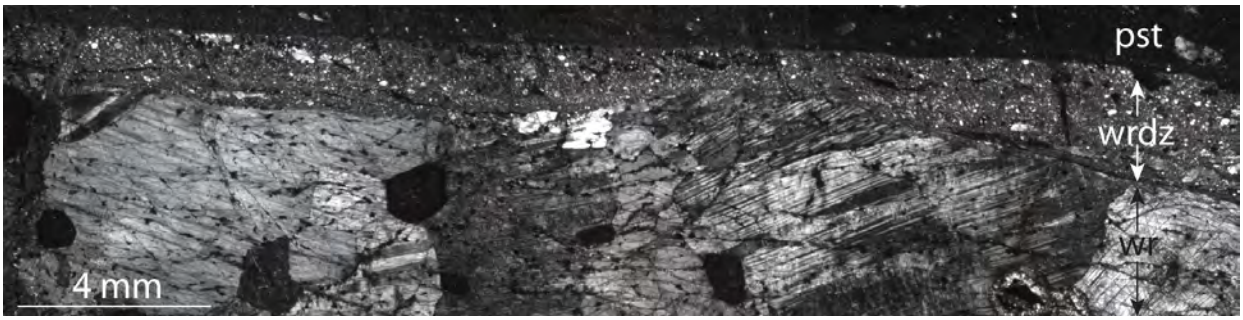

(e) Photomerged micrographs of the lower part of the pst in HK4, the fine grained wall-rock damage zone and the fractured plag in the wall-rock related to it. Note the variable thickness of the wall-rock damage zone. (HK4, xpl).

Figure 4.4: *Micrographs (a-c, e) and BSE-image (d) illustrating the textures and apperance of the wall-rock damage zone of fault HK at Hundkjeften.*

The matrix of the pst consists of plagioclase, amphibole and K-feldspar, the different minerals pointed out in Fig. 4.6a. The darkest grayshade in this BSE-image is plagioclase, the intermediate is K-feldspar, and the palest is amphibole. The grain size is ∼5-10 μm. The thin needles in the matrix, *i.a.*, also observed on plagioclase clasts, may exceed this in their longest direction. Although relatively long, they are so thin that clean analyses in the EMP is difficult to obtain. This phase is therefore not determined, but observations in the optical microscope suggests zoisite.

Like illustrated in Fig. 4.6a, 4.6c and 4.6d, the orientation of the grains in the matrix typically show a random orientation with respect to each other, and to the orientation of the pst vein. Nevertheless, a few places the plagioclase grains show a shape-preferred orientation of elongated, aligned grains. Fig. 4.6c is an example of this, with plagioclase aligned subhorizontal in the image. No correlation was observed considering the distance to the margin or the center of the vein and the places this fabric was observed.

The clasts reflects the local mineralogy of the wall-rock; most are of plagioclase, but clinopyroxene and garnet is also observed. The clasts in the pst have highly variable sizes and shapes. Like displayed in the micrographs in Fig. 4.5a, 4.5c and 4.7, the clasts are up to 1 mm in diameter. The shape of the clasts range from angular to subrounded, or what is often referred to as thermally rounded clasts. This holds also for the smaller clasts, as observed in BSE-images in Fig 4.6. Clasts of plagioclase measuring 20-100 μm across are subangular to subrounded, while the clinopyroxene clast in Fig. 4.6d has the shape of a triangle with a rim of amphibole around. This suggest no obvious relation between the size and shape of the clasts in the pst.

When investigated in crossed polarized light (xpl), see Fig.4.7b, the smallest plagioclase clast has nearly intact twinning lammelae, while the larger clast is fractured and appear more damaged. Also a core-mantle structure is observed, where the outermost part of the clasts have a very fine grain size, whereas the center of the clast retain as a part of the original mineral grain. A fracture in the largest clast is filled with grains of a small grain size, like in the mantle. Symplectites are observed in the remains of the plagioclase crystal.

Kyanite is found as aggregates of needles in association with amphibole, see Fig. 4.6d, in an injection vein.

Garnet is observed both as fragments derived from an earlier, larger wall-rock garnet, and as crystals grown from the melt. The fragments of old garnet (Garnet1), have a rim of newly grown garnet (Garnet2). An example of garnet probably grown from the pst melt is displayed in Fig. 4.6c. The garnets have highly irregular contours, and no crystal faces properly developed. The garnets are ∼50 μm in diameter.

In Section 4.4, the results of image analyses on clasts from micrograph HK4 is presented.

4.2 Husebøvatnet

4.2.1 The Pristine Mineralogy of the Wall-Rock

The pristine mineralogy of the wall-rock of the Husebøvatnet locality is similar to the wall-rock at Hundkjeften, described in 4.1. However, the modal composition is different, with larger amounts og pyroxene and garnet at Husebøvatnet on expence of plagioclase. Non of the samples drilled at Husebøvatnet were drilled more than a cm away from the fault planes.

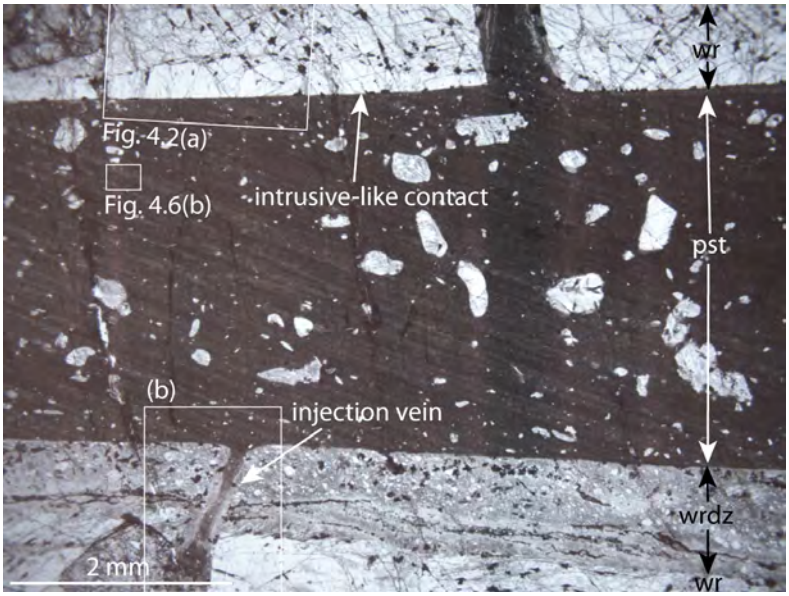

(a) *Fault vein with a sharp contact to the wall-rock above and a wall-rock damage zone below. Injection veins intrudes both wall-rock above (close-up in Fig. 4.5d) and wall-rock damage zone and wall-rock below (close-up in Fig. 4.5b) at high angles. Plag clasts of variable size and shape is observed in pst. Striations in pst is due to sample preparation (HK4, ppl).*

(b) *Close-up on the injection vein truncating wall-rock damage zone and wall-rock. Notice the abrupt changes in grain size from pst to wall-rock. (HK4, ppl).*

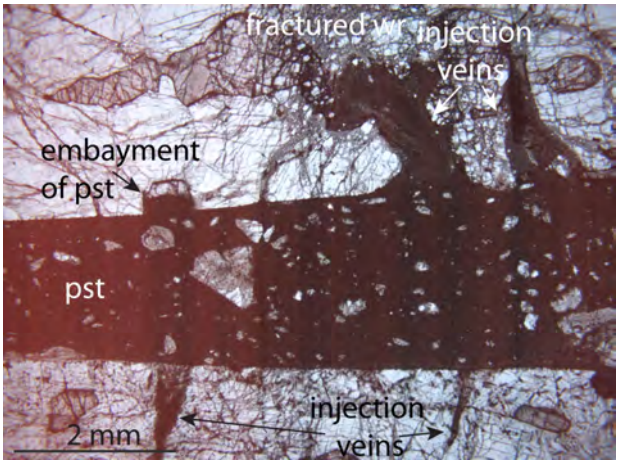

(c) *Fault vein with sharp contacts to the wall-rock, and injection veins of different geometries. The wall-rock seems highly affected by the injections in upper right in the image. An embayment is seen where a grt is in direct contact with the pst. Clasts of highly variable size and shapes are observed (HK12, ppl).*

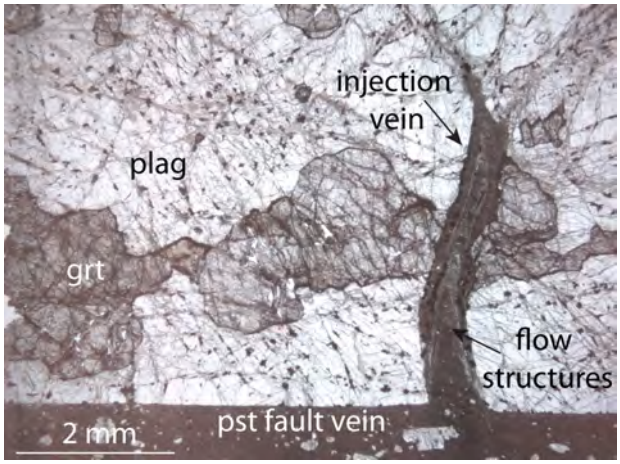

(d) *A clean fracture-type injection vein with flow structures. Garnets crystals, probably grown from the melt, is seen as black dots in injection vein. Notice symplectites on fractures in plag in wall-rock (HK4, ppl).*

Figure 4.5

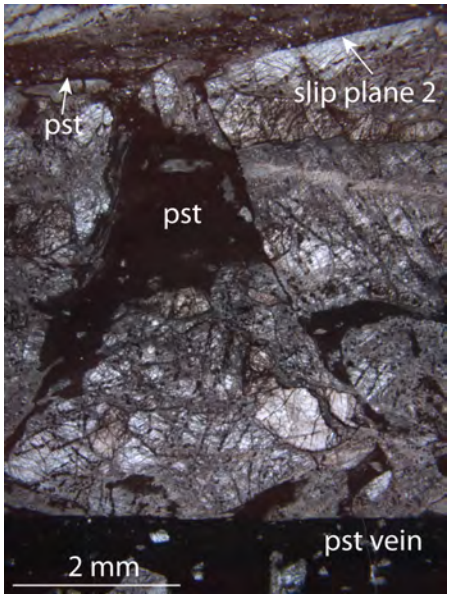

(e) Network of higly irregular pst veins interconnecting two paired slip planes, see Fig. 4.3a for location of image. The amount of pst on the slip planes differ greatly between the upper and lower plane in the image. Note fractured wall-rock in between (HK2, ppl).

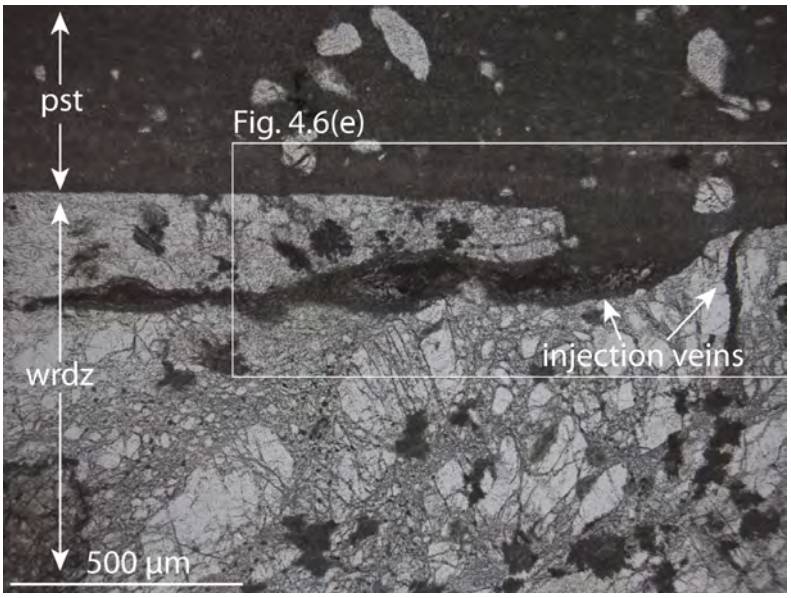

(f) Injection veins into wrdz, one fault vein parallel and one orthogonal. The fault vein parallel has alternating thicker and thinner units. Fragments of fractured plag grains of $\leq 500\mu m$ is observed in the wall-rock damage zone outside pst (HK4, ppl).

Figure 4.5: *Micrographs illustrating the geometry of the pseudotachylyte (pst) veins of fault HK at Hundkjeften.*

4.2.2 The Wall-Rock adjacent to Fault Zones

Minerals observed in the wall-rock adjacent to the fault zones at Husebøvatnet can be divided into three mineral assemblages; the Precambrian granulite facies mineral assemblage, and the Caledonian eclogite and amphibolite facies mineral assemblages.

1. The granulite facies paragenesis is plagioclase+garnet+clinopyroxene+orthopyroxene +spinel±amphibole.

2. The eclogite facies paragenesis is omphacite+garnet2+kyanite+k-feltspar+zoisite

3. The amphibolite facies paragenesis is biotite+corundum+K-feldspar+zoisite±rutile ±Fe-Ti-oxide±muscovite±chlorite

The appearance of the minerals and the texture of the wall-rock at Husebøvatnet resembles the observations of the thin sections from Hundkjeften, see Section 4.1. Although, some differences are noticed, and will be presented here.

The wall-rock adjacent to fault zones at Husebøvatnet is observed varying from almost pristine, via highly fractured and partly recrystallized, to nearly totally recrystallized and replaced, see Fig.4.8 and Fig.4.9. Fig.4.8a display highly fractured wall-rock of fault HVa. The plagioclase in the lower part of the image does not show any particular signs of recrystallization, but zoisite and K-feldspar is observed as feathery intergrowths on grain boundaries and along fractures. The fractures in the plagioclase truncates the garnets without any change in either direction or number. The fractures are oriented subparallel to the fault plane, that is sub horizontal in the image.

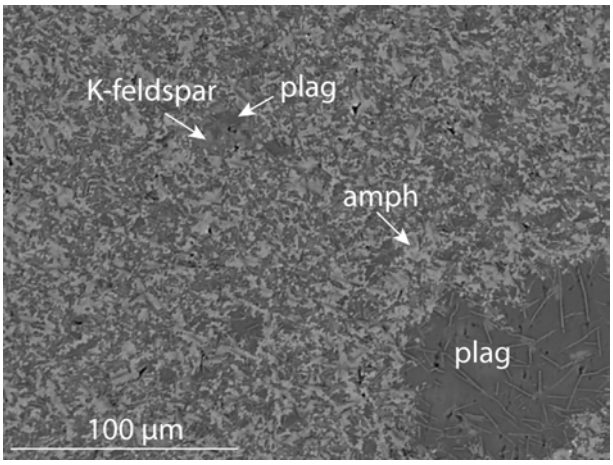

(a) *Randomly oriented minerals in pst matrix. Clasts of plag as survivor grains from wall-rock (HK2).*

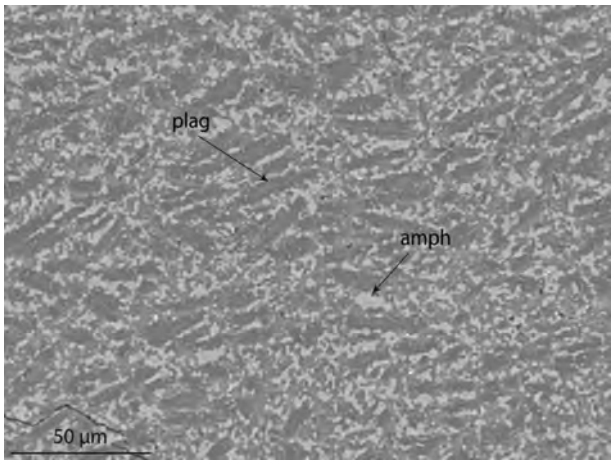

(b) *Shape-preferred orientation of plag making a fabric in the pst matrix. Crystals aligned subhorizontal in image, i.e. subparallel to the strike of fault vein (HK4).*

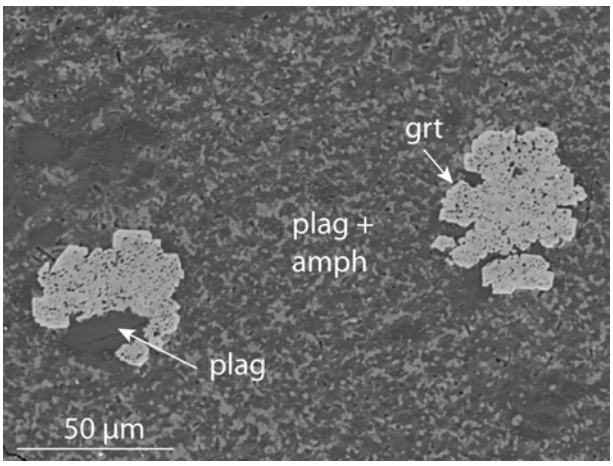

(c) *Randomly oriented minerals in pst matrix, with grain sizes below 10 µm. Grt showing hopper-type crystal growth (HK4).*

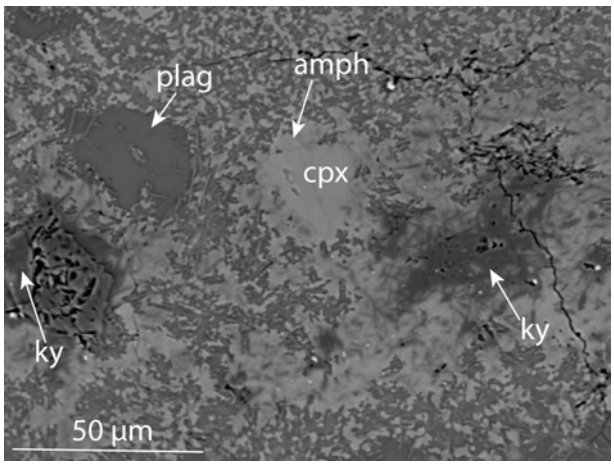

(d) *Clasts of minerals in pst injection vein; plag, cpx with amph around, and an aggregate of ky and amph (HK4).*

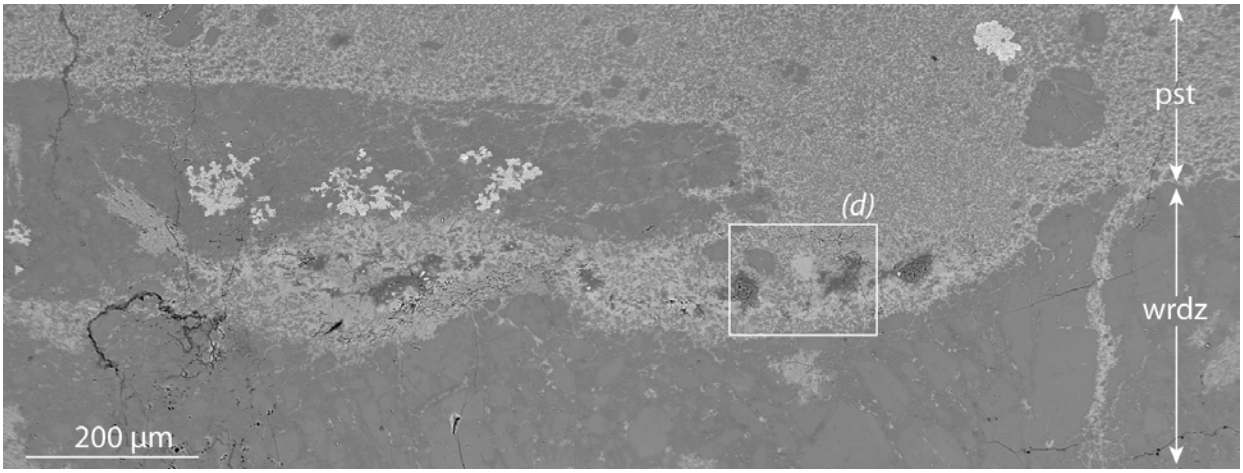

(e) *Fault vein-parallel injection vein into wall-rock damage zone. Note also one thin, orthogonal injection vein (to the right in image). The wall-rock zone consist of angular to subangular fragments embedded in a darker gray matrix (HK4).*

Figure 4.6: *BSE-images of the texture, clasts and newly grown crystals in pseudotachylyte (pst) from fault HK at the Hundkjeften locality. This fault has an amphibolite facies mineralogy (amph+K-feldspar in matrix).*

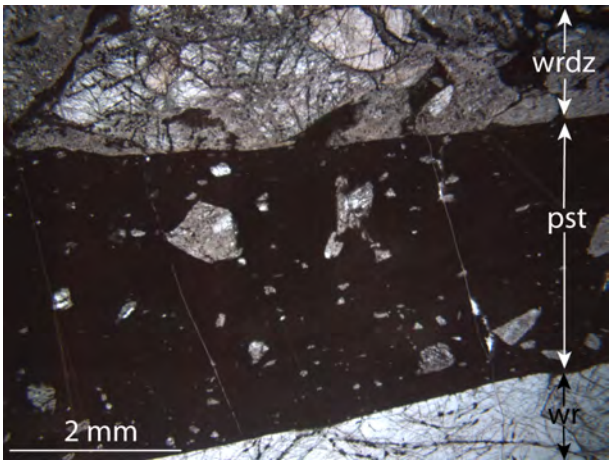

(a) Clasts in pst fault vein. Notice the range in size and the varying degree of roundness of the clasts, and the irregularity of the injection veins into wrdz (HK2, ppl).

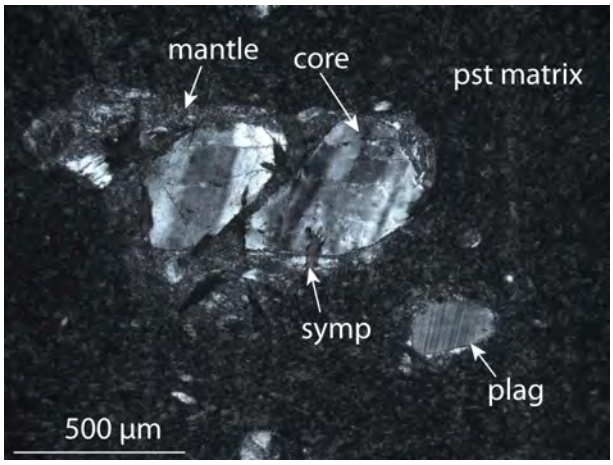

(b) Clasts of plag in pst fault vein. The remnants are surrounded by a rim of recrystallized material, like a core-mantle structure (HK4, xpl).

Figure 4.7: *Micrographs of clasts in pst fault HK at Hundkjeften locality.*

Fig.4.8c and Fig. 4.8e show an increase in alteration and hydration of the wall rock. Fig.4.8c show plagioclase largely recrystallized to zoisite crystals. The BSE-image in Fig .4.8b show a close-up of zoisite in plagioclase. As seen in Fig. 4.8d the twins in the plagioclase are no longer visible, the only remains seen in middle left of the image. In Fig.4.8d a reaction rim is observed around garnet. The orientation of fractures in these images is random, compared to what observed in Fig. 4.8a.

In Fig.4.8e a double reaction rim is observed around the garnets. A close-up on one garnet in Fig. 4.8f show a black rim between the two reaction rims, interpreted as the former outline of the garnet. The inner reaction rim consist of white mica and chlorite, and has an undulating border to the garnet crystal. The outer reaction rim consists of chlorite.

Fig. 4.9 show how clinopyroxene in wall-rock adjacent to faults is deformed, altered and hydrated. In Fig. 4.9a the clinopyroxene crystal is fractured and bent, the latter indicated by exsolution lammelae bending clockwise in center of micrograph. The amphibolite and eclogite facies minerals zoisite+kyanite+K-feldspar+garnet+omphacite is detected by EDS in the transition between clinopyroxene and recrystallized plagioclase. In Fig 4.9b clinopyroxene with exsolution of garnet is shown. The clinopyroxene is fractured, and the bright spots are Fe-sulphides. This part of the sample is from one of the garnet-pyroxene bands in the wall-rock of Husebøvatnet. Plagioclase partly covered by zoisite needles and K-feldspar is also observed in this image.

The variable degrees of hydration and alteration of the wall-rock as shown in Fig 4.8 and 4.9 is observed in association with all the three studied faults at Husebøvatnet locality. Almost pristine and recrystallized wall rock is observed close to each other, *e.g.*, on opposite sides of a pst vein. The wrdz and pst associated with each of the faults HVa, HVb and HVc will be described in the following section.

4.2.3 The Wall-Rock Damage Zones and the Pseudotachylytes

Fault HVa

The wall-rock of fault HVa range from nearly pristine with symplectites of K-feltspar+zoisite, to extensively hydrated and altered (Fig. 4.8). Fig. 4.10a show highly fractured wall-rock, and in the upper part of Fig. 4.8a several narrow cataclastic zones truncates the plagioclase and garnet in the

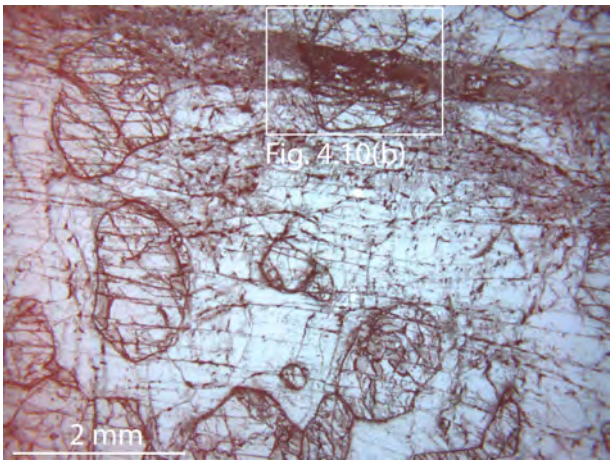

(a) *Highly fractured wall-rock of fault HVa, with cataclastic zones in upper part of image. Most fractures oriented subparallel to fault zone (HV4, ppl).*

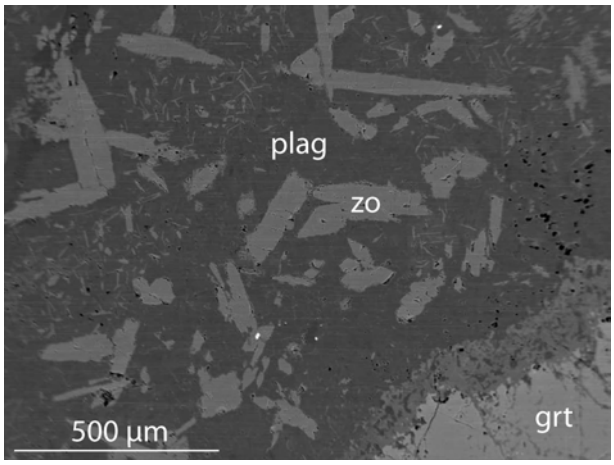

(b) *Zo needles in plag in partly hydrated wall-rock of fault HVb. Garnet surrounded by one single reaction rim in lower rigth corner(HV7, BSE-image).*

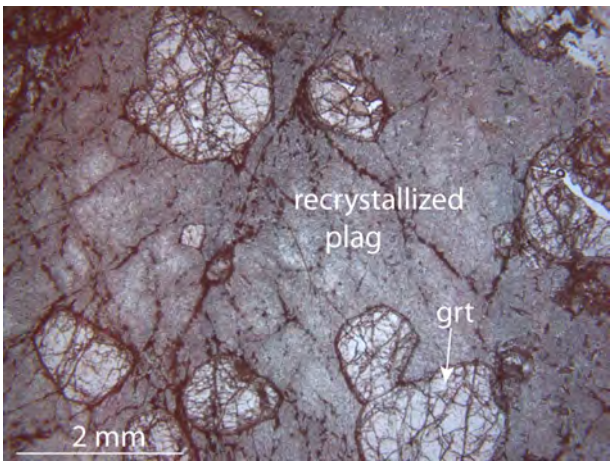

(c) *Partly hydrated wall-rock of fault HVc with recrystallized plag. Garnets intensely fractured (HV11, ppl).*

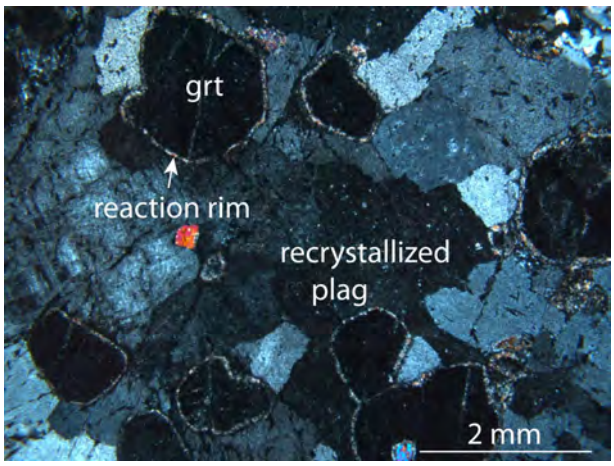

(d) *Partly hydrated wr of fault HVc with recrystallized plag.Garnets surrounded by one single reaction rim (HV11, xpl).*

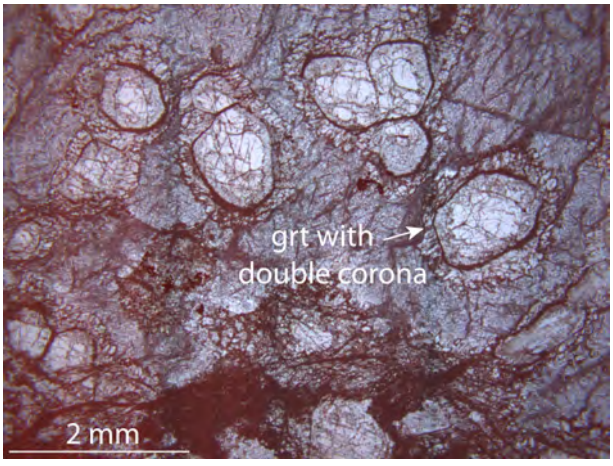

(e) *More hydrated wall-rock of fault HVa, with recrystallized plag and double reaction rims around garnet (HV2, ppl).*

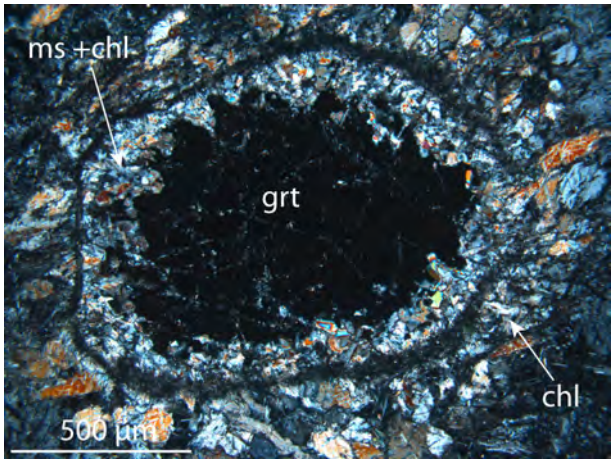

(f) *Grt with double reaction rim, separated by a black rim interpreted as the former outline of the garnet. The innermost consists of ms+chl and the outermost of chl (HV2, xpl).*

Figure 4.8: *Micrographs (a, c-f) and BSE-image (b) of the variably hydrated wall-rock at Husebøvatnet locality, focusing on plag and grt.*

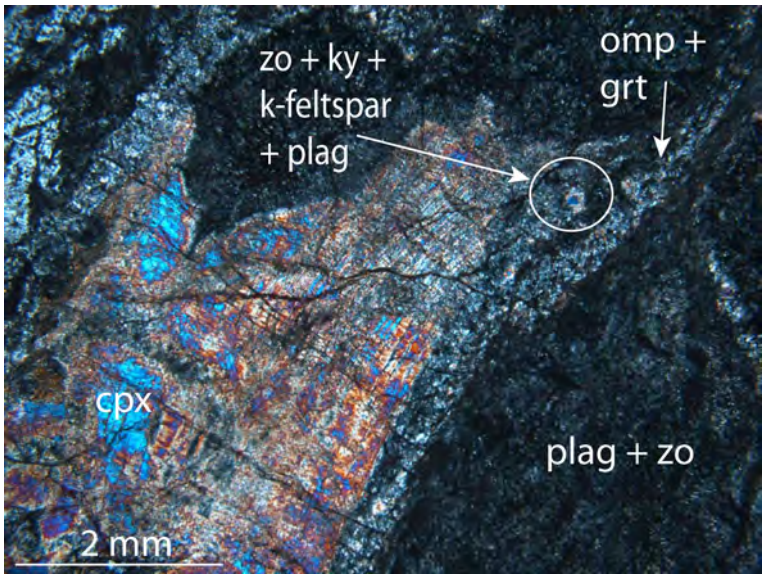

(a) *Parts of a fractured cpx crystal in hydrated wall-rock of HVc. Exsolution lammelae reveal the crystal is bent (HV11, xpl).*

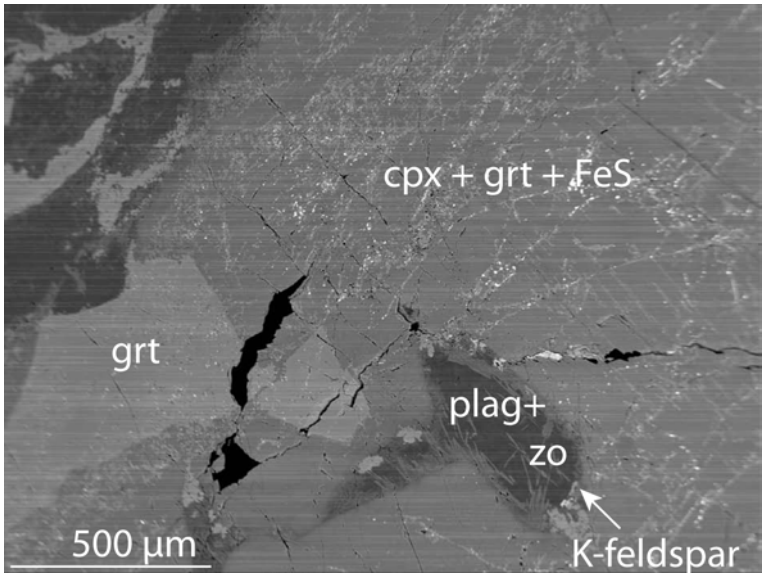

(b) *Exsolution of grt in cpx in wall-rock of fault HVb. This image show parts of a px-band cut by fault rock, see Fig. 4.11b for location of image. Note the presence of Fe-sulphides (bright, white dots)(HV7, BSE-image).*

Figure 4.9: *Micrograph(a) and BSE-image(b) of deformed and altered cpx in the wall-rock at Husebøvatnet locality.*

wall-rock. A close-up on one of this cataclastic zones is shown in Fig. 4.10b, where it runs from upper left to lower right. The width of this cataclastic zone is ∼600-700 μm.

In contrast to the sharp boundaries between wall-rock/wrdz and pst at fault HK at Hundkjeften, undulating boundaries between wall-rock/wrdz and pst is more common along fault HVa. This feature is displayed in Fig. 4.10a and 4.10c. The wrdz consist of fine grained material with grain sizes of $15 - 30\mu m$, see Fig. 4.10d. Larger fragments of plagioclase is also present, like in the center of Fig. 4.10a. The shape of the grains in the wall-rock damage zone is angular to rounded, see also Fig. 4.10d. The thickness of the wrdz is typically ∼300-700 μm wide.

The vein geometry of pst at fault HVa is one single, unduating fault vein. Clean-fracture type injection veins are not observed, but injections of irregular shapes into the wall-rock are found, *e.g.*, in the upper left corner of Fig. 4.10a. The melt has intruded the fractured wall-rock and migrated along grain boundaries and fractures, and the result is a network of thin pst-veins in the wall-rock.

The matrix of the pst consist of plagioclase, amphibole and kyanite. Fault HVa hence has an amphibolite facies mineralogy. The grain size is $\leq$10 μm. Fig. 4.10d display the texture of the pst, which is random orientation of anhedral plagioclase and amphibole, and euhedral kyanite needles. Although not investigated in the EMP, Fig. 4.10c display flow structures in the pst, indicated by the white streaks.

The clasts The number of clasts in the pst is very low compared to the number of newly grown crystals (microliths). Fe-sulphides of dendrittic morphologies is observed, although the main phase of newly formed crystals is garnet. As pointed out in Fig. 4.10c, garnets are aligned along the margin of the pst. The garnet crystals follow the curvature of the pst vein. The BSE-image in Fig. 4.10d also show garnets aligned on the margin of the pst. The garnets have a high number of inclusions in the core, which maybe could explain their appearance in ppl, Fig. 4.10c, with darker rims and more pale cores.

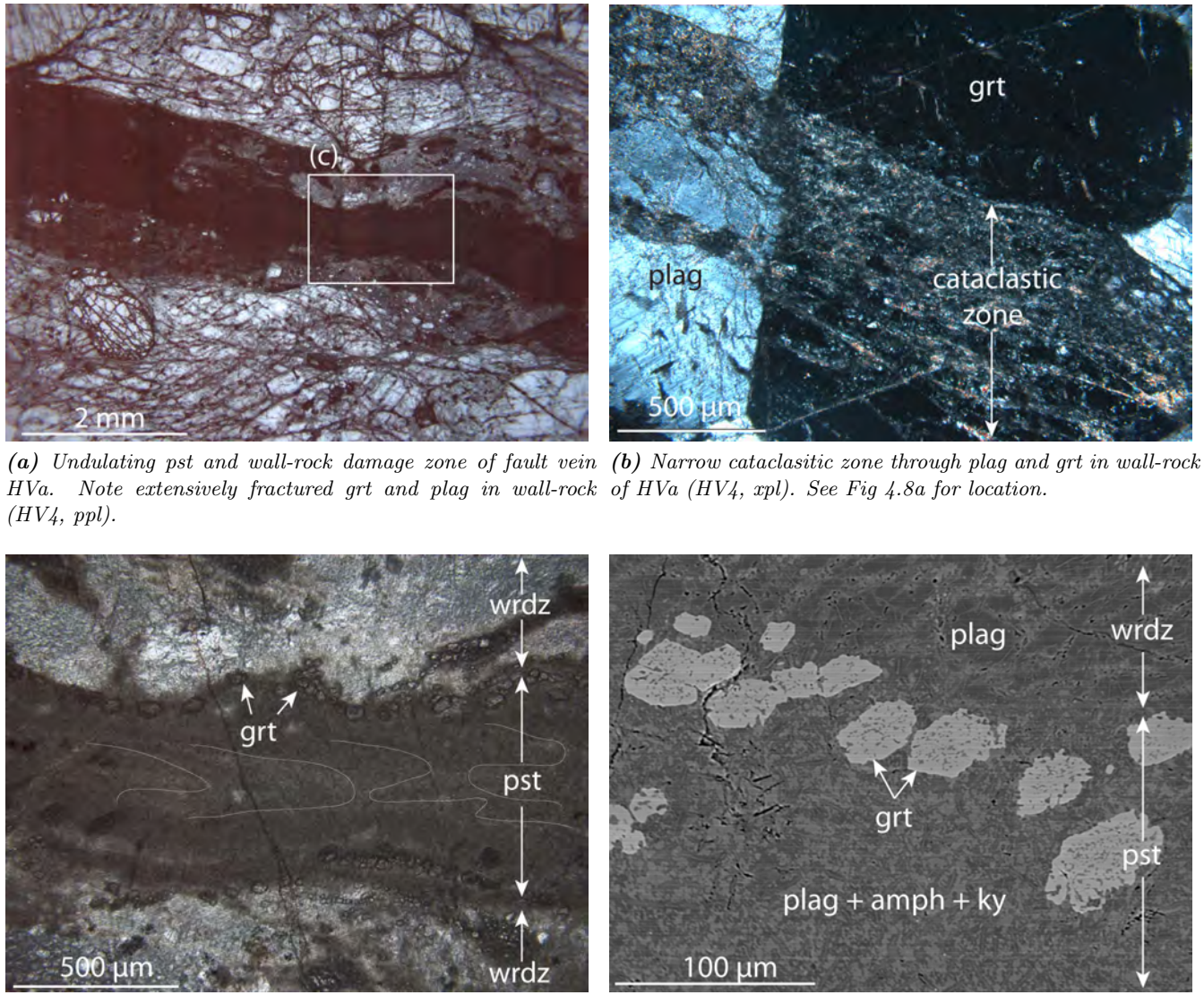

(a) *Undulating pst and wall-rock damage zone of fault vein HVa. Note extensively fractured grt and plag in wall-rock (HV4, ppl).*

(b) *Narrow cataclasitic zone through plag and grt in wall-rock of HVa (HV4, xpl). See Fig 4.8a for location.*

(c) *Grt aligned on the transition between wall-rock damage zone and pst of fault HVa. Flow structures in pst is highlighted in white (HV4, ppl).*

(d) *Grt aligned on the transition between pst and wall-rock damage zone of fault HVa. Matrix minerals in pst are plag+amph+ky. (HV4, BSE-image).*

Figure 4.10: *Micrographs (a-c) and BSE-image (d) of wall-rock damage zone and pst of fault HVa at Husebøvatnet locality.*

Fault HVb

The wall rock of fault HVb is either nearly pristine, like in lower right of Fig. 4.12c, with only symplectites of K-feltspar+zoisite on grain boundaries, or the wall-rock is partly hydrated, and the plagioclase is altered to zoisite, like in Fig. 4.12b. It also varies greatly considering the amount of fracturing.

The contact between wall-rock and pst is in most places sharp, like the lower boundary of the pst in Fig. 4.12c, even more visible in the BSE-image in Fig. 4.13b. Here, the wall-rock is to a limited extent fractured, and otherwise looks undisturbed, with few inclusions. In Fig. 4.12a garnets in the center of the image are cut straight off by a pst vein. Other places, like in Fig. 4.13a and upper parts of Fig. 4.13b, there is a wrdz in between the wall-rock and the pst.

The wrdz outside the pst consist of fine grained material with grain size 15-50 μm. Wrdz is also observed in between interconnected pst veins, like in Fig. 4.12b, where the wrdz consists of highly fractured wall-rock, and fractured and recrystallized plagioclase, in addition to fine-grained crushed material. The thickness of the wrdz is $\leq$3 mm.

Corona structures with corundum in the core are observed in the wrdz, see Fig. 4.13a. The rims in the corona consist of garnet+amphibole, the garnet rim thicker than the amphibole rim.

The vein geometry of the pst of fault HVb varies along strike. Parts of pst has the shape of a singel fault vein. The borders to the wall-rock and/or wrdz are straight. The pst also show a pst generation zone-geometry; a paired slip zone, with varible amounts of pst on the slip planes, like in thin section HV5 in Fig. 4.11a. The micrograps in Fig. 4.12a show two subparallel pst veins of variable thickness, ranging from $\sim$200 μm - 2 mm. The two planes of slip joins to one fault vein in Fig. 4.12b. In between the two planes injection veins of highly irregular geometries are observed intruding the wrdz and connecting the two planes. Fig. 4.12e display narrow zones of deformation subparallel to the fault vein (subhorizontal) in the image. Some of the zones contain pst that enclose lenticular fragments of wall-rock.

The pst on fault HVb can be divided into two types, Type 1 and Type 2, on the basis of color and textures visible in ppl.

Type 1 pst has a dark brown-black color in thin section, also in ppl. Two different mineral assemblages is observed; omphacite+kyanite where it is not closely associated with Type 2 pst, like in Fig. 4.13d. Closely relatede to Type 2, matrix minerals are plagioclase+garnet+biotite, as shown in Fig. 4.13b. The plagioclase and the garnet is anhedral, the biotite is euhedral to subhedral. The grain size is $\leq$10 μm, except the kyanite needels, that can be longer. The orientation of the mineral grains appear random in the BSE-image in Fig4.13d.

Type 1 pst have clasts of different sizes and shapes. Plagioclase clasts are observed in the range of $\sim$30 μm - 1,5 mm, see Fig. 4.13b and 4.13d. The large plagioclase clast in Fig. 4.13d have domains of two different gray shades, and also symplectites/feathery intergrowth of K-feldspar and zoisite associated with a central fracture, see Fig. 4.12b. In the same image a 1.5 mm long garnet clast is also observed. It has a high number of inclusions, and a rim of garnet that has probably grown from the melt, and therefore show this uneven suface. The clasts are thermally rounded.

Newly grown crystals are garnets, as illustrated in Fig. 4.13a and 4.13c. Garnet crystals are aligned like on a string along the margin of the pst, but are also found in the more central parts of the pst veins. The garnets are $\leq$ 200 μm in diameter, and the typical size is $\sim$50 μm. Garnet is also observed as a $\sim$50-100 μm thick rim around a rutile clast.

Type 2 pst has a pale gray color in thin section, also in ppl, see center of Fig 4.11b. It consist of alternating white and dark bands, see Fig. 4.12d-4.12f. Flow structures are observed in the optical microscope in ppl, like in Fig. 4.12c - 4.12f and in Fig. 4.11b. Sheet folds in Fig. 4.12d are visible and

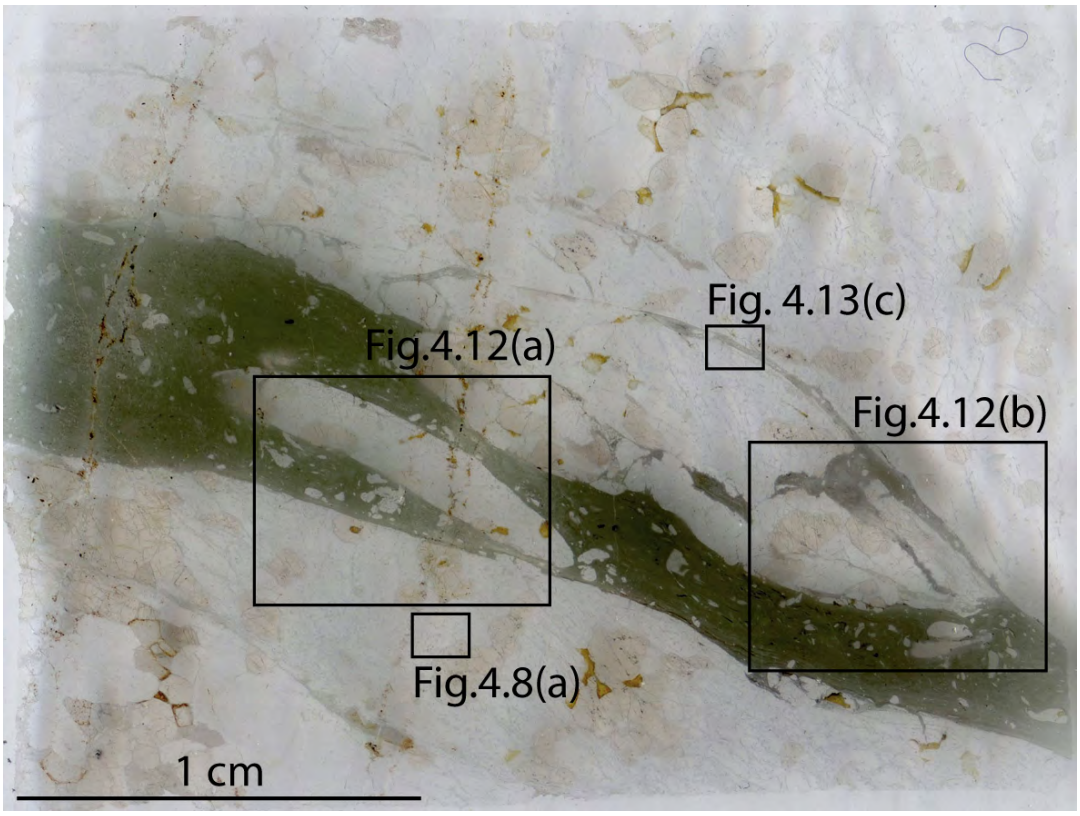

(a) HV5: Image of scanned thin section with location of detaile figures.

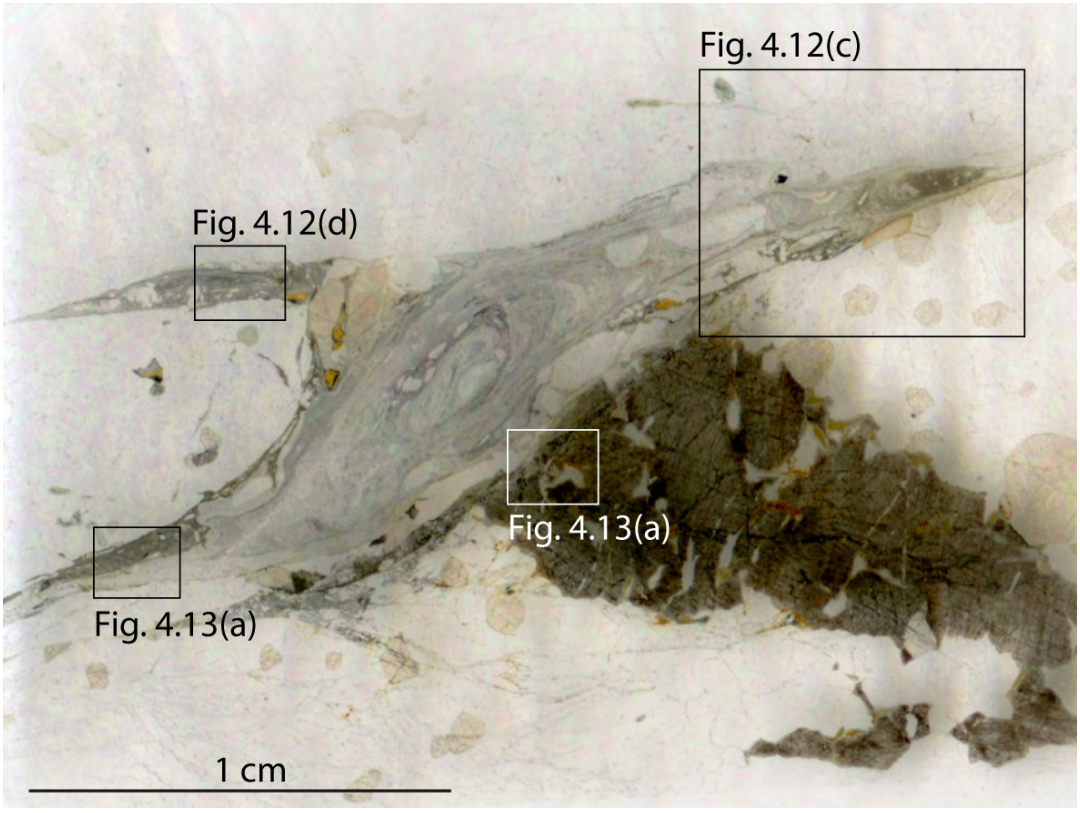

(b) HV7: Image of scanned thin section with location of detail figures.

Figure 4.11: *Scanned thin sections from fault HVb at Husebøvatnet locality.*

defined by alternating dark and pale bands. The foliation is wrapped around clasts, see Fig. 4.12e and 4.12f. The border to the wall-rock/wrdz is sharp, see Fig. 4.12d and 4.13b. This boundary may be difficult to see in micrographs, due to an extensive overgrowth/alteration of the rock, including the pst, erasing or hiding the sharp boundary some places, like in the upper part of Fig. 4.12c.

Type 2 has clasts of plagioclase, see Fig 4.12d-4.12f. In Fig 4.12d both angular and rounded clasts are observed, and their orientations appear random with respect to the orientation of the fault vein. The clasts are ∼75-100 μm in the longest direction. The clasts in Fig. 4.12e and 4.12f(close-up) are larger, up to ∼600 μm, and elongated parallel to the strike of the fault vein. They are subrounded to rounded. The foliation in the fault vein is wrapped around the clast, that has the shape of a ϕ clast. The white bands in the matrix are probably elongated crystals of plagioclase. Symplectites are observed in the larger clasts. Type 2 pst thus show typical characteristics of both pst and mylonite. This will be discussed in Chapter 7.

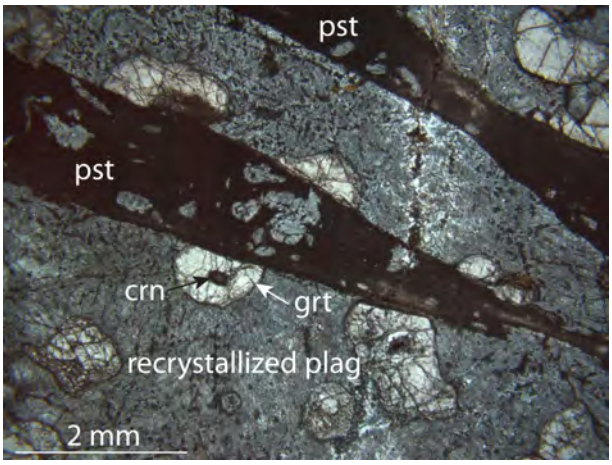

(a) Grt cut sharply off by pst of fault HVb. The plag in the wall-rock is recrystallized (HV5, ppl).

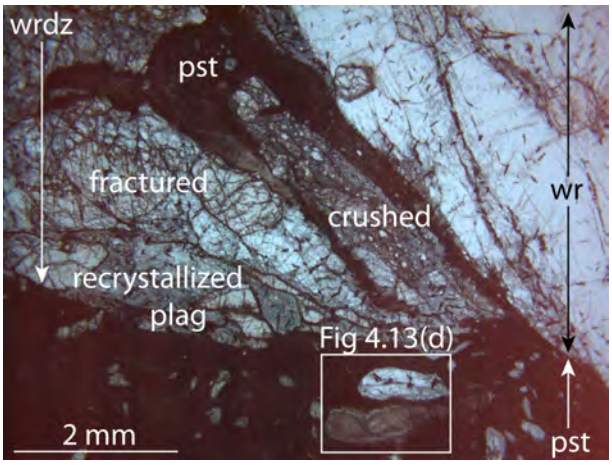

(b) Interconnected veins of pst of HVb. Wall-rock damage zone between comprise crushed material, recrystallized plag, and larger fragments of fractured plag (HV5, ppl).

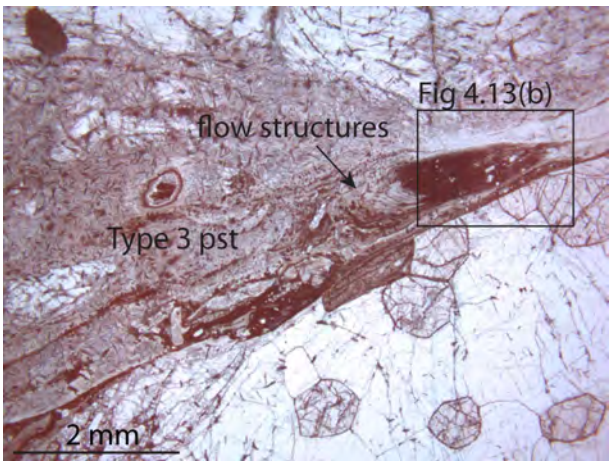

(c) Pst type 2 with one sharp contact to the wr. Above is recrystallised wall-rock damage zone. A pocket of type 1 pst (dark) is observed inside the rectangle (HV7, ppl).

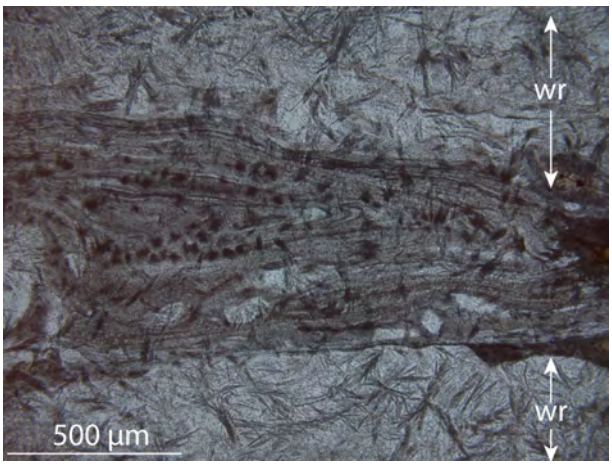

(d) Flow structure/sheet fold in type 2 pst (HV7, ppl).

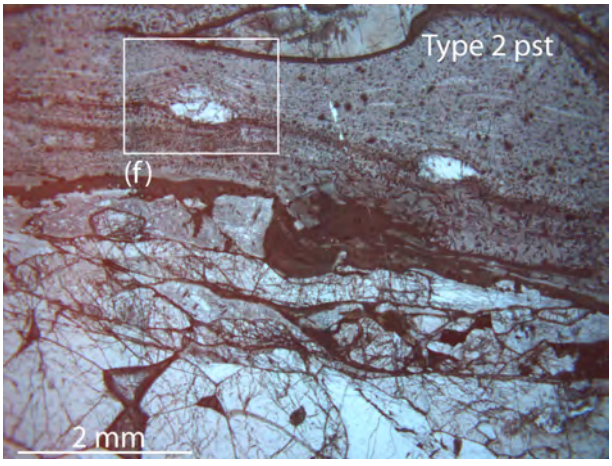

(e) Plag clasts in type 2 pst. Notice thin veins of dark material parallel to the fault vein, in the lower part of the image (HV6,ppl).

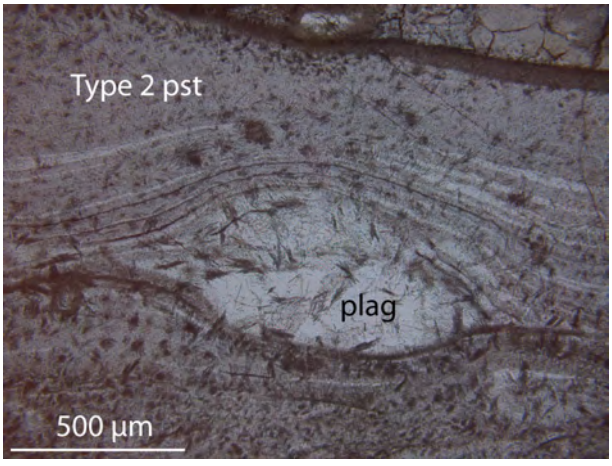

(f) Alternating dark and white layers deflected around plag ϕ clast in type 2 pst (HV6, ppl).

Figure 4.12: *Micrographs of wall-rock, wall-rock damage zone and fault rocks of fault HVb at Husebøvatnet locality. Note the variable apperance of the pst along strike; Type 1 (a,b,(c)) and type 2 (c-f).*

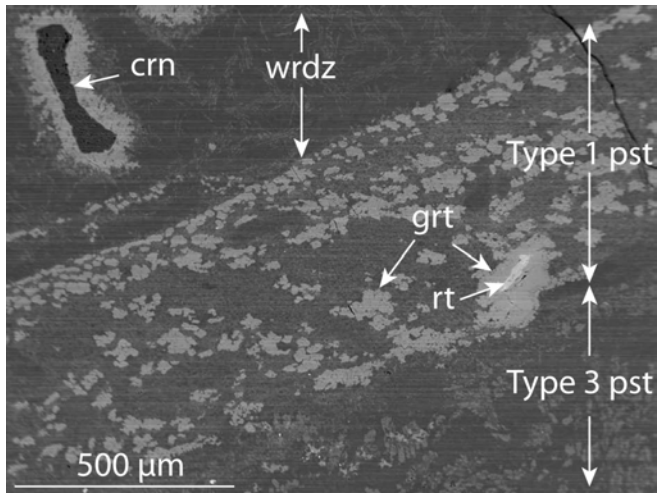

(a) *Wall-rock damage zone and pst of fault HVb. Notice coronas with core of crn and rt, and garnet newly grown from melt (HV7, BSE).*

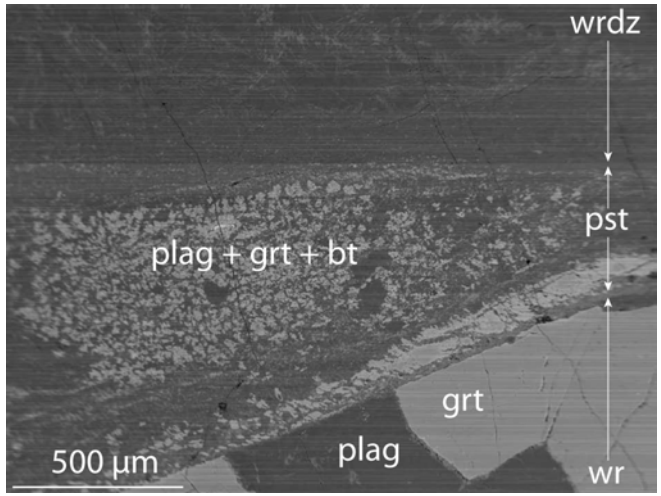

(b) *Pst with a wall-rock damage zone outside upper contact, and a sharp, intrusive contact to the wr below. Notice the relatively undisturbed grt of the wall-rock (HV7, BSE).*

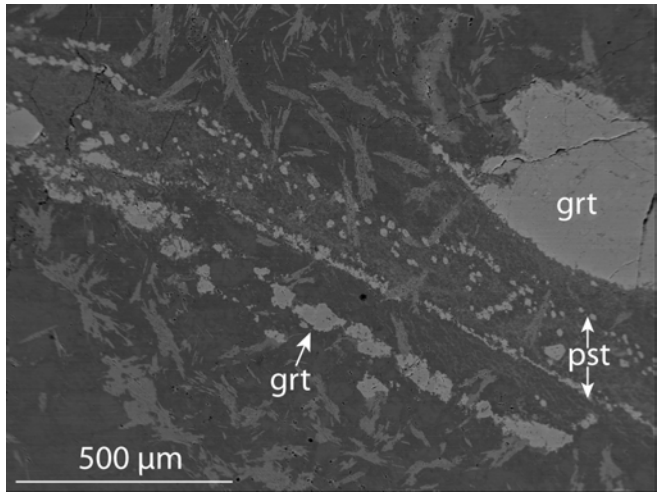

(c) *Thin pst vein in wall-rock away from the main fault plane. Garnet aligned parallel to the vein, near the margins (HV5,BSE)*

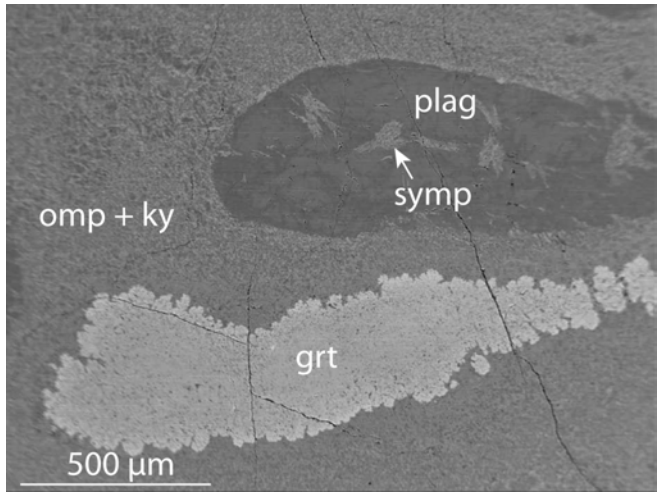

(d) *Clasts of plag and grt in pst vein of fault HVb. The grt clast has a rim of newly grown grt (HV5, BSE).*

Figure 4.13: *BSE-images from fault HVb at Husebøvatnet locality. All images are from Type 1 pst.*

Fault HVc

The wall rock of HVc is hydrated and partly altered, like the wall-rock in Fig. 4.8c and 4.8d. Plag is saussuritized with growth of zoisite, and garnets have a single reaction rim. Clinopyroxene is variably deformed and altered, and show undulose extinction, as observed in Fig. 4.14b. The wrdz consist of cataclastic material and highly fractured, partly recrystallized, wall-rock. Where the wrdz is present, the observed thickness is $\leq$ mm.

Coronas of spinel are observed in the wrdz, along the border to the pst. The spinel in the core is rich in alumina (detected by EDS). The rims consist of corundum±biotite+garnet±Fe-Ni-sulphide.

The vein geometry The pst of HVc is a singel fault vein of variable thickness and straight margins. Nearly orthogonal injection veins ramify of the fault vein, and extend ∼3 mm into the wall-rock, see Fig. 4.14b. The same figure show that several narrow deformation zones of pst and/or cataclasite truncate the wrdz. These thin zones are oriented subparallel to the fault vein, and possibly connected to it, or to a cataclasite adjacent to the pst.

The matrix The mineral assemblage of the matrix is amphibole+omphacite+kyanite. Amphibole and omphacite crystals are anhedral. The grain size is $\sim 5-35\mu m$, but is typically ∼15 μ m. Kyanite is observed as asicular grains/needles of $\leq$20 μm in the longest direction, and as anhedral crystals of ∼10-20 μm. The crystals are randomly oriented.

The clasts The number of clasts is low. One clast consisting of amphibole+omphacite+kyanite +biotite+dolomite is observed, see Fig. 4.14c. The shape is overall spherical, with diameter of 300 μm, and an irregular boundary to the pst matrix. Amphibole+omphacite+kyanite occur as in the matrix, but with larger grain size. Biotite and dolomite is anhedral, with grain size ∼5 μm. The amphibole in this clast contain Cl (detected by EDS).

Newly grown minerals include garnet, with a highly variable grain size,∼3-80 μm. Small garnets are aligned along the margin of pst, and the size increase towards the center of the pst, see Fig. 4.14d. The garnets are anhedral to subhedral. The largers ones have developed one or more crystal face, while the rest show an irregular boundary. The small garnets have few or no inclusions, the number of inclusion seems to increase with the size of the garnet grain.

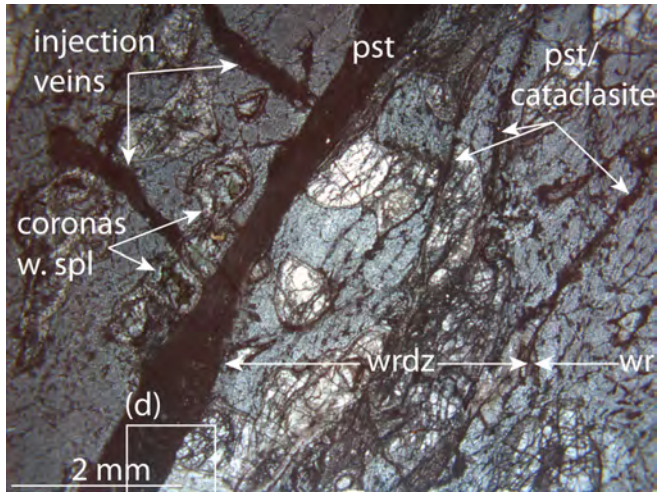

(a) Pst fault vein with injection veins. Several narrow deformation zones of pst and/or cataclasite in the wrdz run subparallel to pst vein (HV11, ppl).

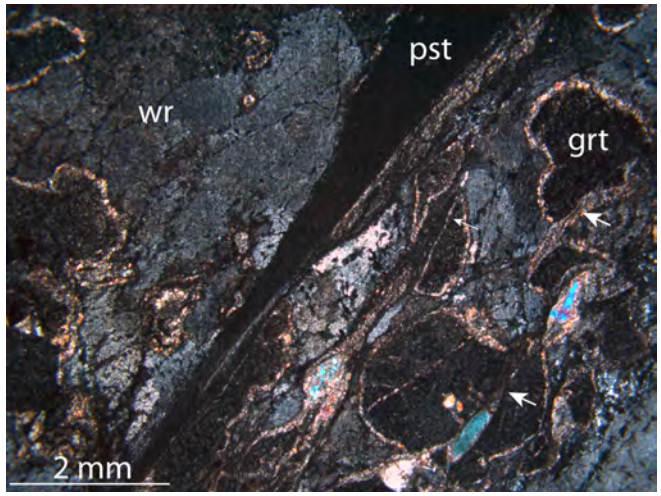

(b) Pst in recrystallized wr. Arrows point out deformation zones crossing garnet crystals (HV11, xpl).

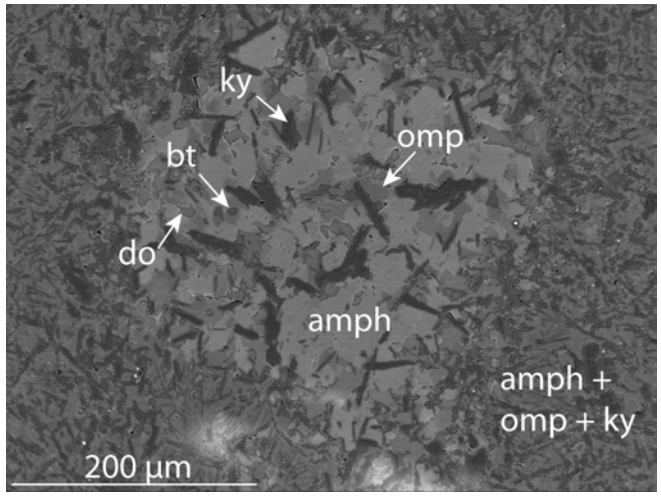

(c) Clast of amph+omp+ky+bt+do in pst vein of fault HVc (HV11, BSE).

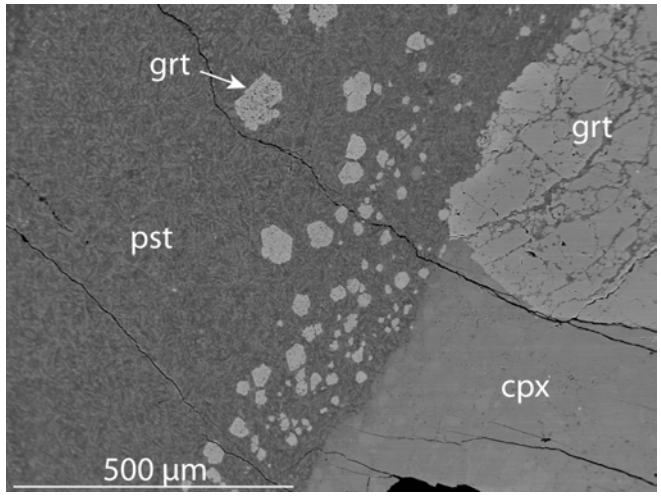

(d) Sharp transition between wr and pst with garnet microliths. A higher number of fractures is observed in grt than in cpx (HV11, BSE).

Figure 4.14: *Micrographs (a-b) and BSE-images (c-d) of wr, wrdz and pst of fault HVc at Husebøvatnet locality.*

4.3 Ådnefjell

4.3.1 The Pristine Mineralogy of the Wall-Rock

The pristine wall-rock of Ådnefjell has the same mineralogy as the pristine wall-rock at Hundkjeften and Husebøvatnet, described in Section 4.1.1. The modal composition of pyroxene and garnet is higher than at Hundkjeften, on expence of plagioclase.

4.3.2 The Wall-Rock adjacent to Fault Zone

The appearance of the wall-rock adjacent to the fault zone is similar to what discribed for Husebøvatnet in Section 4.2.2. However, some different features are pointed out in this section.

Pinning structures formed by grain boundary migration is observed in wall-rock adjacent to fault ÅFSa, see Fig. 4.15a. Plagioclase moves the grains boundary into garnet and clinopyroxene. The twins in plagioclase is in most grains destroyed, and zoisite needles has partly replaced the plagioclase. Garnet are only partly surrouded by a single reaction rim, on the boundaries to clinopyroxene.

4.3.3 The Wall-Rock Damage Zones and the Pseudotachylytes

Fault ÅFSa

Fault ÅFSa is briefly discribed, as no thin section from this fault were investigated in the EMP. It is therefore not determined whether ÅFSa is an eclogite or amphibolite facies pst.

The vein geometry of fault ÅFSa is a fault vein. No injection veins are observed. The fault vein in general have sharp boundaries to the wall-rock, where grains are gut sharply off, like the lower contact of the pst in Fig 4.15c. This image also show that the boundary may also be undulose, like the upper contact of the pst.

The pst of ÅFSa can be divided into Type 1 and Type 3 pst, based on color and the textural appearance in the optical microscope.

Type 1 pst resembles the Type 1 pst described for Fault HVb in Section 4.2.3 and the pst described from the rest of the faults studied in this thesis. It has a dark green-black color in thinsection. See center of Fig. 4.15c for this type of pst. Few clasts are observed. The small pyroxene clast in center of Fig. 4.15d is thermally rounded.

Type 3 pst is fine grained, and pale gray in ppl. It resembles the Type 2 pst described for Fault HVb in Section 4.2.3, except it lacks the banding of alternating dark and pale gray layers. Clinopyroxene is observed a clasts, see Fig. 4.15b. The clasts are angular, and their size varies between $\sim$10μm and $\sim$2 mm.

When considering the boundaries between type 1 and 3 pst, they resemble the boundary between type 1 pst and thermally rounded clasts. In middle right of Fig. 4.15c the type 1 pst (dark) makes embayments into type 3 pst (pale gray). The variable appearance of the pst will be discussed in Chapter 7.

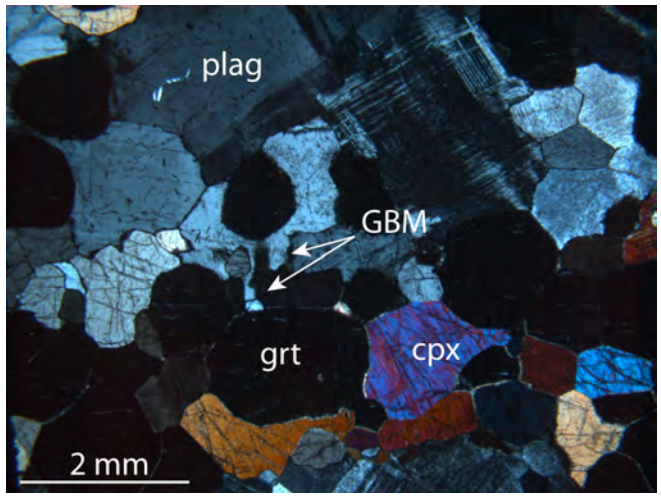

(a) Partly recrystallized wr of ÅFSa with GBM observed in plag (AFS2, xpl).

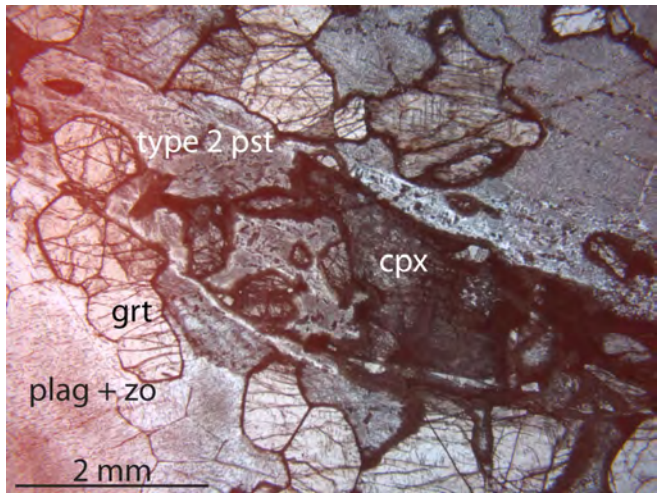

(b) Fault rock of ÅFSa upper left-lower right in partly recrystallized wr. Large fragments of cpx as clasts (AFS2, ppl).

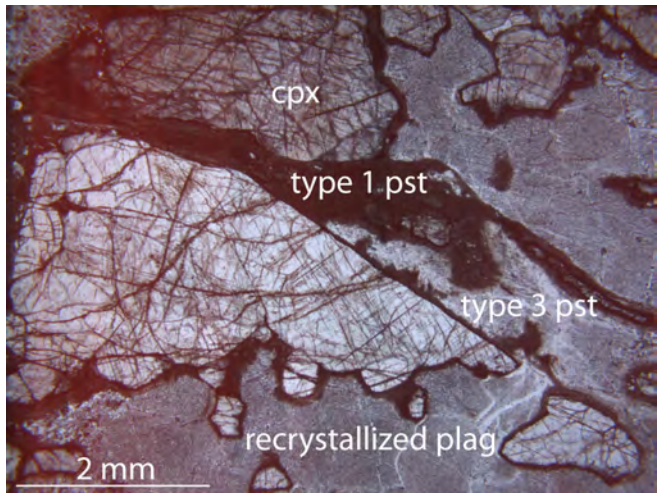

(c) Fault rock of ÅFSa upper left-lower rigth with both undulating and sharp contact to the cpx in wall-rock. Both type 1 (dark) and type 2 pst (pale) is shown (AFS2, ppl).

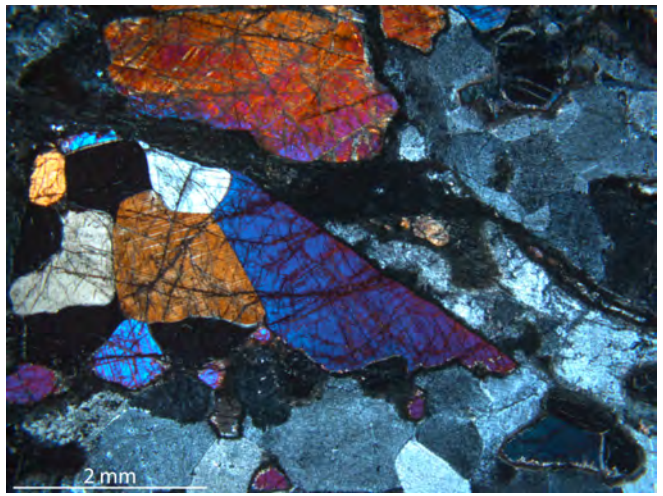

(d) Fault rock of ÅFSa upper left-lower rigth. Cpx have undulous extinction (AFS2, xpl).

Figure 4.15: *Wr, wrdz and pst/fault rock of fault ÅFSa at Ådnefjell locality.*

Fault ÅFSc

Fault ÅFSc is an eclogite facies pseudotachylyte. Since the sample from ÅFSc, hand specimen ÅFS9, is collected from the margin of a thick pst vein and does not show any relations to the wall-rock, the vein geometry of ÅFSc is not described.

The matrix mineral assemblage of the pst is omphacite+kyanite+amphibole. Grain size of the anhedral omphacite and amphibole crystals is $\sim 2\mu m - 20\mu m$, see Fig 4.16c. Kyanite is observed as needles $\leq$20 μm in length, and as anhedral crystals of ∼5-15 μm. The mineral grains appear randomly oriented, see Fig. 4.16b-4.16d.

The clasts have variable size, ranging between ∼75 μm and 1 mm, and are angular to thermally rounded, see Fig. 4.16a. Fragments of plagioclase are observed, as in upper right of Fig. 4.16a. This figure also display a larger clasts in the lower right enclosing a smaller clast. The outermost, largest clast, seen as the vertical band of dark gray in Fig 4.16b, consist of kyanite+omphacite+amphibole+quartz. This clast is ∼1 mm in diameter, and encloses a clast of garnet1. The garnet clast is ∼200 μm across, and is well rounded. The close-up in Fig. 4.16b reveals that the garnet, to the right in the image, is full of inclusions of kyanite+omphacite+dolomite.

Small anhedral to subhedral newly grown crystals of garnet2 is found in the matrix all over the pst. In Fig. 4.16a they are seen as tiny, spherical objects with dark core and pale rim. Fig. 4.16c and 4.16d show close-ups of such garnets. They are often surrounded by omphacite, which also occures as inclusions along with quartz, see Fig. 4.16c. Garnet2 crystals may have developed parts of one or more crystal faces, like in Fig 4.16c, but is often observed with highly irregular morphologies. The garnets in Fig. 4.16d are examples of the latter, one also showing a dendrite-like shape (pointed out).

Fault ÅFSd

The pst of Fault ÅFSd is an amphibolite facies pst. The wall-rock of ÅFSd show a gradual increase in deformation as approching the pst. From left to right, Fig. 4.17a show fractured wall-rock and wrdz. The pst is oriented vertical outside this image, to the right. Narrow zones of cataclasis is observed subparallel to faultvein both in wall-rock and in the wrdz. These cataclastic zones are $\sim 200\mu m$ in width. The wrdz consist of fine grained material, and fragments of highly fractured pyroxene and garnet.

The vein geometry of pst of fault ÅFSd is a fault vein, that splits in two strands some places. Fig. 4.17b show a part of the fault where the pst is observed as a ∼4 mm thick faultvein with a subparallel slip plane with a small amount of pst(left in Fig. 4.17b). The pst is gray-brown in thin section.

The matrix mineral assemblage of is plagioclase+K-feldspar+amphibole. The grain size is $\leq$10 μm, see Fig. 4.17d. Flow structures are observed in ppl e.g. , around the large plagioclase clast in the center right of Fig. 4.17b.

The clasts Plagioclase clasts of highly variable size is observed, ∼50 μm - 2 mm. A few clasts are angular, but most are thermally rounded. The pst also enclose large fragments of wall-rock that consist of plagioclase+clinopyroxene.

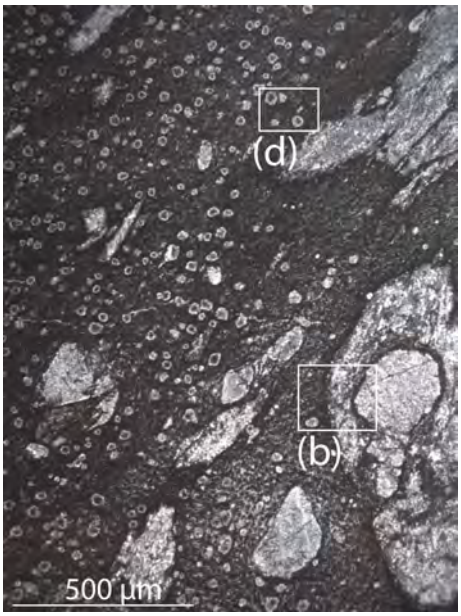

(a) *Matrix, clasts and newly grown garnets in pst vein (ÅFS9, ppl).*

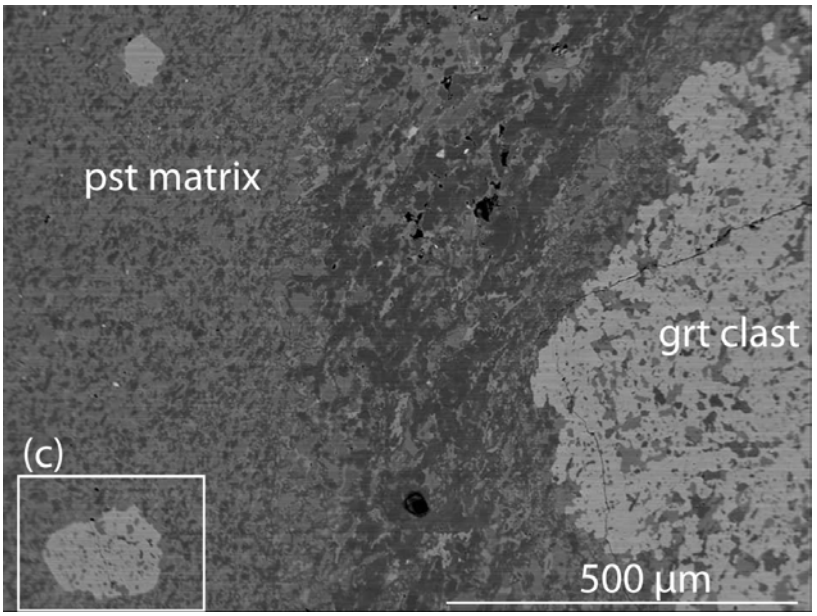

(b) *Grt1 clast with inclusions of ky+omph+dol inside clast of omph+ky+amph+qtz in pst matrix(ÅFS9, BSE).*

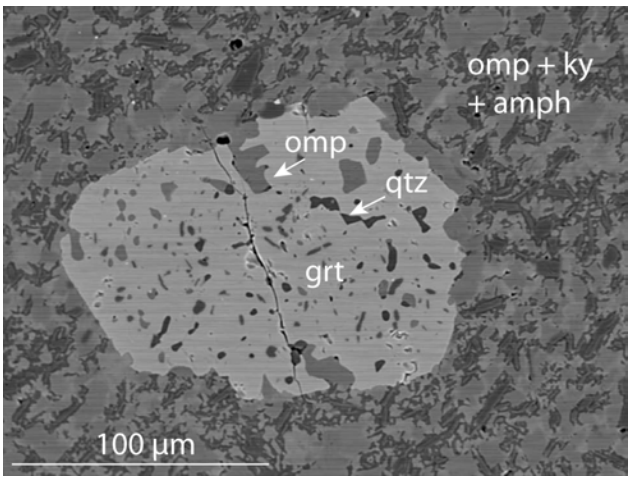

(c) *Garnet2 with inclusion of omph+qtz partly surrounded by omph in pst matrix (ÅFS9, BSE).*

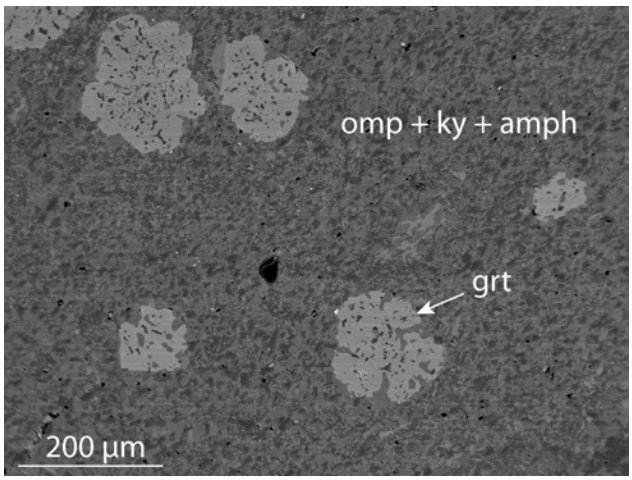

(d) *Garnet2 in pst matrix of omph+amph+ky (ÅFS9, BSE).*

Figure 4.16: *Micrograph (a) and BSE-images (b-d) of pst from fault HVc at Ådnefjell locality. Sample ÅFS9 was taken from a thick pst vein only, no relations to the wall-rock were therefor observed in this thin section.*

The dark patches observed in the pst in ppl in Fig. 4.17b and 4.17c is amphibole±other mineral(s). From Fig. 4.17b it looks as the amphibole-aggregates is an overprinting feature, and that it is found both in wall-rock, pst matrix, clasts in pst, and also on the margin between matrix and clasts.

Quench textures Spherulites are observed in the main fault vein, see Fig. 4.17c. Fig. 4.17d is a close-up BSE-image. The diameter of the spherulites is typically ∼100 μm. The spherulites grow in plagioclase, and consist of feldspar2+one other mineral (not determined).

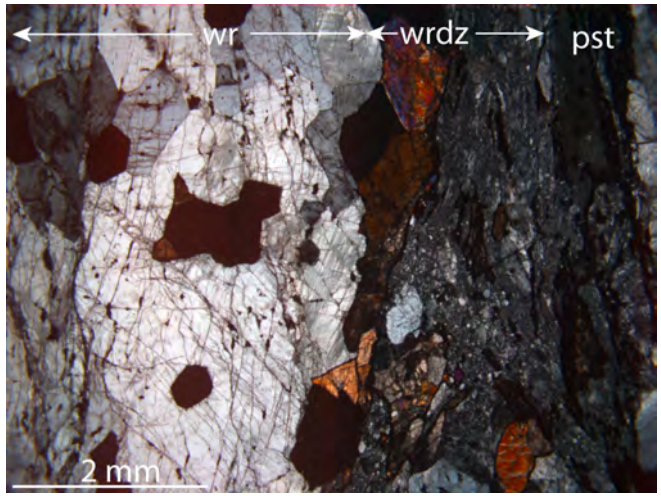

(a) *Wall-rock and wall-rock damage zone with cataclastic material. Fault ÅFSd oriented vertical to the right of this image (ÅFS10, xpl).*

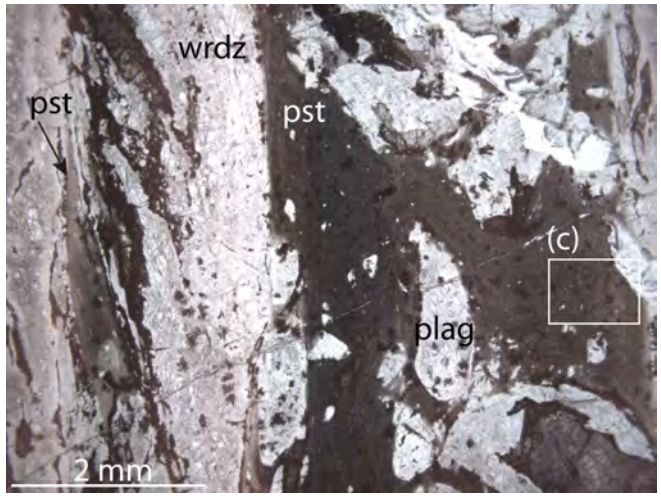

(b) *Paired slip surfaces of pst oriented vertical, with damaged wall-rock in between. Note flow structures around large plagioclase clast in pst in middle right (ÅFS10, ppl).*

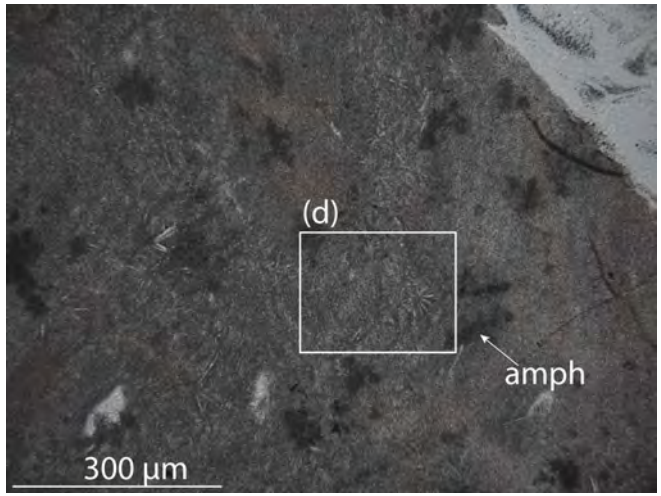

(c) *Texture of the pst matrix with spherulites and aggregates of amphibole (ÅFS10, ppl).*

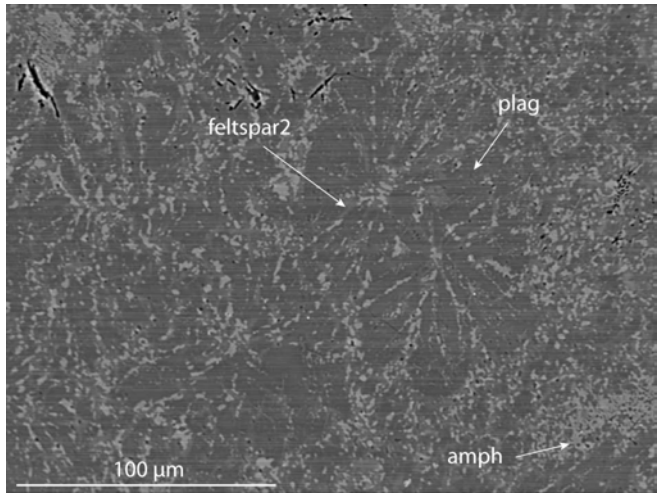

(d) *Spherulites of feldspar2 in plag in pst matrix (ÅFS10,BSE).*

Figure 4.17: *Micrographs (a-b) and BSE-images (c-d) of wall-rock, wall-rock damage zone and pst associated with fault ÅFSd at Ådnefjell locality.*

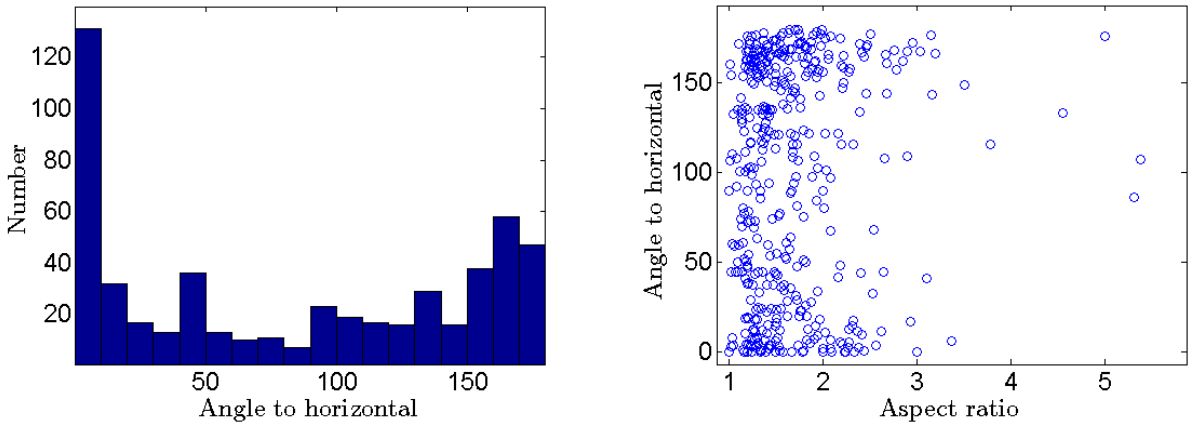

(a) *Number of clasts oriented within a certain range of angles to the horizontal, which is subparallel to the strike of the fault vein.*

(b) *The angle of the clasts plotted against the aspect ratio.*

Figure 4.18: *Plots from analyses of the orientation of particles (clasts) in pst matrix.*

4.4 Results from Image Analyses on HK4

Image analyses were applied for one micrograph, Fig. 4.19a, from fault HK at Hundkjeften. The micrograph, described in Fig. 4.5a in Section 4.1.4, show a pst fault vein with injection veins and clasts of variable size.

The aim of the image analyses was to get quantitative information on the orientation of clasts in the pst vein.

The binary image in Fig. 4.19b show that the margins of the pst vein only host small clasts, while in the center of the pst the clasts have the whole range of sizes. 533 particles (clasts) were recognized by the software, all marked by number in Fig. 4.19c. The histogram in Fig. 4.18a show the number of clasts that have the major axis of the best fit ellipse at a certain angle to the horizontal, which is subparallel to the fault vein. A significantly higher number of the clasts have their longest axis oriented with a low angle to the strike of the fault, compared to the number of clasts having a high angle.

To see if the aspect ratios have any influence on the oriantation of the clasts, this value is plotted against the angle to the horizontal in Fig. 4.18b. The values of the aspect ratios vary from 1 (perfect circle) and up to ∼5,5. The plot reveal that very few clasts have high aspect ratioes, and that these clasts are oriented from subhorizontally to nearly orthogonal to the strike of the fault vein.

Most of the clasts have an aspect ration between 1 and 2,5. Fig. 4.18b confirm what observed in Fig. 4.18a; there are more clasts oriented with a low angle to the horizontal than there are clasts with a high angle to the horizontal. Two clustres are observed, for aspect ratios ∼1,5 and angles below 15 and above 150 to the horizontal. Also, there is a relatively higher dispersion in aspect ratio among the clasts oriented sub-parallel to the fault vein compared to the clasts oriented with a high angle to the fault vein.

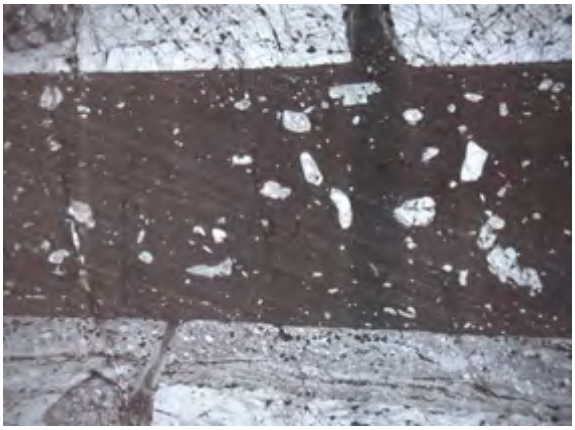

(a) Original micrograph of fault vein with injection veins and clasts (HK4, ppl).

(b) Binary image of (a) processed in photoshop and ImageJ (HK4).

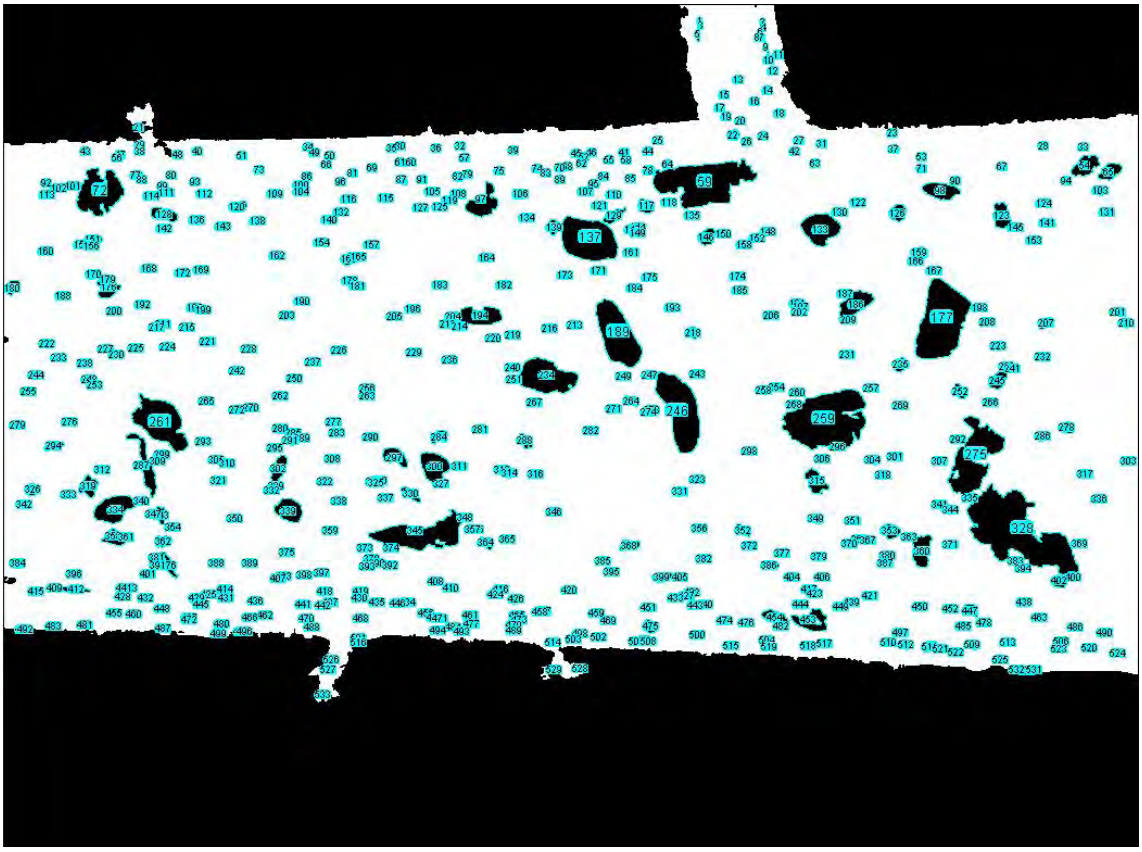

(c) Binary image analyzed using ImageJ. 533 clasts were detected and anlayzed.

Figure 4.19: *Pre- and post processed images of parts of thin section HK4.*

Chapter 5

Mineral Chemistry: From Wall Rock to Pseudotachylyte

This chapter addresses the changes in composition of the three most abundant minerals in the granulite facies anorthosites; plagioclase, garnet, and clinopyroxene, from wall-rock to pst.

5.1 Plagioclase

The plagioclase in the granulite facies anorthosite wall-rock has a composition of $\sim An_{50}$. It has a high content of alumina, the Al_2O_3 accounts for $\sim$28wt%. Plagioclase in wrdz have a fairly similar composition, with An_{52} (Analysis HK4 6/2). Plagioclase is present in the pst both as clasts from the wall-rock and as matrix mineral. The composition of these vary, but most analyses are also around An_{50}. No decrease in the An-component was observed in the amphibolite facies pst, contrary to what Kuhn (2002) reported from amphibolites in the same area. This might be due to the limited number of analyses taken (n=10 in total for plagioclase).

In contrast, two of the analyses from Hundkjeften show a remarkable increase in the An-component. Plagioclase in fractured wall-rock mm's from the pst is An_{75}, while one analysis of plagioclase in the pst-matrix has an An-content of An_{81}. Such high An-contents of plagioclase have been observed from this areas earlier (Austrheim, 2013), but will not be addressed in this thesis. The composition of plagioclase is listed in Tab.2.

5.2 Garnet

The primary garnet, grt1, in the wall-rock has a composition of $\sim Alm_{30}Prp_{46}Gros_{24}$ (analysis HK16-2/1). Except a slightly higher Gros-component and lower Prp-component of garnet in the wrdz there is not much variation observed in the grt1, see Fig 5.1. Grt1 is also found growing in fractures or exsolution lammelae in cpx1, these show a slightly higher value of the almandine-component.

Grt2 show a wide variety of compositions, with $Alm_{7-54}Prp_{6-43}Gros_{11-87}Sps_{0-2}$. Typical compositions are, however, either grossular-rich or almandine-rich with a relatively low content of the pyrope-component, like seen in the two ellipses in Fig 5.1. Newly grown grains of grt2 in pst correspond to the group of highest content of almandine, and have a variable content of grossular vs.

Plagioclase

Sample	HK16	HK4	HK4	HK4	HK2	HK2	HV11	HV7	HV7	HV7
Analysis nr.	4/1.	13/1.	23/1.	6/2.	16/2.	17/2.	18/3.	3/5.	9/5.	10/5.
SiO2 [wt%]	55,74	55,36	58,72	55,96	55,15	61,17	57,22	56,97	63,48	61,07
Al2O3	28,15	28,24	25,68	27,93	27,84	24,31	26,61	26,93	22,48	23,72
FeO	0,06	0,04	0,16	0,10	0,03	0,06	0,10	0,35	0,02	0,05
CaO	10,57	10,73	7,90	10,38	10,18	6,01	8,71	8,85	4,31	5,81
Na2O	5,52	5,62	7,38	5,65	5,69	7,92	6,87	6,52	9,28	8,63
K2O	0,44	0,23	0,15	0,10	0,20	0,34	0,13	0,18	0,52	0,24
Total	100,48	100,21	99,99	100,12	99,10	99,80	99,64	99,80	100,09	99,50
Structural formulae*										
Si	10,06	8,99	8,76	9,95	9,99	9,97	10,00	9,92	10,04	10,00
Al	5,91	6,97	7,17	6,00	5,97	6,00	5,96	6,03	5,92	5,96
Fe	0,01	0,01	0,02	0,01	0,01	0,01	0,02	0,02	0,01	0,01
Ca	2,02	3,04	3,30	2,12	2,10	2,08	2,07	2,10	2,01	2,04
Na	1,92	0,87	0,78	1,90	1,89	1,94	1,93	1,97	1,99	1,97
K	0,07	0,15	0,01	0,05	0,05	0,02	0,03	0,02	0,08	0,06
Total	19,98	20,03	20,05	20,03	20,00	20,02	20,00	20,06	20,04	20,03
An	*50*	*75*	*81*	*52*	*52*	*51*	*51*	*51*	*49*	*50*

*Calculated on 32 oxygens

Table 5.1: *Plagioclase analyses*

pyrope. THis is in accordance with what reported on garnets by Austrheim et al. (1996). Grt2 with high content of grossular are found in reaction rims in wall-rock. Most analyses of grt2 give compositions of $\sim Alm_{45}Prp_{34}Gros_{21}$. The chemistry of the grt2 is similar to what Kuhn (2002) describe as eclogite facies garnets, related to mineral reactions consistent with the eclogitization processes. Two such garnets are observed in fault HK, where pst has an amphibolite facies mineralogy, and no omphacite is observed. These garnets are associated with plagioclase, see Fig. 4.6c,Section 4.1.4 in Chapter 4. In eclogite facies matrix the grt2 are typically assiciated with omphacite, like in Fig. 4.16c,Section 4.3 in Chapter 4.

The andradite-component has not been calculated as the structural formulae suggest that Fe^{3+} is low. The spessartine-component is also low, and in most analyses zero.

Fig 5.2 show grt in wall-rock, on the margin to the pst, and newly grown garnet grains in the pst. Analyses, found in Tab. 5.3, reveal a change in composition from a pyrope-rich grt1 in wall-rock to a almandine-rich grt2 in the pst. Fig 5.2b show a highly fractured garnet that, away from the pst (analysis HV11-8/3), have a composition of $Alm_{28}Prp_{52}Gros_{19}$. The fractures are filled with omphacite. The margin of the garnet, towards the pst, appears brighter than the rest of the garnet. Analysis HV11-10/3 reveals an increase in Fe and a decrease in Mg, and the composition is $Alm_{37}Prp_{44}Gros_{19}$.

The newly grown grt2 in the pst in Fig. 5.2 have an even higher Fe-content and lower Mg-content, and the composition is $Alm_{42-44}Prp_{36-38}Gros_{19}$. The analysis is taken in one inclusion-free newly grown grt2 (analysis HV11-11/3 in Fig. 5.2b) and one newly grown grt2 with inclusions (analysis HV11-5/3 in Fig 5.2c). Notice how the size and amount of inclusions in the newly grown grt2 increase from the margin of the pst and towards the center of the pst-vein. On the margin the size is $\geq 5\ \mu m$, while closer to the center of the pst the are $\leq 100\ \mu m$. Most of the grt2 have few or non of their crystal faces developed, an exception is the grt in the upper, left corner of Fig. **??**, that has two crystal faces developed.

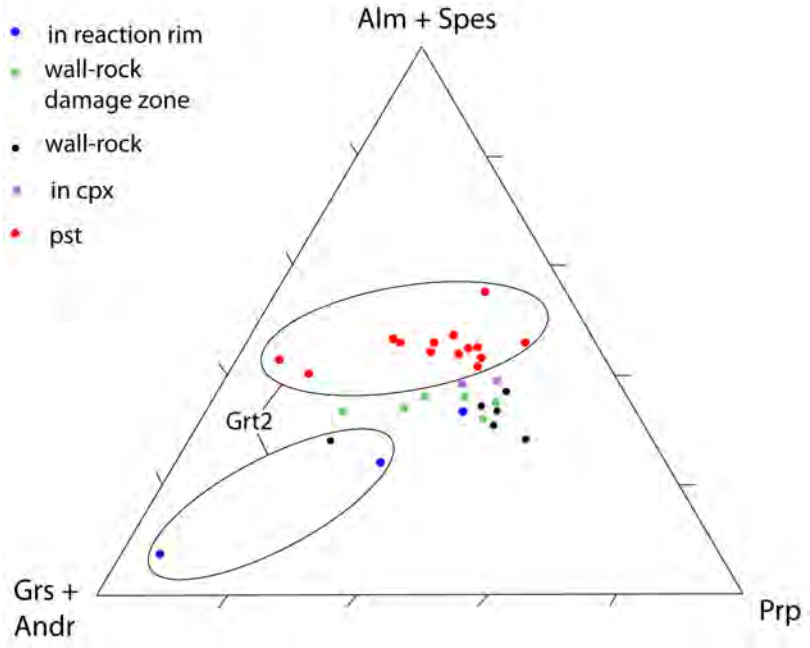

Figure 5.1: *Garnet chemistry plotted as the components Alm+Spes-Grs+Andr-Prp. Garnet2 is encircled, the rest of the analyses are garnet1.*

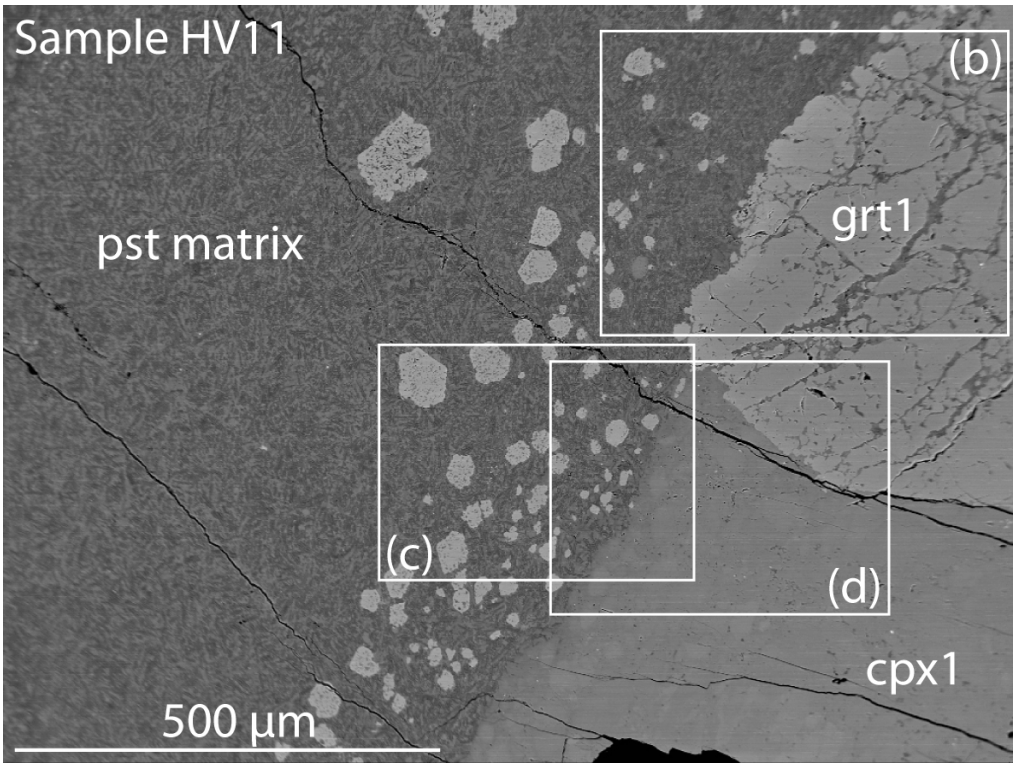

(a) *Overview of transition from wall-rock (lower right) to pseudotachylyte (upper left) (HV11, BSE).*

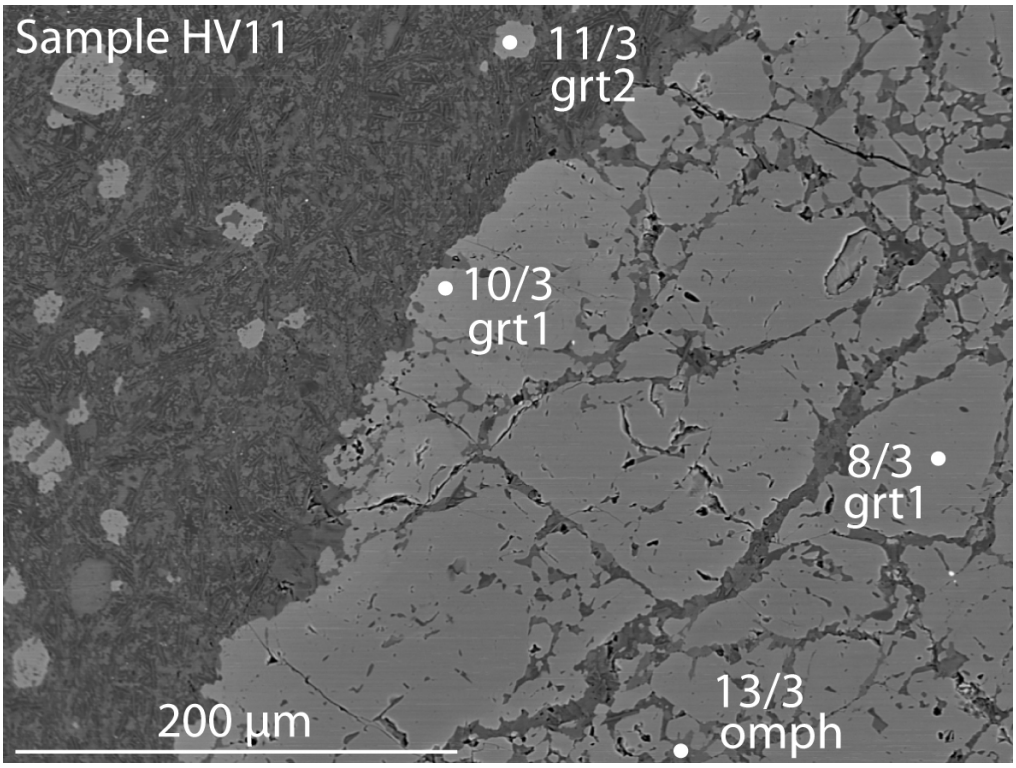

(b) *Fractures in Grt1 of wall-rock filled with omph. Grt2 as newly grown grain in pseudotachylyte has few inclusions. (HV11, BSE)*

Figure 5.2: *Continued on the following page.*

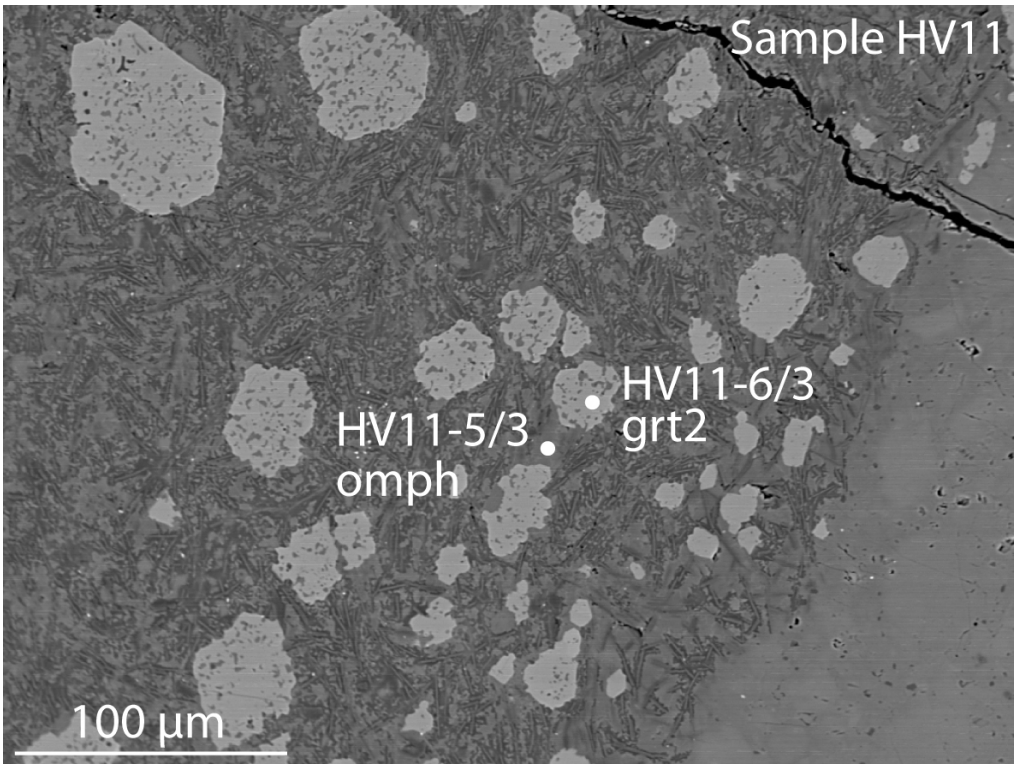

(c) Omph in the pst matrix and a newly grown grt2 with inclusions. Notice the uneven morphologies of most of the anhedral grt crystals. The size of newly grown grains of grt increase from the margin towards the center of the pst vein. The tiniest garnets occur on the margin have few or no inclusions, while the bigger have more inclusions.

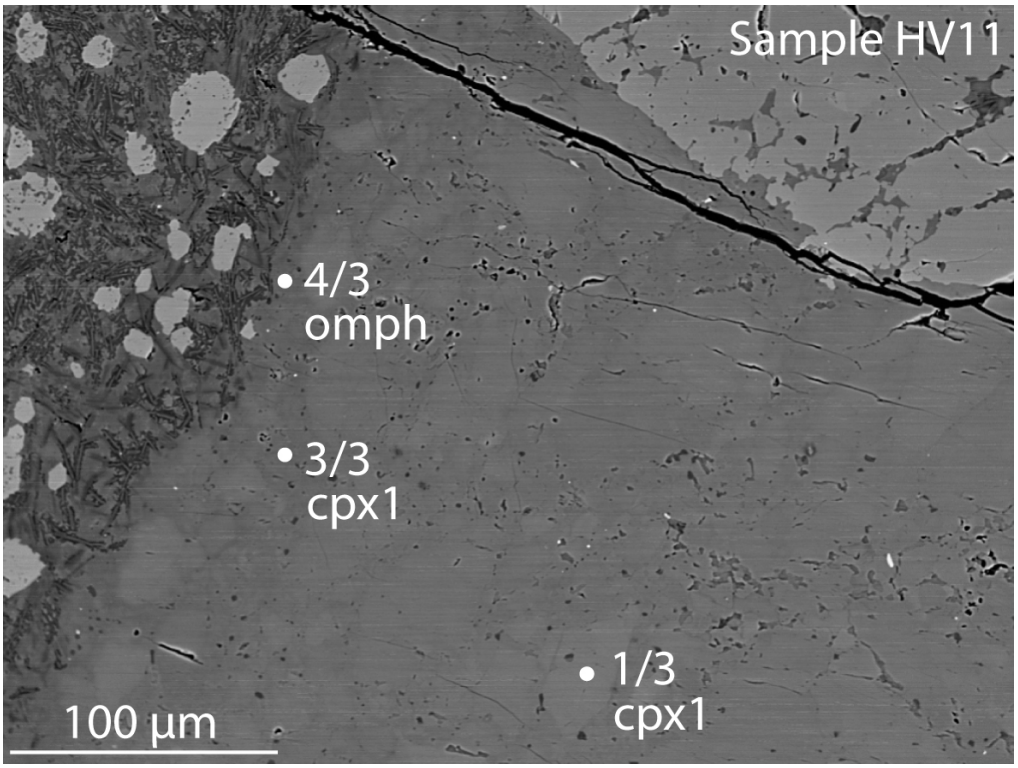

(d) Cpx1 of wall-rock becomes more Na-rich approaching the pst, and is classified as an omphacite on the edge of the grain. Notice the two different gray-shades in the cpx. The darkest

Figure 5.2: *BSE-images of sample HV11 from fault HVb at Husebøvatnet. When going fom wall-rock to pseudotachylyte the mineral chemistry change from cpx1 to omph, and from grt1 to grt2.*

Garnet

Sample	HK16	HK16	HK16	HK16	HK4	HK4	HK4	HK4	HK4	HK4	HK4	HK4	HK4	HK2	HK2	HK2	HK2
Analysis nr.	2/1.	8/1.	10/1.	12/1.	14/1.	15/1.	18/1.	7/2.	8/2.	9/2.	10/2.	11/2.	12/2.	24/2.	25/12.	28/2.	29/2.
[wt%]	Grt1	Grt1	Grt1	Grt2	Grt2	Grt1	Grt2	Grt1	Grt1	Grt1	Grt1	Grt1	Grt1	Grt1	Grt1	Grt2	Grt2
	wr	rx.r	wr	rx.r	rx.r	wr	wr	wrdz	wrdz	wrdz	wrdz	wrdz	wrdz	in cpx	in cpx	prt	pst
SiO2	40,80	40,57	40,48	40,66	40,33	40,47	39,70	40,61	40,61	40,24	39,64	39,83	39,86	40,09	39,79	39,24	39,27
TiO2	0,27	0,00	0,22	0,04	0,04	0,20	0,57	0,28	0,25	0,20	0,17	0,17	0,13	0,07	0,11	0,07	0,16
Al2O3	22,56	23,75	22,95	22,15	22,91	22,39	20,50	22,60	22,74	22,34	22,06	22,19	21,96	23,71	22,64	21,84	22,20
FeO	14,95	15,50	15,93	11,92	3,60	16,61	14,01	16,04	15,84	16,82	16,53	17,05	15,88	17,61	18,54	21,92	21,12
MnO	0,27	0,09	0,18	0,09	0,06	0,33	0,16	0,27	0,22	0,29	0,21	0,34	0,28	0,30	0,30	0,31	0,29
MgO	12,97	10,54	12,70	8,88	1,61	11,63	6,16	12,10	11,84	11,69	8,14	8,95	5,66	9,79	11,60	8,25	8,99
CaO	9,27	9,90	8,91	16,88	33,01	9,35	18,82	8,54	9,05	8,87	13,35	11,51	16,82	9,54	7,20	7,83	8,05
Total	101,09	100,35	101,37	100,63	101,56	100,98	99,92	100,43	100,56	100,45	100,10	100,03	100,59	101,10	100,17	99,47	100,08
Structural fomulae*																	
Si	2,99	3,00	2,96	3,01	2,99	2,99	3,02	3,00	3,00	2,99	2,99	3,00	3,01	2,97	2,97	3,01	2,98
Ti	0,01	0,00	0,01	0,00	0,00	0,01	0,03	0,02	0,01	0,01	0,01	0,01	0,01	0,00	0,01	0,00	0,01
Al	1,95	2,07	1,98	1,94	2,00	1,95	1,84	1,97	1,98	1,96	1,96	1,97	1,96	2,07	2,00	1,97	1,99
Fe	0,92	0,96	0,98	0,74	0,22	1,03	0,89	0,99	0,98	1,04	1,04	1,07	1,00	1,09	1,16	1,41	1,34
Mn	0,02	0,01	0,01	0,01	0,00	0,02	0,01	0,02	0,01	0,02	0,01	0,02	0,02	0,02	0,02	0,02	0,02
Mg	1,42	1,16	1,39	0,98	0,18	1,28	0,70	1,33	1,30	1,30	0,92	1,00	0,64	1,08	1,29	0,94	1,02
Ca	0,73	0,78	0,70	1,34	2,62	0,74	1,53	0,68	0,72	0,71	1,08	0,93	1,36	0,76	0,58	0,64	0,66
Total	8,02	7,97	8,03	8,02	8,01	8,02	8,03	8,00	8,00	8,02	8,02	8,01	8,00	7,99	8,02	8,00	8,01
Alm	0,30	0,33	0,32	0,24	0,07	0,33	0,28	0,33	0,32	0,34	0,34	0,35	0,33	0,37	0,38	0,47	0,44
Prp	0,46	0,40	0,45	0,32	0,06	0,42	0,22	0,44	0,43	0,42	0,30	0,33	0,21	0,37	0,42	0,31	0,34
Spes	0,01	0,00	0,00	0,00	0,00	0,01	0,00	0,01	0,00	0,01	0,00	0,01	0,01	0,01	0,01	0,01	0,01
Grs	0,24	0,27	0,23	0,44	0,87	0,24	0,49	0,22	0,24	0,23	0,35	0,31	0,45	0,26	0,19	0,21	0,22

*Calculated on 12 O

Table 5.2: *Composition of garnet 1 and 2 from Hundkjeften.*

Garnet

Sample	HV11	HV11	HV11	HV11	HV11	HV5	HV4	HV4	HV7	HV7	ÅFS9	ÅFS9	ÅFS9
Analysis nr.	6/3	8/3	10/3	11/3	14/3	27/3	16/4	21/4	2/5	13/5	6/4	12/4	13/4
	Grt2	Grt1	Grt1	Grt2	Grt2	Grt2	Grt2	Grt2	Grt2	Grt2	Grt2	Grt2	Grt2
[wt%]	pst	wr	wr	pst	pst	pst	pst	pst	pst	pst	pst	pst	pst
SiO2	39,37	40,92	40,15	38,97	39,80	39,49	39,24	39,48	38,80	38,11	39,06	39,23	39,08
TiO2	0,11	0,15	0,11	0,12	0,03	0,02	0,03	0,06	0,19	0,30	0,04	0,04	0,13
Al2O3	22,11	23,23	22,69	22,46	22,30	22,14	21,89	21,94	22,30	25,11	21,54	21,58	21,80
FeO	21,12	14,11	17,93	20,14	21,90	20,95	25,48	20,37	18,21	18,12	20,71	21,59	21,34
MnO	0,39	0,24	0,31	0,36	0,10	0,56	0,29	0,28	0,32	0,15	1,06	0,93	1,03
MgO	9,69	14,85	12,04	10,33	11,74	9,39	8,30	7,71	3,34	1,71	6,19	6,11	7,89
CaO	7,27	7,57	7,45	7,21	4,28	7,43	4,83	10,34	17,32	16,90	11,14	10,69	9,02
Total	100,06	101,08	100,69	99,58	100,16	100,00	100,07	100,18	100,48	100,40	99,74	100,16	100,29
Structural fomula*													
Si	2,99	2,97	2,98	2,96	2,99	3,00	3,01	3,00	2,98	2,91	3,01	3,02	2,99
Ti	0,01	0,01	0,01	0,01	0,00	0,00	0,00	0,00	0,01	0,02	0,00	0,00	0,01
Al	1,98	1,99	1,98	2,01	1,98	1,98	1,98	1,97	2,02	2,26	1,96	1,96	1,96
Fe	1,34	0,86	1,11	1,28	1,38	1,33	1,64	1,30	1,17	1,16	1,34	1,39	1,36
Mn	0,03	0,01	0,02	0,02	0,01	0,04	0,02	0,02	0,02	0,01	0,07	0,06	0,07
Mg	1,10	1,61	1,33	1,17	1,32	1,06	0,95	0,87	0,38	0,20	0,71	0,70	0,90
Ca	0,59	0,59	0,59	0,59	0,35	0,60	0,40	0,84	1,42	1,38	0,92	0,88	0,74
Total	8,02	8,03	8,02	8,03	8,02	8,01	8,00	8,01	8,00	7,94	8,01	8,00	8,02
Alm	0,44	0,28	0,36	0,42	0,45	0,44	0,54	0,43	0,39	0,42	0,44	0,46	0,44
Prp	0,36	0,52	0,44	0,38	0,43	0,35	0,32	0,29	0,13	0,07	0,23	0,23	0,29
Spes	0,01	0,00	0,01	0,01	0,00	0,01	0,01	0,01	0,01	0,00	0,02	0,02	0,02
Grs	0,19	0,19	0,19	0,19	0,11	0,20	0,13	0,28	0,48	0,50	0,30	0,29	0,24

*Calculated on 12 O

Table 5.3: *Garnet analyses from Husebøvatnet and Ådnefjell.*

5.3 Pyroxene

The primary clinopyroxene, Cpx1, in the granulite facies anorthosite wall-rock is diopsidic in composition, with Jd = 0,06. Al-content is between 12,49 and 16,06 wt% Al_2O_3, and Na_2O between 1,40 and 2,72 wt%. The Mg/Mg-Fe-ratio is typically ∼76 at Hundkjeften and ∼83 at Husebøvatnet. Fe^{3+} is low, ranging fra zero and up to 0.06. The primary clinopyroxene is also present in altered wall-rock, and as clasts in pst. The analyses reveal little variation of the chemical composition, except for HK165/11, regardless of where the analysis is taken. One of the clasts in the pst have an increased Na_2O-content, and Jd=18.

Even in the wall-rock of sample HK16, drilled 70 cm away from the fault plane, reactions have taken place. Cpx1 on grain boundary between cpx and scp show a slight increase in Al_2O_3 (16,06wt%) and Na_2O (2,45wt%) and a Jd-content of 0,16. Cpx in reaction rim around an aggregate of spinel and garnet1 has an even higher content of Na_2O (3,06wt%), and an Al-content of 25,98wt% Al_2O_3, and is referred to as **Cpx2**. Cpx2 has Jd-content of 0,21, lower Ca-Ts and higher En+Fs compared to Cpx1.

Omphacite is present in wall-rock and pst at Husebøvatnet and Ådnefjell, but has not been observed at Hundkjeften. It has been observed in wall-rock, and as vein-fill in fractured wall-rock, adjacent to pst fault veins. In pst it is found as a matrix mineral, in clasts, and as inclusions in newly grown garnet. The omphacite has 5,37-6,78 wt% Na_2O and Jd=0,34-0,45. The contents of Jd is highest in the matrix of and inclusions in clasts in pst.

An example of the development from cpx1 to omphacite from wall-rock to pst is shown in Fig 5.2. Sample HV11 is from the eclogite-facies pst-bearing fault HVb at Husebøvatnet locality. The clinopyroxene1 in Fig 5.2d consist of material of two different gray shades. Angular to subrounded fragments of the palest gray shade (analysis HV11-1/3) is surrounded by material of the darker gray-shade (analysis HV11-3/3). The pale gray clinopyroxene1 has a Ca-content of 22,42 wt%Ca_2O_3. This value decrease to 20,92 in the darker gray clinopyroxene1. The Fe- and Mg-content also show a slight decrease from the pale to the dark gray cpx1. The similarity of the composition of analysis HV11-1/3 with the primary clinopyroxene from Hundkjeften suggests the pale gray is the primary, old cpx1. On the margin to the pst the pyroxene is classified as an omphacite (analysis HV11-4/3), with an even lower content of Ca, Fe and Mg. The Na-content, however, increase from 1,91 wt% Na_2O in analysis HV11-1/3, via 2,62 in analysis HV11-3/3, to 5,60 wt% in analysis HV11-4/3. The Jd-content of this omphacite is 0,36.

Omphacite in the matrix of the pst, analysis HV11-5/3 in Fig 5.2c, differs even more from the primary cpx1, with 6,51 wt% Na_2O. The Jd-content is 0,45, which is the highest value obtained. Omphacite in veins in fractured wall rock of grt1, analysis HV11-13/3 in Fig 5.2b, has a Na-content of 5,60 wt% of Na_2O, and a Jd-content of 0,36.

Clinopyroxene										
Sample	HK16	HK16	HK16	HK4	HK4	HK2	HK2	HK2	HK2	HK2
Analysis nr	1/1.	5/1.	9/1.	17/1.	13/2.	18/2.	19/2.	20/2.	21/2.	26/2.
Mineral	Cpx1	Cpx1	Cpx2	Cpx1	Cpx1	Cpx1	Cpx1	Cpx1	Cpx1	Cpx1
[wt%]	wr	rx.rim	rx.rim	wr	clast	wr	wr	wr	wr	clast
SiO2	44,70	47,42	48,87	44,55	47,75	46,78	46,33	45,63	45,91	48,10
TiO2	2,19	0,15	0,04	2,54	0,98	1,55	1,53	1,55	1,51	1,29
Al2O3	14,31	16,06	25,98	14,75	12,49	14,00	14,30	13,68	13,61	13,25
Cr2O3	0,00	0,00	0,00	0,03	0,02	0,03	0,03	0,00	0,01	0,00
FeO	6,16	5,07	2,76	4,76	6,29	4,57	4,38	4,99	5,08	5,30
MnO	0,00	0,03	0,03	0,00	0,05	0,00	0,03	0,02	0,04	0,04
MgO	9,62	8,40	7,30	9,49	9,23	9,50	9,83	9,67	9,66	9,14
CaO	21,95	21,08	12,69	22,62	21,47	21,24	22,41	22,51	22,15	19,52
Na2O	1,71	2,45	3,06	1,52	1,88	1,98	1,59	1,51	1,40	2,72
K2O	0,00	0,05	0,02	0,01	0,03	0,04	0,09	0,00	0,01	0,08
Total	100,64	100,66	100,72	100,27	100,16	99,65	100,43	99,56	99,38	99,37
Mg/Mg+Fe	73,58	74,71	82,53	78,06	72,36	78,76	80,01	77,54	77,23	75,46
Structural formulae*										
Si	1,63	1,72	1,74	1,63	1,75	1,72	1,69	1,68	1,70	1,77
Al IV	0,37	0,28	0,26	0,37	0,25	0,28	0,31	0,32	0,30	0,23
Al VI	0,25	0,40	0,83	0,27	0,29	0,32	0,30	0,28	0,29	0,34
Ti	0,06	0,00	0,00	0,07	0,03	0,04	0,04	0,04	0,04	0,04
Cr	0,00	0,00	0,00	0,00	0,00	0,00	0,00	0,00	0,00	0,00
Fe3+	0,06	0,02	0,00	0,03	0,02	0,01	0,02	0,03	0,01	0,01
Fe2+	0,13	0,13	0,08	0,11	0,18	0,13	0,11	0,12	0,14	0,15
Mn	0,00	0,00	0,00	0,00	0,00	0,00	0,00	0,00	0,00	0,00
Mg	0,52	0,45	0,39	0,52	0,51	0,52	0,53	0,53	0,53	0,50
Ni	0,00	0,00	0,00	0,00	0,00	0,00	0,00	0,00	0,00	0,00
Ca	0,86	0,82	0,48	0,89	0,84	0,83	0,87	0,89	0,88	0,77
Na	0,12	0,17	0,21	0,11	0,13	0,14	0,11	0,11	0,10	0,19
	5,94	5,98	6,18	5,97	5,98	5,99	5,98	5,97	5,99	5,99
Al total	0,62	0,68	1,09	0,64	0,54	0,61	0,61	0,59	0,59	0,57
Fe tot	0,19	0,15	0,08	0,15	0,19	0,14	0,13	0,15	0,16	0,16
Fe3+	0,06	0,02	0,00	0,03	0,02	0,01	0,02	0,03	0,01	0,01
Acm	0,06	0,02	0,00	0,03	0,02	0,01	0,02	0,03	0,01	0,01
Jd	0,06	0,15	0,21	0,08	0,12	0,13	0,09	0,07	0,09	0,18
Ti-Di	0,06	0,00	0,00	0,07	0,03	0,04	0,04	0,04	0,04	0,04
Jo	0,00	0,00	0,00	0,00	0,00	0,00	0,00	0,00	0,00	0,00
Ca-Tsc	0,55	0,54	0,23	0,59	0,62	0,59	0,60	0,61	0,61	0,57
En+Fs	0,05	0,02	0,12	0,02	0,03	0,03	0,02	0,02	0,03	0,04

* Based on Neumann(1976)

Table 5.4: *Composition of clinopyroxene1 and clinopyroxene2 from Hundkjeften*

Clinopyroxene														
Sample	HV11	HV11	HV11	HV11	HV11	HV11	HV11	HV11	HV11	HV11	HV5	ÅFS9	ÅFS9	ÅFS9
Analysis nr.	1/3.	3/3.	4/3.	5/3.	13/3.	17/3.	19/3.	20/3.	21/3.	23/3.	25/3.	7/4.	9/4.	10/4.
Mineral	Cpx1	Cpx1	Omph	Omph	Omph	Cpx1	Omph	Omph	Cpx1	Omph	Omph	Omph	Omph	Omph
[wt%]	wr	wr	wr	matrix	vein	wr	wr	wr	wr	clast	vein	incl	incl	matrix
SiO2	48,21	49,54	54,10	55,09	55,70	48,45	53,08	52,44	49,21	54,37	54,14	54,79	54,64	54,16
TiO2	1,09	1,16	0,32	0,23	0,06	1,35	0,44	1,09	1,54	0,03	0,13	0,22	0,10	0,21
Al2O3	12,06	11,63	11,88	13,06	11,02	11,43	13,82	12,33	11,99	11,58	12,95	10,05	12,01	11,23
Cr2O3	0,00	0,00	0,01	0,00	0,00	0,03	0,00	0,00	0,03	0,00	0,01	0,00	0,00	0,08
FeO	4,24	3,41	3,14	2,72	2,19	4,12	4,67	3,61	3,43	5,08	2,75	5,42	5,43	5,54
MnO	0,00	0,01	0,07	0,00	0,00	0,03	0,00	0,03	0,00	0,10	0,01	0,09	0,04	0,03
MgO	11,14	10,83	9,57	8,29	10,79	10,72	7,72	9,18	10,36	8,88	9,30	9,00	7,75	8,13
CaO	22,42	20,92	15,88	14,17	15,99	21,79	15,90	16,35	20,80	15,61	16,00	15,37	13,48	14,16
Na2O	1,91	2,62	5,60	6,51	5,60	2,16	5,43	5,37	2,87	5,60	5,70	5,96	6,87	6,22
K2O	0,01	0,01	0,03	0,02	0,01	0,01	0,01	0,00	0,13	0,02	0,01	0,01	0,02	0,01
Total	101,07	100,12	100,57	100,08	101,36	100,07	101,06	100,39	100,23	101,24	101,00	100,92	100,33	99,78
Mg/Mg+Fe	82,40	85,00	84,45	84,45	89,80	82,27	74,68	81,92	84,35	75,70	85,76	74,75	71,80	72,35
Structural formulae*														
Si	1,74	1,79	1,91	1,95	1,94	1,76	1,88	1,87	1,78	1,92	1,90	1,94	1,94	1,94
Al IV	0,26	0,21	0,09	0,05	0,06	0,24	0,12	0,13	0,22	0,08	0,10	0,06	0,06	0,06
Al VI	0,25	0,29	0,41	0,49	0,40	0,25	0,46	0,38	0,29	0,40	0,44	0,36	0,44	0,42
Ti	0,03	0,03	0,01	0,01	0,00	0,04	0,01	0,03	0,04	0,00	0,00	0,01	0,00	0,01
Cr	0,00	0,00	0,00	0,00	0,00	0,00	0,00	0,00	0,00	0,00	0,00	0,00	0,00	0,00
Fe3+	0,05	0,02	0,02	0,00	0,02	0,03	0,00	0,03	0,02	0,03	0,02	0,05	0,04	0,03
Fe2+	0,08	0,08	0,07	0,08	0,05	0,09	0,14	0,08	0,08	0,12	0,06	0,11	0,12	0,13
Mn	0,00	0,00	0,00	0,00	0,00	0,00	0,00	0,00	0,00	0,00	0,00	0,00	0,00	0,00
Mg	0,60	0,58	0,50	0,44	0,56	0,58	0,41	0,49	0,56	0,47	0,49	0,48	0,41	0,43
Ni	0,00	0,00	0,00	0,00	0,00	0,00	0,00	0,00	0,00	0,00	0,00	0,00	0,00	0,00
Ca	0,86	0,81	0,60	0,54	0,60	0,85	0,60	0,62	0,81	0,59	0,60	0,58	0,51	0,54
Na	0,13	0,18	0,38	0,45	0,38	0,15	0,37	0,37	0,20	0,38	0,39	0,41	0,47	0,43
	5,95	5,98	5,98	6,00	5,98	5,97	6,00	5,97	5,98	5,97	5,98	5,95	5,96	5,97
Al total	0,51	0,50	0,49	0,54	0,45	0,49	0,58	0,52	0,51	0,48	0,54	0,42	0,50	0,47
Fe tot	0,13	0,10	0,09	0,08	0,06	0,13	0,14	0,11	0,10	0,15	0,08	0,16	0,16	0,17
Fe3+	0,05	0,02	0,02	0,00	0,02	0,03	0,00	0,03	0,02	0,03	0,02	0,05	0,04	0,03
Acm	0,05	0,02	0,02	0,00	0,02	0,03	0,00	0,03	0,02	0,03	0,02	0,05	0,04	0,03
Jd	0,09	0,16	0,36	0,45	0,36	0,12	0,37	0,34	0,18	0,36	0,37	0,36	0,43	0,40
Ti-Di	0,03	0,03	0,01	0,01	0,00	0,04	0,01	0,03	0,04	0,00	0,00	0,01	0,00	0,01
Jo	0,00	0,00	0,00	0,00	0,00	0,00	0,00	0,00	0,00	0,00	0,00	0,00	0,00	0,00
Ca-Tsc	0,21	0,15	0,07	0,04	0,05	0,16	0,09	0,08	0,14	0,08	0,09	0,05	0,06	0,05
Di+Hd	0,63	0,63	0,52	0,49	0,54	0,65	0,50	0,52	0,63	0,51	0,51	0,53	0,45	0,49
En+Fs	0,03	0,02	0,03	0,01	0,03	0,01	0,02	0,02	0,01	0,04	0,02	0,03	0,04	0,04

*Based on Neumann(1976)

Table 5.5: *Clinopyroxene1 and omphacite analyses from Husebøvatnet and Ådnefjell.*

This page intentionally left blank

Chapter 6

Determination of Paleostress

6.1 Theoretical Background

The magnitude of the dynamic shear stress during coseismic slip τ_f determines the amount of coseismic dynamic stress drop (Scholz, 1990). The stress estimates in this thesis will be determined using the energy balance of faulting. The reason for this is that the amount of pst preserved on the fault planes yield information on what the energy released during faulting must have been to be able to melt the given amount of melt. If multiple events occurs on the same fault, the amount of heat may be less due to lower stress required for faulting, due to less cohesion (Eq. (1.2) in Section 1.2.4 in Chapter 1).

Following Scholz (1990), a general energy balance for faulting can be written

$$W_f = Q + E_s + U_s + W_g, \tag{6.1}$$

where W_f is mechanical work done in faulting (including both friction and ductile deformation), Q is the heat, U_s is surface energy (found to be negligible for faulting), E_s is the energy radiated in earthquakes, and W_g is the work against the gravity.

Experiments and seismological studies have shown that E_s is negligible compared with the total energy released (<6%). Also U_s can be considered negligible with respect to the work done by friction. If work against gravity is neglected, e.g. , in strike-slip settings where $W_g \sim 0$, almost all mechanical work done during deformation must be converted into heat (Scholz, 1990). This reduces Eq. (6.1) to

$$W_f \approx Q, \tag{6.2}$$

The heat generated during faulting result in the rock heating and melting. Di Toro et al. (2005) use the following equations to determine the dynamic shear stress during faulting, τ_f. Total energy E_m per unit mass [J kg^{-1}] can be partitioned as:

1. energy exchanged for rock heating until melting, $c_p(T_m - T_{hr})$
2. energy exchanged during melting of the rock, H, and
3. energy required for further heating of the melt, $c_p(T_i - T_m)$, in the case of superheated melt.

Thus,

$$E_m = c_p(T_m - T_{hr}) + H + c_p(T_i - T_m), \tag{6.3}$$

where T_m is the rock melting temperature, T_{hr} is the temperature of the ambient host rock, T_i is the initial melt temperature, H is latent heat of fusion, c_p is the specific heat of the rock at constant pressure, and c_{pm} is the specific heat of the melt. Survivor clasts of the wall-rock does not exchange

heat of fusion, and hence the relative amount of clasts in the pst needs to be accounted for. The third term in Eq. (6.3) must therefor be split into two terms; one considering the melt and one considering the clasts. If $\phi = (V_{clast}/V_{pst})$, where V_{clast} is the volume of clasts and V_{pst} is the total volume of pst (*i.e.*, matrix+clasts), then from Eq. 6.3:

$$E_m = c_p(T_m - T_{hr}) + (1-\phi)H + (1-\phi\ c_{pm}(T_i - T_m) + \phi\ c_p(T_i - T_m),$$

and assumed that $c_{pm}(T) \approx c_p(T)$, all $c_{pm}(T)$ can be replaced by $c_p(T)$, which gives

$$E_m = (1-\phi)H + c_p(T_i - T_{hr}). \tag{6.4}$$

since E_m is energy per unit mass, the energy input E [J] is

$$E = E_m \rho A t, \tag{6.5}$$

where

$$\rho A t = mass,$$

and where ρ is the density, A is the area of the fault surface, and t is the average thickness of the friction-induced melt along the fault plane. From inserting Eq. (6.4) into Eq.(6.5),

$$E = \rho A t(1-\phi)H + c_p(T_i - T_{hr})\rho A t. \tag{6.6}$$

The work for unit area [J m^{-2}] done to overcome the frictional sliding resistance for a constant τ_f is

$$W_f = d\tau_f,$$

where d is the fault displacement. Considering W_f is converted to heat E, for the area of the fault surface where frictional work occurs:

$$d\tau_f = \frac{E}{A}.$$

Inserting the expression for E from Eq. (6.5),

$$d\tau_f = \frac{E_m \rho A t}{A} = E_m \rho t,$$

so that

$$\tau_f = \frac{E_m \rho t}{d}.$$

Inserting the expression for E_m from Eq. (6.4):

$$\tau_f = \rho[(1-\phi)H + c_p(T_i - T_{hr})]t/d \tag{6.7}$$

This is the equation Di Toro et al. (2005) used for their calculation of the dynamic shear stress, and will also be used for the stress estimates in this thesis.

The parameters H, c_p, and ρ can be calculated or found in the literature, and from field and microstructural observations ϕ, T_i, t, and d can be determined. If the ambient conditions for faulting T_{hr} are known, τ_f can be estimated.

6.2 Parameters used for Estimates

The density ρ of anorthositic to gabbroic granulites from the Hundkjeften area was measured by Kuhn (2002), from the weight of drill cores in air and in water. The typical value lie around $\sim 3.0 g/cm^3$, consistent with previous values obtained by Austrheim and Griffin (1987).

The relative amount of clasts $\phi = (V_{clast}/V_{pst})$ vary from fault to fault. What we can observe from microstructural studies is really the area of clasts relative to the area of the pst. Two methods have been used to find a value for the amount of clasts;

1. Image processing and analysis on micrograph. This approach was used for the fault at Hundkjeften only.
2. Estimated from thin sections. The amount of clasts relative to the total amount of pst was estimated from the number of thin sections available from each fault ($n = 1 - 3$).

The values used for each fault is found in Tab. 6.1.

The latent heat of fusion H for the wall-rock is $\sim$377 kJkg^{-1}. This value was determined by Warren (1986) for lunar anorthosite.

The heat capacity C_p of the wall-rock is $\sim$1.1 kJkg^{-1}K^{-1}. This value was determined by Warren (1986) for anorthosite.

The initial melt temperature T_i is based on the nominal melting curve of plagioclase, which is the dominating mineral in the rocks. In the solid solution diagram of the An-Ab system, for dry rocks with composition $\sim$An$_{50}$, the first melt will be produced when heated to 1275°C (intersection with solidus).

The ambient host rock temperature, T_{hr}, is determined based on the mineral-assemblages of the pst and the regional metamorphism during faulting. Their mineralogy is assumed to represent the P-and T-space of quenching, which occurred in both eclogite facies and amphibolite facies. These two metamorphic events are carefully studied by numerous workers, and *i.e.* Kuhn (2002) give temperature estimates of 750°C for the eclogite facies metamorphism, and 625°C for the retrograde amphibolite facies metamorphism. These will be the values used for the stress estimates. The value of T_{hr} used for the different faults is found in Tab. 6.1.

However, using the temperature estimate for the retrograde amphibolite facies metamorphism is really only viable if we knew that the faulting occurred during eduction and retrograde metamorphism. If the faulting occurred during subduction during prograde metamorphism towards eclogite facies conditions, 625°C will be a maximum temperature. Therefor, the temperature increase from T_{hr} to T_i could have been more than what used in these estimates, and hence the dynamic shear stress during faulting could have been much greater.

The thickness, t, of the pst is estimated by using three different methods, depending on the information available for the different faults.

1. For fault HK, mapped in detail, the map was used to measure the total area of pst, including injection veins, rip-out structures and fragments of pst found in the adjacent wall-rock, in addition to the pst present along the main fault vein.
2. For the rest of the faults the thickness is estimated based on investigation of the thin sections available from each fault ($n = 1 - 3$).

For thicknesses estimated based on thin section observations, no correction for the dip of fault plane is needed, because the drill cores were cut perpendicular to the fault plane.

The true displacement can not be measures directly in the field due to lack of piercing point. The apparent displacement d is therefor the best approximation, even though this is always a minimum estimate. The presence of a marker enable this value to be measured.

Fault	ρ [kgm^{-3}]	ϕ	H [kJkg^{-1}]	Cp [kJkg^{-1}K^{-1}]	T_i [°C]	T_{hr} [°C]	t [m]	d[m]
HK	3000	0.17	377	1.1	1275	625	0.0044	0.62
Hva	3000	0.36	377	1.1	1275	625	0.0016	0.095
HVb	3000	0.71	377	1.1	1275	750	0.0037	0.052
HVc	3000	0.02	377	1.1	1275	750	0.002	0.16
ÅFSa	3000	0.85	377	1.1	1275	n.d.	0.001	0.055
ÅFSc	3000	n.d	377	1.1	1275	750	n.d	n.d
ÅFSd	3000	0.70	377	1.1	1275	625	0.007	0.125

Table 6.1: *The values of the parameters used for stress estimates for the different faults*

6.3 Uncertainties

To estimate the dynamic shear stress during coseismic slip τ_f is rather straight forward in theory. Although, there are several uncertainties regarding the parameters used in the estimates.

The thickness of the vein t is a value that give rise to several difficulties. If the fault plane is shallow-dipping, and the outcrop is nearly horizontal, the thickness is overestimated if not corrected for the dip. The thickness of pst vary along strike of the fault, so unless the whole fault is uncovered, it is necessary to choose the most representative section for calculating the area per unit length. Along fault it is common to find pst-free segments, because pst is likely produced heterogeneously along the fault and redistributed by flow to fill dilational domains, both on fault plane and in adjacent host rock. Consequently, t is often overestimated, which in turn contribute to an overestimate of τ_f (Di Toro et al., 2005). Sometimes it might be difficult to distinguishing between pst and wall-rock in the field. This is an especially relevant problem in case of rain, which makes the outcrop appear darker, and the wall-rock less distinct from the dark gray pst. Inaccuracy during measurements and mapping may also occur. When measuring the thickness from thin section, it is also important to choose the most representative value of t.

The melt drained away from the fault plane and into injection veins may account for a significant part of the total produced melt, but is often not included in the total melt volume. This is also a clear limitation of estimating amount of melt from thin sections. Detailed mapping of fault HK reveal that 25% of the melt measured in the field are observed away from the main fault plane, i.e. , as injection veins, sidewall ripouts and fragments in the wall-rock.

The field-measured, apparent displacement d also involves uncertainties because the pst is often associated with cataclasites. If cataclasis was a precursor to the seismic rupture, two possible scenarios arise; If cataclasis was the result of the incremental deformation products of a continuous short-lived coseismic episode, the measured d may be directly used in Eq.(6.7). In case of a longlived phase of fault creep prior to earthquake rupture, d would be composite, including a cataclastic component that does not contribute to melting. This leads to an overestimate of d, which in turn gives an underestimate of τ_f. There is a general problem that slip can not be separated in aseismic and seismic components (Di Toro et al., 2005).

The ambient host rock temperature, T_{hr}, assumes the faulting occurred at the same conditions as the recorded metamorphic events; at 750°C for eclogite facies, and at maximum 625°C for amphibolite facies. This is based on the mineral assemblages of the pst. For amphibolite facies pst the

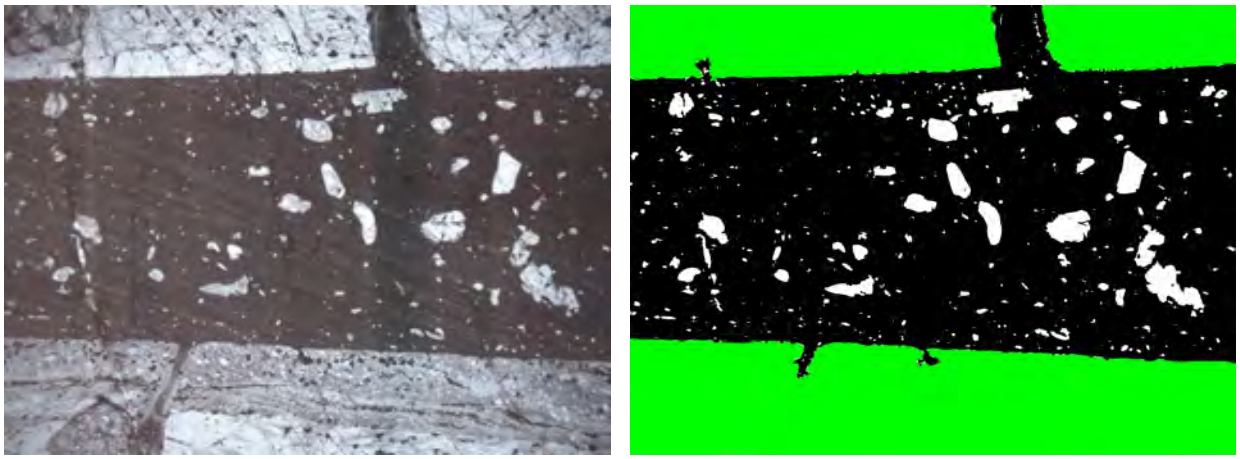

(a) Original micrograph (HK4, ppl) *(b) Processed image(HK4)*

Figure 6.1: *Micrograph from thin section from fault HK and processed image to estimate ϕ.*

temperature corresponds to the retrograde path. It is a possibility that the faulting occurred during subduction, and/or on a shallower level than what the maximum amphibolite facies temperature corresponds to. In such a case, the temperature rise required for melting would increase, and the estimated average shear stress during faulting, τ_f, would be higher.

The initial melting temperature T_i may be overestimated because the nominal melting curve of plagioclase is used. The melting temperature of rocks is lowered when more than one mineral is present. Also, H_2O-saturated rocks will have lower melting temperature than dry. The estimates in this thesis do not consider the H_2O-saturation, as they are calculated for dry anorthosites. However, a temperature of 1350-1400°C was suggested for melting of garnets of such compositions as at norther Holsnøy (Deer in (Austrheim et al., 1996)). This suggest the temperature chosen to use in the estimates is relatively modest.

The relative amount of clasts ϕ is only in one case determined using image processing and analysis. If these were applied to all the faults, the error margin would have been lower.

6.4 Results of Stress Estimates

Eq. (6.7), outlined in Section 6.1,

$$\tau_f = \rho[(1-\phi)H + c_p(T_i - T_{hr})]t/d,$$

is used to estimate the average dynamic shear stress during faulting for six faults at northern Holsnøy.

Fault HK Relative amount of clasts ϕ is determined by imaging of one micrograph, from thin section HK4, which is considered representative for the thin sections.

Color	black (matrix)	white (clasts)	phi
Nr. pixels	7787287	1554759	0,17

Table 6.2: *Calulating ϕ from nr.of pixels in Fig 6.1b*

Thickness t is determined by using the area method on the detailed map of this fault, Fig 3.5. The total area of melt measured is divided on the length of the fault to find the average thickness of

pst preserved on the fault plane. Injection veins, sidewall ripouts and fragments of pst in nearby wall-rock is included.

The apparent displacement is measured in the horizontal plane in the field. The maximum ambient host rock temperature is set to 625°C based on the amphibolite facies mineral assemblage observed in the pst. These values yield an estimate of the minimum average shear stress during faulting, τ_f, of 21,88 MPa, see Tab. 6.3.

Fault	ϕ	T_i [°C]	T_{hr} [°C]	t [m]	d [m]	τ_f [MPa]
HK	0,17	1275	625	0,0044	0,62	21,88

Table 6.3: *Minimum dynamic shear stress estimate for fault HK.*

Fault HVa Relative amount of clasts ϕ and thickness t determined by examination of three thin sections; HV2, HV3 and HV4, see Tab. 6.4 and scan of thin sections HV2 and HV4 in Appendix. The maximum ambient host rock temperature is set to 625°C based on the amphibolite facies mineral assemblage observed in the pst. The apparent displacement d is measured directly on the sub-horizontal outcrop. These values yield an estimate of the average shear stress during faulting, τ_f, of 50,33 MPa, see Tab. 6.5.

Fault	Thin section	t [mm]	ϕ
Hva	HV2	1	0,15
	HV3	3	0,9
	HV4	1	0,02
	Mean	1,6	0,36

Table 6.4: *t and ϕ of pst at HVa*

Fault	ϕ	T_i [°C]	T_{hr} [°C]	t [m]	d [m]	τ_f [MPa]
HVa	0,36	1275	625	0,00166	0,095	50,33

Table 6.5: *Dynamic shear stress estimate for fault HVa.*

Fault HVb Relative amount of clasts ϕ and thickness t determined by examination of three thin sections; HV5, HV6 and HV7, see Tab. 6.6, and Appendix for scan of thin section HV6. A difficulty concerning the value of ϕ arise when examining thin sections HV6 and HV7. Unlike HV5, they show some features indicative of pst, and other features indicative of mylonite, see Section 4.2.3. The mylonite could be a secondary texture after pst or cataclasis. This makes it unclear whether the pale colored matrix material in the fault vein, referred to as Type 2 pst, was ever molten, and thus it is considered not in this case. There is, however, a clear border between the wall-rock and the fault vein, therefor the value of ϕ is close to 1 and equals 1, see Tab. 6.6.

The ambient host rock temperature is set to 750°C based on the eclogite facies mineral assemblage observed in the pst. The apparent displacement d is measured directly on the sub-horizontal outcrop. These values for the parameters yield an estimate of the average shear stress during faulting, τ_f, of 146,61 MPa, see Tab. 6.7.

Fault	Thin section	t [mm]	ϕ
HVb	HV5	4	0,25
	HV6	4	1
	HV7	3	0,9
	Mean	3,7	0,71

Table 6.6: *Average values for thickness of pst and ϕ of fault HVb*

Fault	ϕ	T_i [°C]	T_{hr} [°C]	t [m]	d [m]	τ_f [MPa]
HVb	0,71	1275	750	0,0037	0,052	146,61

Table 6.7: *Dynamic shear stress estimate for fault HVb.*

Fault HVc Relative amount of clasts ϕ and thickness t determined by examination of the one thin sections available from this fault ; HV11, see Appendix for scan of thin section. The apparent displacement d is measured from field photo in Fig. 3.12b. The ambient host rock temperature is set to 750°C based on the eclogite facies mineral assemblage observed in the pst. These values yield an estimate of the average shear stress during faulting, τ_f, of 35,51 MPa, see Tab. 6.8.

Fault	ϕ	T_i [°C]	T_{hr} [°C]	t [m]	d [m]	τ_f [MPa]
HVc	0,02	1275	750	0,002	0,16	35,511

Table 6.8: *Dynamic shear stress estimate for fault HVc.*

ÅFSa Relative amount of clasts ϕ and thickness t determined by examination of the one thin sections available from this fault; ÅFS2, see Appendix for scan of thin section. The problem regarding whether parts of the fault veins has ever been molten arises also in this case, see Section 4.3.3. The fault vein have sharp boundaries to the wall-rock, but most of the material is pale gray in ppl in the optical microscope. This is referred to as Type 3 pst, and it is uncertain if this parts of the vein was molten, or only underwent severe cataclasis. In the estimates it is therefore considered not having been molten, and thus the value of ϕ is high.

The mineral assemblage of thin sections ÅFS2 was not checked in the EMP, and the ambient conditions of faulting and coseismic slip is therefore not determined. To avoid an overestimate, the temperature requiring the least temperature increase, 750°C (eclogite facies conditions), is used, see $*$. The apparent displacement d is measured directly on the outcrop. These values yield an estimate of the average shear stress during faulting, τ_f, of 34,58 MPa, see Tab. 6.9.

Fault	ϕ	T_i [°C]	T_{hr} [°C]	t [m]	d [m]	τ_f [MPa]
ÅFSa	0,85	1275	750$*$	0,001	0,055	34,58

Table 6.9: *Dynamic shear stress estimate for fault ÅFSa.*

ÅFSd Relative amount of clasts ϕ and thickness t determined by examination of the one thin sections available from this fault; ÅFS10, see Appendix for scan of thin section. The apparent displacement d is measured directly on the outcrop. The ambient host rock temperature is set to 625°C based on the amphibolte facies mineral assemblage observed in the pst. These values yield an estimate of the minimum average shear stress during faulting, τ_f, of 139,12 MPa, see Tab. 6.10.

Fault	ϕ	T_i [°C]	T_{hr} [°C]	t [m]	d [m]	τ_f [MPa]
ÅFSd	0,70	1275	625	0,007	0,125	139,12

Table 6.10: *Minimum dynamic shear stress estimate for fault ÅFSd.*

Tab. 6.11 gives an overview of the mineral assemblage of the pst, the displacement and the dynamic shear stress estimates calculated for he six fault.

	Amphibolite facies pst			Eclogite facies pst		Not det.
Fault	HK	Hva	ÅFSd	HVb	HVc	ÅFSa
d [m]	0.62	0.095	0.125	0.052	0.16	0.055
τ_f [MPa]	21,88	50,33	139,12	146,61	35,51	34,58

Table 6.11: *d and τ_f for all faults. Not det. = mineral assemblage of the pst is not determined.*

This page intentionally left blank

Chapter 7

Discussion

Deep earthquakes, often associated with tremors, are reported from lower crustal levels and Moho-depths (Chen et al., 2012). Pst have been reported from several exhumed high grade metamorphic terranes, like fossil subduction zones, the latest decades (Andersen and Austrheim, 2006; Austrheim and Andersen, 2004; Austrheim and Boundy, 1994; John and Schenk, 2006). Pst at Holsnøy is intimately associated with granulite, eclogite and, locally, amphibolite. These high grade metamorphic rocks were subducted and partly metamorphosed during the Caledonian orogeny.

The spatial relationship between the high grade metamorphic rocks and the pst give reason to ask if the pst at Holsnøy are formed at depth and represent paleo-earthquakes analoge to those released at mantle depth below Himalaya today.

7.1 Depth of faulting

EMP analyses of six faults reveal that two different mineral assemblages are present in the pst veins; an eclogite facies assemblage and an amphibolite facies assemblage. The pst that have an eclogite facies mineralogy could be either

1. prograde, formed during subduction, while the rock resided in the brittle regime, and later recrystallized at eclogite facies conditions, or
2. formed at depths of eclogite facies conditions, at relatively high temperature and high pressures (here; 650-750°C and 15-21 kbar (Glodny et al., 2008; Jamtveit et al., 1990))

Austrheim and Boundy (1994) and Austrheim et al. (1996) report euhedral to dendrittic garnets in pst with inclusions of eclogite facies minerals, and eclogite facies minerals filling fractures in garnet adjacent to pst. The authors interpreted this as evidence of the pst having formed at eclogite facies conditions. The present work include observations of the similar textures; newly grown garnets with inclusions of eclogite facies minerals, and omphacite grown in fractures in wall-rock garnets adjacent to pst.

The observation of some of the pst having an amphibolite facies mineralogy imply that faulting producing pst occured over a wider range of metamorphic conditions, and thus depths, than previously reported from northern Holsnøy. Three different possibilites of relative timing and depth of the amphibolite facies pst veins in relation to the eclogite facies deformation and metamorphism follows:

1. prograde, faulting occurring while the rocks were subducted towards eclogite facies depths. In this case the pst have survived burial to greater depths and the following exhumation.
2. faulting ocurred at eclogite facies conditions, and the pst recrystallized to an amphibolite facies assmblage at amphibolite facies conditions during exhumation. Observations of microtextures like spherulites, interpreted to have quenched from a melt, contradicts this. Also, the clasts have a tendence to a preferred orientaton sub-parallel to the strike of the pst fault vein, that could be result of flow in the pst-melt. Flow structures are observed from several pst.
3. retrograde, faulted during exhumation. The amphibolite facies metamorphism on the retrograde path of the subducted rocks is constrained to maximum 600-690°C and 8-12 kbar (Bingen et al., 2004; Glodny et al., 2008; Kuhn, 2002), corresponding to depths of ∼30km. In this case the granulite would already be partly altered to eclogite, which have a weaker rheology compared to the granulite (Austrheim et al., 1997; Jolivet et al., 2005). One would therefor expect deformation to localize in zones of weakness, hence, in the eclogites, but this is not the case at Holsnøy, as the pst is mostly observed in the dry granulite.

Faulting may have occured on shallower levels than what inferred from the retrograde path of amphibiolite facies metamorphism, for which the maximum temperatur is constrained. Fig. 7.1 show a conseptual sketch of burial and exhumation during continental subduction, modified from Jolivet et al. (2005). White stars indicate the possible depth range of paleo-earthquakes in the Lindås nappe, from ∼60-70 km for the eclogite facies pst and up to ∼30 km for the amphibolite facies pst.

However, almandine-rich garnet (grt2), interpreted as having grown from the melt, is observed in the amphibolite facies pst at fault HK at Hundkjeften. The garnet show a crystal growth resulting in an irregular morphology, with poorly developed crystal faces. The newly grown garnets are associated with plagioclase, and not omphacite as in the eclogite facies pst.

The matrix of pst at fault HVb at Husebøvatnet mainly consist of an eclogite facies mineral assemblage. However, minor pockets of pst with an amphiboite facies assemblage are observed along the same fault, associated with pst type 2, see Section 4.2.3, Chapter 4. The various appearances of pst will be discussed in the following section.

7.2 The variable appearance of pst

Since the amount of melt preserved on the fault planes must be determined in order to estimate the average dynamic shear stress during faulting based on the energy budget, like done in Chapter 6, the appearance and possible origin of the observed fault rocks will be discussed.

Most pst-veins described from Hundkjeften, Husebøvatnet and Ådnefjell in Chapter 4 have a dark colored and a very fine-grained matrix, and sharp boundaries to wall-rock or wrdz. They contain clasts, that are angular to thermally rounded, and newly grown grains of garnet. In the petrographic descriptions this is referred to as only *pst*, or *type 1 pst*. The faults HK, HVa, HVc, ÅFSc and ÅFSd have type 1 pst.

The pst at the faults HVb and ÅFSa differ from those previously described. At fault HVb, both type 1 pst and what is referred to as type 2 pst in Chapter 4, Section 4.2.3 are observed. This type of pst has a pale gray color, and a foliation of alternating dark an white to pale gray layers wrapped around plagioclase clasts. The clasts is mostly rounded, but angular fragments are observed. Folding of the foliation is observed, a sheet fold is shown in Fig 4.12d as an example. The Type 2 pst show some fabric elements characteristic for mylonites; porphyroclasts and foliation (Passchier and Trouw, 2005). Mylonites do, however, typically show a gradational contact to the wall-rock

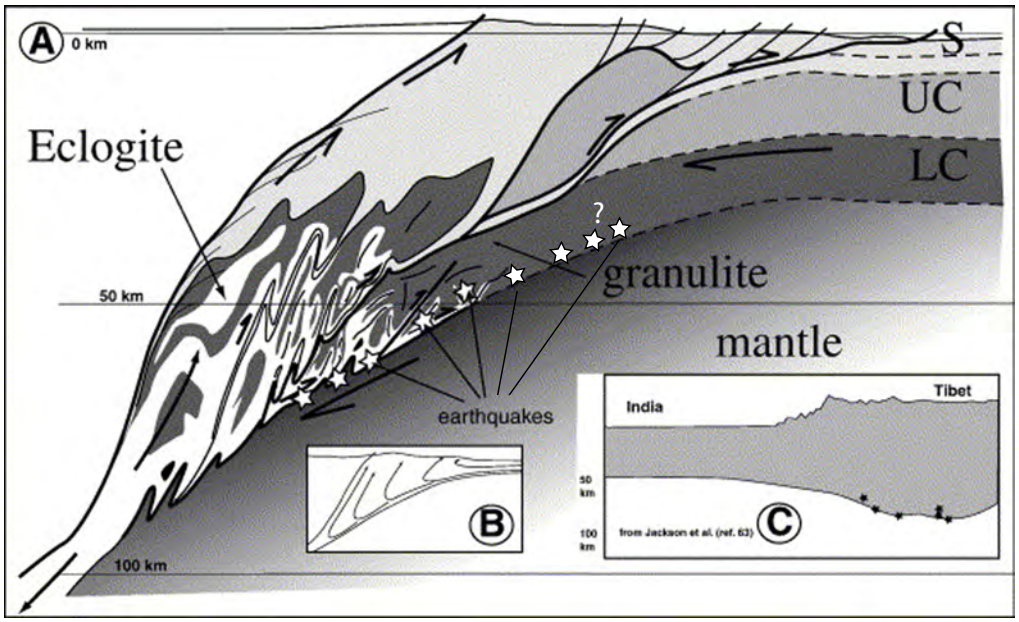

Figure 7.1: *A:Synthetic conseptual model of burial and exhumation during continental subduction. B: Schematic trajectories of particles within the subduction channel. C: Deep earthquakes below the Himalayas (Jolivet et al., 2005). White stars indicate earthquakes in the lower crust, that possibly occurred at a wide range of depths in the case of Holsnøy, from ∼30 km and down to ∼70 km. Figure modified from Jolivet et al. (2005).*

(Passchier, 1982), which is not observed at fault HVb. The rounded clasts may have attained their shape during mylonitization, or they can have been thermally rounded in a melt.

The following scenarios may have resulted in the fault rock observed, referred to as type 2 pst:

1. A type 1 pst reactivated as a mylonite. The foliation can in this case be result of compositional banding in pst or by ductile deformation during mylonitization. Type 1 pst at the same fault plane show no sign of reactivation.

2. A cataclasite reactivated as a mylonite. In this case the material have not been through a melt phase, and the foliation, folds and rounded clasts are results of mylonitization. Since not all clasts are rounded, as observed in Fig 4.12d, this alternative seems less likely.

3. A type 1 pst extensively recrystallized. The foliation must in this case represent a compositional layering, and the folds result from fluid flow. The clasts must have been thermally rounded.

The detailed map of fault HVb in Fig 3.10 show that the geometry of the pst alternates between a single fault vein and a double slip zone that enclose lenticular fragments of wall-rock. Injection veins, concidered a common characteristic of pst (Passchier, 1982), are, however, not observed. This could indicated that limited amounts of melt was produced along this fault. Passchier (1982) describes ultramylonite bands developed from pst bands, with flattened and ductily deformed microtextures like spherulites. This is however not observed from HVb.

At fault ÅFSa both type 1 pst and type 3 pst are observed. The type 3 pst, described in Chapter 4, Section 4.3.3, has a pale gray color in ppl, and angular clasts up to the width of the fault vein. No foliation or flow structures are observed. Corroded garnet in wall-rock suggests a melt event. Although, when considering the boundaries between type 1 and type 3 pst, it appears as that of type 1 pst and thermally rounded clast, with type 1 pst making embayments into the type 3 pst. This may indicate that the type 3 pst have not beeen through a melt phase.

Considering that there are heterogeneities in the stress state along faults (Kanamori, 2008), and that it is commen to find pst-free segments along fault (Di Toro et al., 2005), it may not be surprising that the fault rocks would vary along fault. Since the observations are not unambiguous, no conclusions regarding the apperance of pst will be drawn. In the estimate of the average dynamic shear stress during faulting in Chapter 6, the type 2 and 3 pst is therefore considered as not having been molten. This is done in order to avoid an overestimate of melt produced on the fault.

7.3 Stress drop estimates/dynamic shear resistance

Uncertainties regarding the parameters used in the stress estimates have been discussed in Chapter 6, Section 6.3. This section will focus on evaluating the results from the stress estimates.

The estimated average τ_f are found to vary considerably, the lowest value is 21,88 MPa (fault HK) and the highest is 146,61 MPa (fault HVb). This immediately rise the question of what makes them so variable. Do the difference in τ_f show any relation to the depth of faulting, or to displacement?

The temperature of the ambient host rock, T_{hr}, used in the estimates, is determined based on the mineral assemblage of the pst. It is therefore assumed that the faulting resulting in amphibolite facies pst occurred on a shallower level than the faulting resulting in eclogite facies pst. For amphibolite facies pst τ_f varies from 21,88 MPa to 139,12 MPa, see Tab. 6.11. This is a difference in τ_f of 117,24 MPa. For eclogite facies pst τ_f varies from 35,51 MPa to 146,61 MPa, see Tab. 6.11, which is a difference in τ_f of 111,1 MPa. The large span of estimated τ_f can thus not be explained by the depth of faulting.

Di Toro et al. (2005) estimated the average shear stress of 63 exhumed faults from the paleoseismic Gole Larghe Fault Zone, using Eq. (6.7), and observed a decrease in τ_f with d. Fig. 7.2a show their plot of τ_f versus d. In Fig. 7.2b the estimated values of the average dynamic shear stress for the six studied faults at Holsnøy is plotted against the displacement. Both low and high shear stresses were obtained for fault with small displacements, while a low shear stress was obtained for the fault with the largest displacement. Despite the low number of faults, and the different values of the axis, the same trend is observed as in the plot of Di Toro et al. (2005).

7.4 Evaluation of possible mechanisms causing intermediate deep earthquakes

In Chapter 1 the two main hypothesis for explain intermediate deep earthquakes, dehydration embrittlement and shear heating, were reviewed. Understanding the mechanism by which rocks fail by brittle faulting under high confining pressure is one of the overall goals of the numerous studies previously carried out on exhumed pst-bearing fault complexes *i.a.*, by Andersen and Austrheim (2006) and John et al. (2009). Thus, this section will evaluate the observations that may point to one of those more likely than the other.

For the possibility of an increase in pore pressure and a dehydration embrittlement to occur, a hydrous or volatile phase must be present in the rocks. The pst at Holsnøy are associated with relatively dry granulite facies rocks. Only minor amounts of amphibole are locally observed in the wall-rock, like illustrated in Fig. 4.1a in Chapter 4. Another phase that can possibly undergo dehydration is scapolite, that are also observed in relatively small amounts throughout the granulites. This mineral has a volatile component that could possibly be released to give a dehydration embrittlement. Observation of a 1 cm thick vein of scapolite at the locality at Hundkjeften suggest that this mineral locally might occur in larger amounts than first at appearance. Although, as illustrated

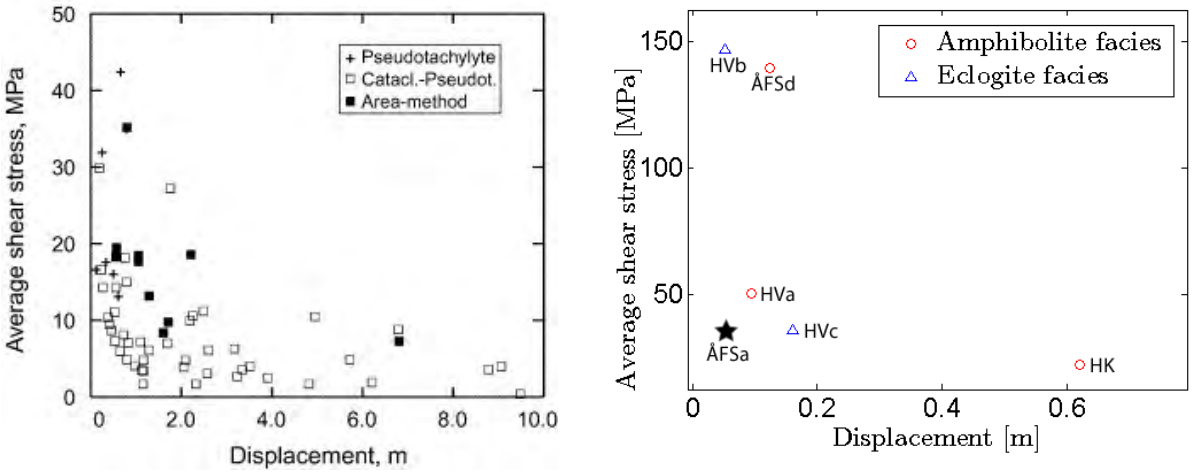

(a) 63 faults from the exhumed Gole Larghe Fault Zone. From Di Toro et al. (2005).

(b) Six faults from Holsnøy. The minaral assemblage of pst of fault ÅFSa is not determined, it is here plotted as a black star

Figure 7.2: *The average dynamic shear stress during faulting plotted against the displacement according to Eq.* (6.7)*. Note the difference in values on the axes from (a) to (b).*

in the detailed map of fault HK, Fig. 3.5, the scapolite vein does not show a spatial correlation with fault HK. It is, however, offset by another network of pst.

If shear heating resulting in self-localizing thermal runaway was the mechanism responisble for generation of the earthquake, the precurser of faulting was ductile. Petrographic observations of the interface between wall-rock and pst, and of the wall-rock damage zones of the pst may give information on, or indications of, the pre-seismic behaviour of the rock.

The pst on Holnsøy always have a sharp contact to the adjacent rock, regardless of this being a coarse-grained wall-rock or a fine-grained wall-rock damage zone (wrdz). This is described in Chapter 4. The term wrdz implies that the wall-rock is damaged; meaning it has experienced severe deformation, and appear different from what it originally did. What is *not* implied in the term is how or when this deformation occurred.

The wrdz are mostly observed as a transition between pst and wall-rock, but where the geometry of the pst is a generation zone with double slip planes, a wrdz is locally observed in between pst-layers, like in Fig. 4.12b. Regarding the relative timing of generation of pst verus generation of the wrdz,the wrdz can be seen as a precursor to the pst melting event, or as a result of the pst damaging the surrounding wall-rock. In the case of fault HK, petrographic observations may constrain this. Fig. 4.5b show an injection vein of pst truncating the wrdz and wall-rock. In this case the wrdz clearly was present at the time of melting. Injection veins into the wrdz are also shown in Fig. 4.5f.

The wrdz are typically cataclastic, with mostly angular, but also subrounded fragments, like in Fig. 4.4d. Fig. 4.5f show fractured plagioclase in a matrix that, as shown in Fig. 4.6e, consist of angular to subrounded fragments. Other places signs of ductile deformation is evident in the wrdz, like larger plagioclase grains with undulose extinction, that reveal they are bent towards the fault plane. In Fig. 4.4b the plagioclase grain embedded in a finer grained matrix is an example of this.

However, the presence of a wrdz, regardless of indications or evidence of brittle of ductile deformation, may in it self be conflicting with the shear heating and SLTR as proposed mechansim. The numerical simulations by John et al. (2009) show that the thickness of the pertubated and ductilly deforming zone, is much narrower than the thickness of the reulting melted material. Their petrographical observations also report a sharp contact between the pst and wall-rock. Such intrusive-like contacts

are also observed several places along the studied faults at Holsnøy, like Fig. 4.2, 4.5c and 4.5d are examples of. Although, the intrusive-like contact is only present along parts of the fault, and often only on one side of the pst. The field observations do not reveal any transition from shear zone to pst along the same deformation surface.

The observations are not comprehensive and clear enough to consider one hypothesis more likely than the other. Also, the faults that have amphibolite facies pst could possibly have been generated at much shallower depths than the eclogite facies pst-bearing faults. Their occurrence may need no mechanism other than the regular stick-slip as for shallow earthquakes.

7.5 Large scale implications of faulting at depth

The pst at Holsnøy are found in granulites adjacent to eclogite facies shear zones and breccias. Austrheim et al. (1997) suggested that the paleo-seismic faulting represented by the pst initiated the fluid infiltration and eclogitization. The authors also pointed to the weakening of the rock caused by this metamorphism. Jolivet et al. (2005) developed this idea, and suggested that the deformation and eclogitization lower the resistance of rocks, causing localization in shear zones. This lead to decoupeling of buoyant tectonic units from the subducting slab, and a possibility for these units to be incorporated in the subduction channel circulation and eventually being exhumed.

Deep lithospheric earthqakes also give information on the relative strength of mantle and crust. The estimated dynamic stress drops give qualitative information on what shear stresses the crust can be capable of storing before it is released in earthquakes. Labrousse et al. (2010) compared the observed seismicity, strength loss and delayed density increase of the lower Indian crust to the observation of pst and partly eclogitized rocks at Holsnøy. They argue that the similar size and structure of the two orogens emphazise the importance of eclogitization at depth, both as a way to weaken the lower crust and for decoupling of crustal material from lithospheric mantel in collision zones.

Given that the metamophic transitions at depth are suggested to control delamination preocesses and exhumation, the initial faulting of deep crust have severe geodynamic implications. Understanding the mechanism by which faulting is initiated at such depths are still an open question.

Chapter 8

Conclusion

From the observations made and the results given in this thesis, the following can be concluded:

1. Amphibolite facies pst are observed at northern Holsnøy. This suggests that the seismic faulting occurred at a wider range of depths than previously reported from this area.
2. For the amphibolite facies pst, there might not be need for a mechanism other than that of shallow earthquake to explain their occurrence.
3. The estimates of shear stress resistance give highly variable values of the average shear stresses during faulting. The lowest value is 21,88 MPa and the highest is 146,61 MPa.
4. The large span of obtained values are found not to correlate with depth, as the amphibolite facies pst varies between 21,88 and 139,12 MPa, and the eclogite facies pst between 35,51 and 146,6 MPa.
5. Both low and high average dynamic shear stresses are obtained for faults with small displacements, while a low average dynamic shear stress is obtained for the fault with the largest displacement.
6. Why rocks respond by brittle failure at great depths is still left as an open question.

Appendix

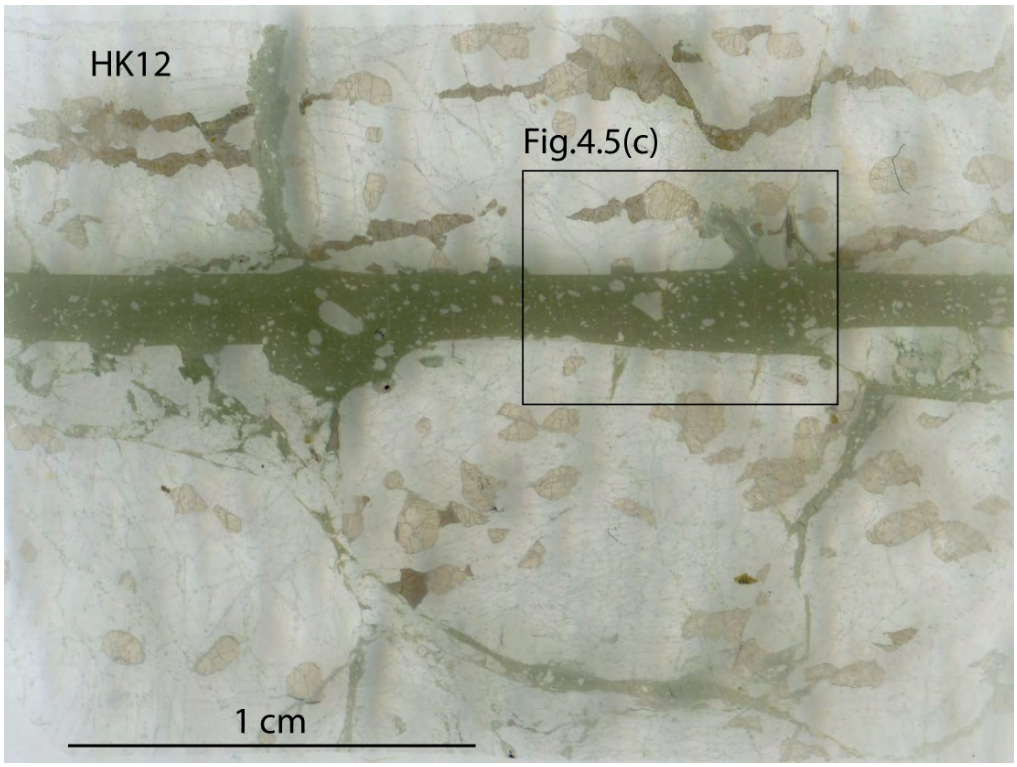

Figure 8.1: *Scan of thin section HK12 from fault HK.*

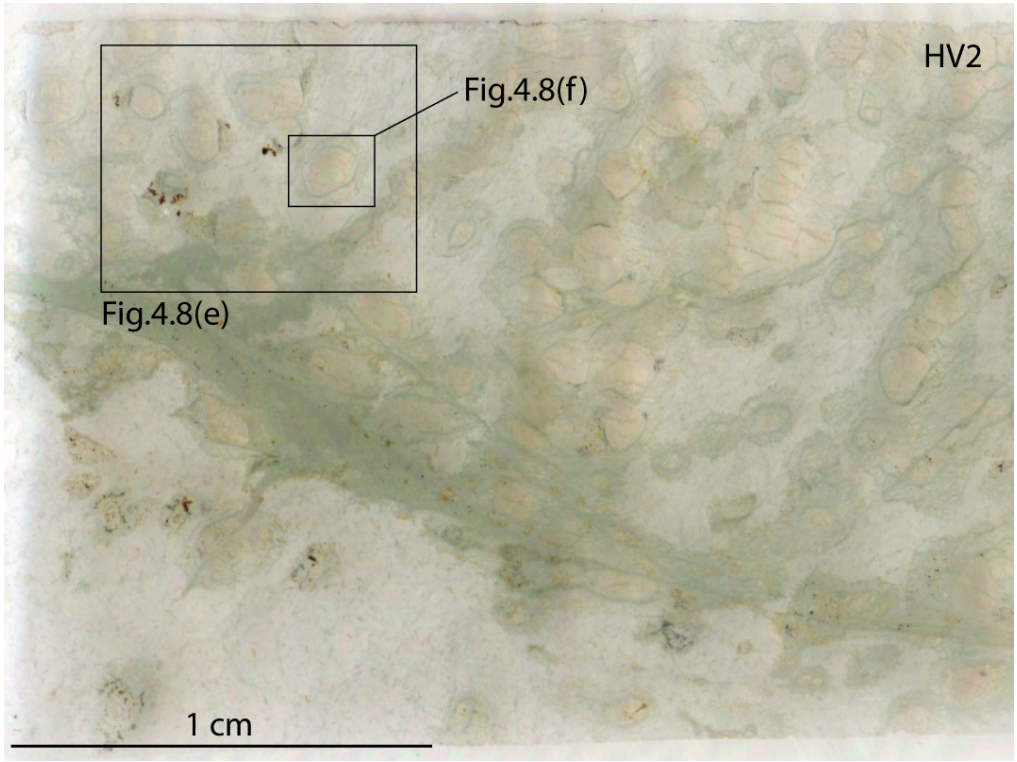

Figure 8.2: *Scan of thin section HV2 from fault HVa.*

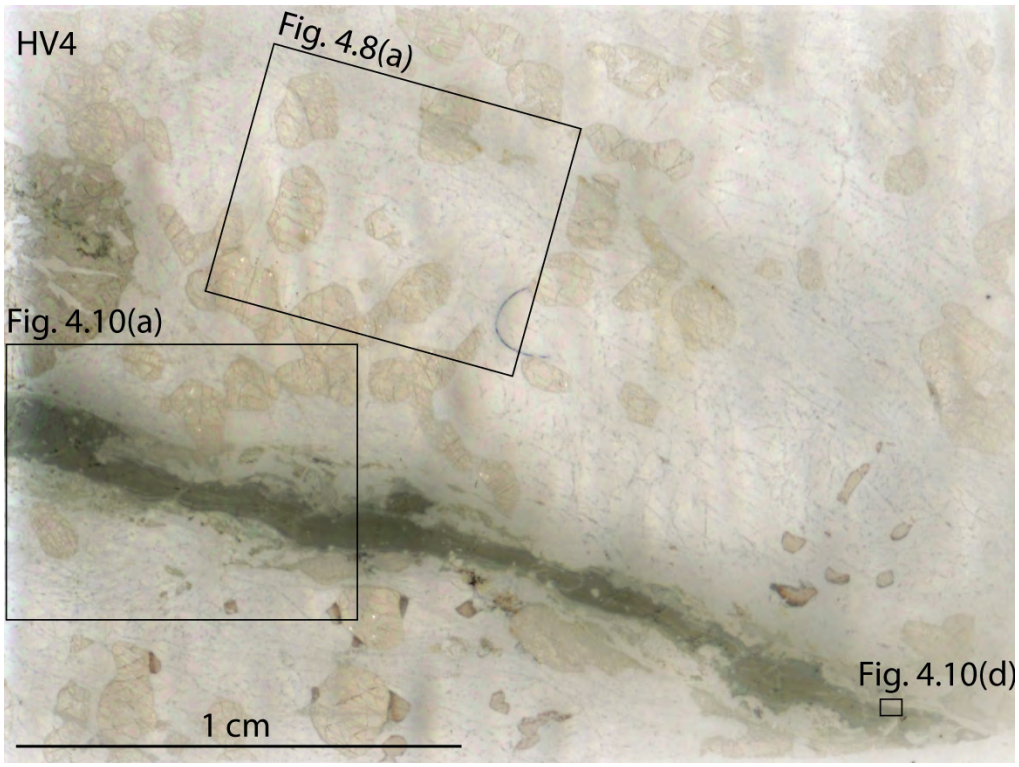

Figure 8.3: *Scan of thin section HV4 from fault HVa.*

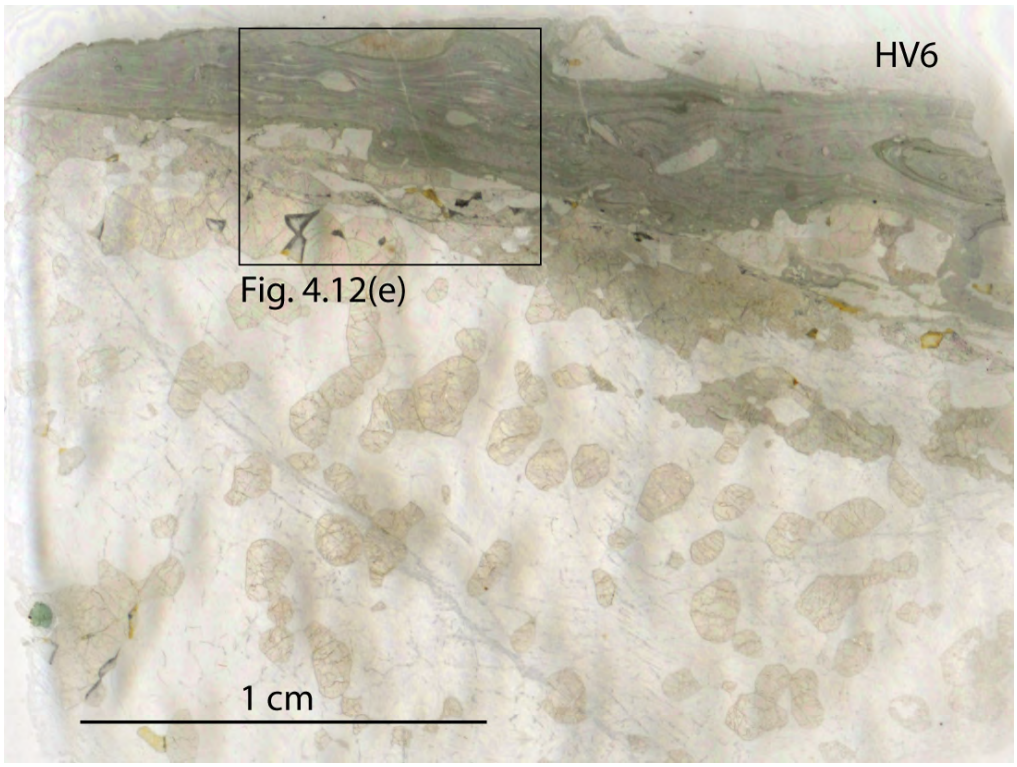

Figure 8.4: *Scan of thin section HV6 from fault HVb.*

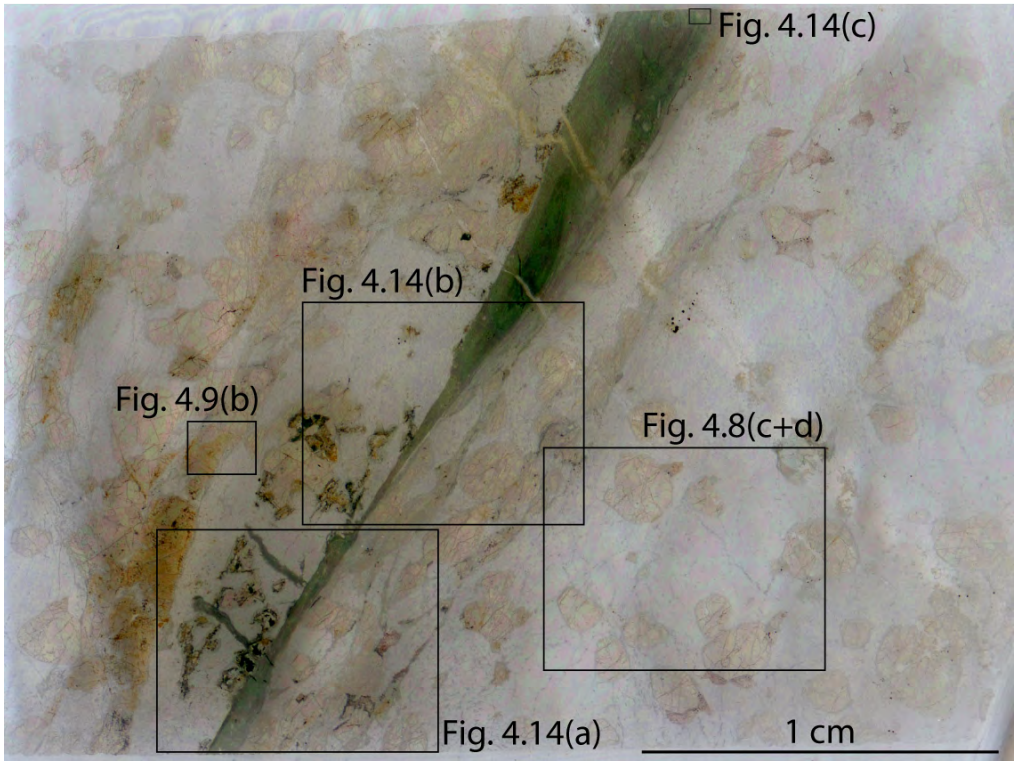

Figure 8.5: *Scan of thin section HV11 from fault HVc.*

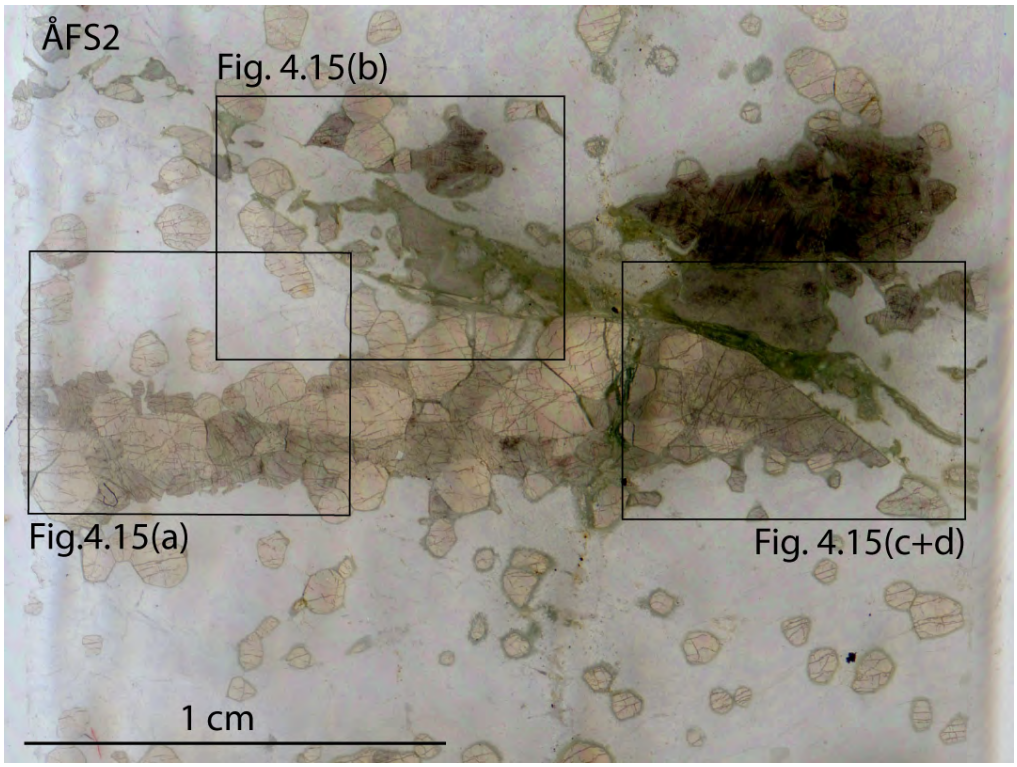

Figure 8.6: *Scan of thin section ÅFS2 from fault ÅFSa.*

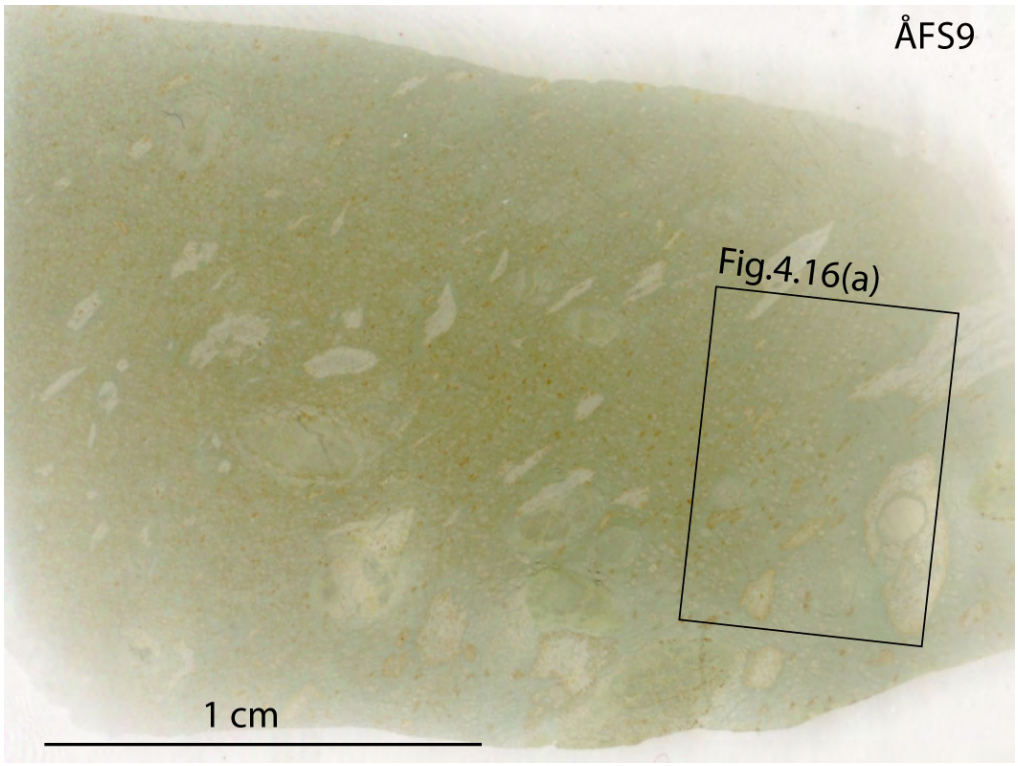

Figure 8.7: *Scan of thin section ÅFS9 from fault ÅFSc.*

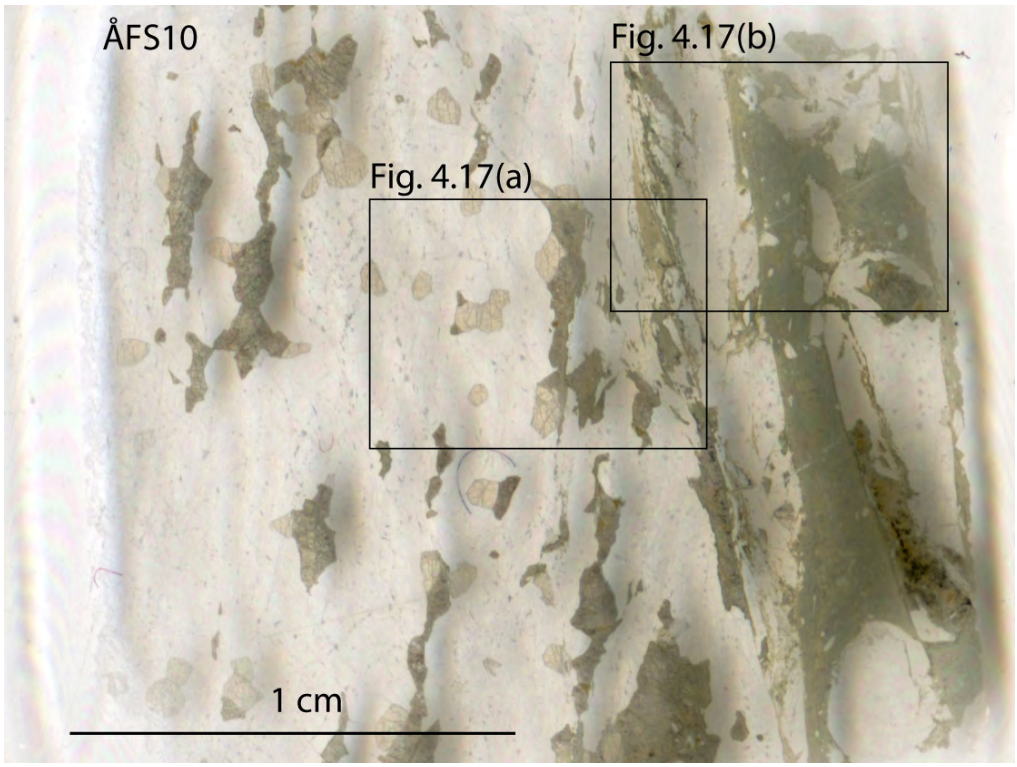

Figure 8.8: *Scan of thin section ÅFS10 from fault ÅFSd.*

Bibliography

T. B. Andersen and H. Austrheim. Fossil earthquakes recorded by pseudotachylytes in mantle peridotite from the alpine subduction complex of corsica. *Earth and Planetary Science Letters*, 242(1-2):58–72, 2006.

Torgeir B. Andersen, Fernando Corfu, Loic Labrousse, and Per-Terje Osmundsen. Evidence for hyperextension along the pre-caledonian margin of baltica. *Journal of the Geological Society*, 169 (5):601–612, 2012. doi: 10.1144/0016-76492012-011.

H. Austrheim and T. B. Andersen. Pseudotachylytes from corsica: Fossil earthquakes from a subduction complex. *Terra nova*, 16(4):193–197, 2004.

Håkon Austrheim. The granulite-eclogite facies transition: A comparison of experimental work and a narural occurrence in the bergen arcs, western norway. *Lithos*, 25:163–169, 1990.

Håkon Austrheim. Pers.comm., 2013.

Håkon Austrheim and Teresa M. Boundy. Pseudotachylytes generated during seismic faulting and eclogitization of the deep crust. *Science*, 265:82–83, 1994.

Håkon Austrheim and William L. Griffin. Shear deformation and eclogite formation within granulite-facies anorthosites of the bergen arcs, western norway. *Chemical Geology*, 50(1-3):267 – 281, 1985.

Håkon Austrheim and William L. Griffin. Eclogitization of lower crustal granulites by fluid migration through shear zones. *Earth and planetary Science Letters*, 81:221–232, 1987.

Håkon Austrheim, Muriel Erambert, and Theresa M. Boundy. Garnets recording deep crustal earthquakes. *Earth and Planetary Science Letters*, 139(1-2):223 – 238, 1996. ISSN 0012-821X. doi: 10.1016/0012-821X(95)00232-2.

Håkon Austrheim, Muriel Erambert, and Ane K. Engvik. Processing of crust in the root of the caledonian continental collision zone:the role of eclogitization. *Tecttonophysics*, 273:129–153, 1997.

Wolfgang Bach and Gretchen L. Früh-Green. Alteration of the oceanic lithosphere and implications for seafloor processes. *Elements*, 6(3):173–178, 2010.

Bernard Bingen, Håkon Austrheim, Martin J. Whitehouse, and William J. Davis. Trace element signature and u - pb geochronology of eclogite-facies zircon, bergen arcs, caledonides of w norway. *Contributions to Mineralogy and Petrology*, 147:671–683, 2004. ISSN 0010-7999. doi: 10.1007/s00410-004-0585-z.

Bernard Bingen, William J. Davis, and Håkon Austrheim. Zircon U-Pb geochronology in the Bergen arc eclogites and their Proterozoic protoliths, and implications for the pre-Scandian evolution of the Caledonides in western Norway. *Geological Society of America Bulletin*, 113(5):640–649, May, 2001. doi: 10.1130/0016-7606(2001)113⟨0640:ZUPGIT⟩2.0.CO;2.

M. Bjørnerud. Rethinking conditions necessary for pseudotachylyte formation: Observations from the otago schists, south island, new zealand. *Tectonophysics*, 490(1-2):69 – 80, 2010.

T.M. Boundy, K. Mezger, and E.J. Essene. Temporal and tectonic evolution of the granulite-eclogite association from the bergen arcs, western norway. *Lithos*, 39(3-4):159 – 178, 1997. ISSN 0024-4937. doi: 10.1016/S0024-4937(96)00026-6.

S. Braeck and Y. Y. Podladchikov. Spontaneous thermal runaway as an ultimate failure mechanism of materials. *Physical Review Letters*, 98(9):95504, 2007.

S. Braeck, Y. Y. Podladchikov, and S. Medvedev. Spontaneous dissipation of elastic energy by self-localizing thermal runaway. *Physical Review E*, 80(4), 2009.

I Bryhni and B.A. Strurt. Caledonides of southwestern norway. In D.G. Gee and B.A Sturt, editors, *The Caledonian Orogen–Scandinavian and Related Areas, Part 1*, A Wiley–Interscience Publication, pages 89–108. IGCP, John Wiley and Sons, 1985. A contribution to Project No. 27 The Caledonian Orogeny.

Wang-Ping Chen, Shu-Huei Hung, Tai-Lin Tseng, Michael Brudzinski, Zhaohui Yang, and Robert L. Nowack. Rheology of the continental lithosphere: Progress and new perspectives. *Gondwana Research*, 21(1):4 – 18, 2012. ISSN 1342-937X. doi: 10.1016/j.gr.2011.07.013. URL `http://www.sciencedirect.com/science/article/pii/S1342937X1100205X`. Tectonic evolution of Tibet and surrounding regions.

Giulio Di Toro, Giorgio Pennacchioni, and Giordano Teza. Can pseudotachylytes be used to infer earthquake source parameters? an example of limitations in the study of exhumed faults. *Tectonophysics*, 402(1-4):3–20, 2005. ISSN 0040-1951. doi: 10.1016/j.tecto.2004.10.014.

Robert S. Dietz. Vredefort ring structure; an astrobleme (meteorite impact structure). *Geological Society of America Bulletin*, 71(12):2093, 1960.

Yuri Fialko. Temperature fields generated by the elastodynamic propagation of shear cracks in the earth. *Journal of Geophysical Research: Solid Earth*, 109, 2004. doi: 10.1029/2003JB002497.

Johannes Glodny, Alexander Kuhn, and Håkon Austrheim. Geochronology of fluid-induced eclogite and amphibolite facies metamorphic reactions in a subduction - collision system, bergen arcs, norway. *Contributions to Mineralogy and Petrology*, 156:27–48, 2008. ISSN 0010-7999. doi: 10.1007/s00410-007-0272-y.

V.M. Goldschmidt. Om friksjonsglass (pseudo-tachyliytt) i fjellkjeden. *GFF*, 65, 1943.

Harry W. Green and Heidi Huston. The mechanics of deep earthquakes. *Annual reviews of earth and planetary science*, 23:160–213, 1995.

Harry W. Green, Thomas E Young, David Walker, and Christopher H. Scholz. Anticrack-associated faulting at very high pressure in natural olivine. *Nature*, 348, 1990.

Bradley R. Hacker, Simon M. Peacock, Geoffrey A Abers, and Stephen D. Holloway. Subduction factory 2. are intermediate–depth earthquakes in subducting slabs linked to metamorphic dehydration reactions? *Journal of Geophysical Research*, 108:2030–2045, 2003.

Bjørn Jamtveit, Kurt Bucher-Nurminen, and Håkon Austrheim. Fluid controlled eclogitization of granulites in deep crustal shear zones, bergen arcs, western norway. *Contributions to Mineralogy and Petrology*, 104:184–193, 1990. ISSN 0010-7999. doi: 10.1007/BF00306442.

Timm John and Volker Schenk. Interrelations between intermediate-depth earthquakes and fluid flow within subducting oceanic plates: Constraints from eclogite facies pseudotachylytes. *Geology*, 34(7):557–560, 2006. doi: 10.1130/G22411.1. URL `http://geology.gsapubs.org/content/34/7/557.abstract`.

Timm John, Sergei Medvedev, Lars H Rupke, Torgeir B. Andersen, Yuri Y. Podladchikov, and Håkon Austrheim. Generation of intermediate-depth earthquakes by self–localizing thermal runaway. *Nature Geoscience*, 2:137–140, 2009. doi: 10.1038/ngeo419. URL `http://geology.gsapubs.org/content/38/5/479.short`.

Laurent Jolivet, Hugues Raimbourg, Loic Labrousse, Dov Avigad, Yves Leroy, Håkon Austrheim, and Torgeir B. Andersen. Softening trigerred by eclogitization, the first step toward exhumation during continental subduction. *Earth and Planetary Science Letters*, 237(3 - 4):532 – 547, 2005. ISSN 0012-821X. doi: 10.1016/j.epsl.2005.06.047.

Haemyeong Jung, Harry W. Green, II, and Larissa F. Dobrzhinetskaya. Intermediate-depth earthquake faulting by dehydration embrittlement with negative volume change. *Nature*, 428(6982): 545–549, 2004.

Hiroo Kanamori. Earthquake physics and real-time seismology. *Nature*, 451(17):271–273, 2008.

Philip Kearey, Keith A. Klepies, and Frederick J. Vine. *Global Tectonics*. Wiley//Blackwell, third edition, 2009.

Peter B. Kelemen and Greg Hirth. A periodic shear heating mechanism for intermediate-depth earthquakes in the mantle. *Nature*, 446:787–790, 2007.

A.M. Killick. Pseudotachylyte generated as result of drilling burn-inn. *Tectonophysics*, 171(1-4): 221–227, 1990.

Stephen H. Kirby, William B. Durham, and Laura A. Stern. Mantle phase changes and deep-earthquake faulting in subducting lithosphere. *Science*, 252(5003):pp. 216–225, 1991. ISSN 00368075. URL `http://www.jstor.org/stable/2875676`.

CF Kolderup and NH Kolderup. Geology of the bergen arc system. *Bergens museums skrifter*, 20: 1–137, 1940.

Alexander Kuhn. *The influence of fluid on the granulite to eclogite and amphibolite facies transition: a study in the anorthositic rocks from the Lindås Nappe, Bergen Arcs, West Norway*. PhD thesis, University of Oslo, 2002.

Loic Labrousse, Gyorgy Hetenyi, Hugues Raimbourg, Laurent Jolivet, and Torgeir B. Andersen. Initiation of crustal-scale thrusts triggered by metamorphic reactions at depth: Insights from a comparison between the himalayas and scandinavian caledonides. *Tectonics*, 29(5), 2010. ISSN 1944-9194. doi: 10.1029/2009TC002602. URL `http://dx.doi.org/10.1029/2009TC002602`.

Aiming Lin. Injection veins of crushing-originated pseudotachylyte and fault gouge formed during seismic faulting. *Engineering Geology*, 43(2-3):213 – 224, 1996.

Aiming Lin and Toshihiko Shimamoto. Selective melting processes as inferred from experimentally generated pseudotachylytes. *Journal of Asian Earth Sciences*, 16(75 - 60):533 – 545, 1998.

M. G. Lund and H. Austrheim. Processes at the origin of deep crustal fault planes during fluid-induces eclogitization of dry granulites. *Unpublished*.

A.M. Lundmark and F. Corfu. Late-orogenic sveconorwegian massif anorthosite in the jotun nappe complex, sw norway, and causes of repeated amcg magmatism along the baltoscandian margin. *Contributions to Mineralogy and Petrology*, 155:147–163, 2008. ISSN 0010-7999. doi: 10.1007/s00410-007-0233-5.

A.M. Lundmark, F. Corfu, S. Spurgin, and R.S. Selbekk. Proterozoic evolution and provenance of the high-grade jotun nappe complex, {SW} norway: U-pb geochronology. *Precambrian Research*, 159(3-4):133 – 154, 2007.

R.H. Maddock. Frictional melting in landslide-generated frictionites (hyalomylonites) and fault-generated pseudotachylytes-discussion. *Tectonophysics*, 128(1 - 2):151 – 153, 1986. ISSN 0040-1951.

Jerry F. Magloughlin and John G. Spray. Frictional melting processes and products in geological materials: introduction and discussion. *Tectonophysics*, 204(3 - 4):197 – 204, 1992. ISSN 0040-1951.

L. Masch, H.R. Wenk, and E. Preuss. Electron microscopy study of hyalomylonite as evidence for frictional melting in landslides. *Tectonophysics*, 11(1 - 2):131 – 160, 1985.

C.W. Passchier. Pseudotachylyte and the developement of ultramylonite bands in the saint-bartelemy massif, french pyrenees. *Journal of Structureal Geology*, (1), 1982.

C.W. Passchier and R.A.J. Trouw. *Microtectonics*. Springer, 2.nd edition, 2005.

A. R. Philpotts. Origin of pseudotachylites. *American Journal of Science*, 262(8):1008–1035, 1964.

James R. Rice. Heating and weakening of faults during earthquake slip. *Journal of Geophysical Research: Solid Earth*, 2006.

D. Roberts and D.G. Gee. An introduction to the structure of the scandinavian caledonides. In D.G. Gee and B.A Sturt, editors, *The Caledonian Orogen–Scandinavian and Related Areas, Part 1*, A Wiley–Interscience Publication, pages 55–68. IGCP, John Wiley and Sons, 1985. A contribution to Project No. 27 The Caledonian Orogeny.

D. Roberts and B. A. Sturt. Caledonian deformation in norway. *Journal of the Geological Society*, 137(3):241–250, 1980.

David Roberts. The scandinavian caledonides: event chronology, palaeogeographic settings and likely modern analogues. *Tectonophysics*, 365(1 - 4):283 – 299, 2003. ISSN 0040-1951. doi: 10.1016/S0040-1951(03)00026-X. Collisional Orogenesis in the Geological Record and Modern Analogues.

C. Roffeis, F. Corfu, and H. Austrheim. Evidence for a caledonian amphibolite to eclogite facies pressure gradient in the middle allochthon lindås nappe, sw-norway. *Contributions to Mineralogy and Petrology*, 164:81–99, 2012. ISSN 0010-7999. doi: 10.1007/s00410-012-0727-7.

Christopher H. Scholz. *The mechanics of earthquakes and faulting*. Cambridge University Press, Cambridge, first edition, 1990.

S. James Shand. The pseudotachylyte of parijs (orange free state), and its relation to trap - shotten gneiss and flinty crush - rocks. *Quarterly Journal of the Geological Society*, 72(1-4):198–220, NP–NP, 221, 1916. doi: 10.1144/GSL.JGS.1916.072.01-04.12.

Richard H. Sibson. Generation of pseudotachylyte by ancient seismic faulting. *Geophysical Journal International*, 43(3):775–794, 1975.

Richard H. Sibson and Virginia G. Toy. The habitat of fault-generated pseudotachylyte: Presence vs. absence of friction-melt. In R Abercrombie, A McGarr, G DiToro, and H Kanamori, editors, *Earthquakes: Radiated Energy and the Physics of Faulting*, volume 170 of *Geophysical Monograph Series*, pages 153–166. ECNP, American Geophysical Union, 2006. Conference on Radiated Energy and the Physics of Earthquake Faulting, Portland, ME, jun, 2005.

Jaakko Siivola and Rolf Schmid. List of mineral abbreviations, 2007. Recommendations by the IUGS Subcommission on the Systematics of Metamorphic Rocks: Web version 01.02.07.

Kurt Stuwe. Energetics: Heat and temperature. In *Geodynamics of the Lithosphere*, pages 51–137. Springer Berlin Heidelberg, 2007.

Mark T. Swanson. Fault structure, wear mechanisms and rupture processes in pseudotachylyte generation. *Tectonophysics*, 204(3 - 4):223 – 242, 1992. ISSN 0040-1951. doi: 10.1016/0040-1951(92)90309-T.

Tracy N Tingle, Harry W II Green, Christopher H Scholz, and T.A Koczynski. The rheology of faults triggered by the olivine-spinel transformation in mg2geo4 and its implications for the mechanism of deep-focus earthquakes. *Journal of Structural Geology*, 15(9 - 10):1249 – 1256, 1993.

Robert J. Twiss and Eldridge M. Moores. *Structural Geology*. W. H. Freeman and Company, New York, second edition, 2007.

A. Vigano, S. Tumiati, S. Recchia, S. Martin, M. Marelli, and R. Rigon. Carbonate pseudotachylytes: evidence for seismic faulting along carbonate faults. *Terra Nova*, 23:187–194, 2011.

Paul H. Warren. Anorthosite assimilation and the origi of the mg/fe-related bimodality of pristine moon rocks: Support for the magmasphere hypothesis. *Journal of geophysical research*, 91(B4): 331–343, 1986.

L.E. Weiss and H.R. Wenk. Experimentally produced pseudotachylite-like veins in gabbro. *Tectonophysics*, 96(3-4):299 – 310, 1983.

O. P. Wennberg, A. G. Milnes, and I Winsvold. The northern bergen arc shear zone - an oblique-lateral ramp in the devonian extensional detachment system of western norway. *Norsk Geologisk Tidsskrift*, 78(3):169–184, 1998.

Joseph Clancy White. Paradoxical pseudotachylyte - fault melt outside the seismogenic zone. *Journal of Structural Geology*, 38(0):11 – 20, 2012. ISSN 0191-8141. doi: 10.1016/j.jsg.2011.11.016. Physico-Chemical Processes in Seismic Faults.